

Air Force Institute of Technology

**AFIT Scholar**

---

Theses and Dissertations

Student Graduate Works

---

3-2000

## An Experimental Investigation on Periodic Forced Vibrations of a Bladed Disk

Colin J. Duffield

Follow this and additional works at: <https://scholar.afit.edu/etd>



Part of the [Aerospace Engineering Commons](#)

---

### Recommended Citation

Duffield, Colin J., "An Experimental Investigation on Periodic Forced Vibrations of a Bladed Disk" (2000). *Theses and Dissertations*. 4776.  
<https://scholar.afit.edu/etd/4776>

This Thesis is brought to you for free and open access by the Student Graduate Works at AFIT Scholar. It has been accepted for inclusion in Theses and Dissertations by an authorized administrator of AFIT Scholar. For more information, please contact [AFIT.ENWL.Repository@us.af.mil](mailto:AFIT.ENWL.Repository@us.af.mil).



**AN EXPERIMENTAL INVESTIGATION ON PERIODIC  
FORCED VIBRATIONS OF A BLADED DISK**

THESIS

Colin J. Duffield, Captain, USAF

AFIT/GAE/ENY/00M-05

**DEPARTMENT OF THE AIR FORCE  
AIR UNIVERSITY**

**AIR FORCE INSTITUTE OF TECHNOLOGY**

---

Wright-Patterson Air Force Base, Ohio

APPROVED FOR PUBLIC RELEASE; DISTRIBUTION UNLIMITED

**DTIC QUALITY INSPECTED 4**

**20000803 107**

The views expressed in this thesis are those of the author and do not reflect the official policy or position of the Department of Defense or the United States Government.

AFIT/GAE/ENY/00M-05

AN EXPERIMENTAL INVESTIGATION ON PERIODIC  
FORCED VIBRATIONS OF A BLADED DISK

THESIS

Presented to the Faculty of the School of Engineering and Management  
of the Air Force Institute of Technology

Air University

In Partial Fulfillment of the  
Requirements for the Degree of  
Master of Science

Colin J. Duffield, B.S.

Captain, USAF

March, 2000


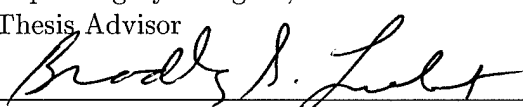
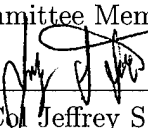
Approved for public release; distribution unlimited

AFIT/GAE/ENY/00M-05

AN EXPERIMENTAL INVESTIGATION ON PERIODIC  
FORCED VIBRATIONS OF A BLADED DISK

Colin J. Duffield, B.S.  
Captain, USAF

Approved:

 _____ Capt Gregory S. Agnes, Ph.D. Thesis Advisor	<u>9 Mar 00</u> _____ Date
 _____ Dr. Bradley S. Liebst Committee Member	<u>9 Mar 00</u> _____ Date
 _____ Lt Col Jeffrey S. Turcotte, Ph.D. Committee Member	<u>9 Mar 00</u> _____ Date

## *Acknowledgements*

The process of completing this thesis was one of extreme personal growth. The opportunity to be immersed in a challenging research topic, become acutely informed and to advance the forefront understanding of a formidable engineering problem is something to which I may never have exposure again. Likewise, the persistent stress and emotional management towards seemingly overwhelming obstacles has only advanced my overall abilities and capacities.

To these ends, thank you God for the blessings and grace to finish this journey. My faith and belief in Jesus Christ has been a bedrock of hope and peace throughout all the struggles. To these gifts which I can never repay, I am eternally grateful.

I would like to thank my advisor Captain Agnes for offering me this unique research idea. The guidance and insightful recommendations you gave helped push me through many barriers. Good luck with all your future plans for this experimental platform. There are numerous other individuals sprinkled throughout AFIT and AFRL who were also invaluable. Lt Col. Turcotte and Dr. Liebst, thank you for your expertise and availability to answer research questions. Your assistance tremendously helped me comprehend the immense amounts of theory I needed to grasp. Dr. Joseph Holkamp and Robert Gordon, sharing your experiences with this research topic certainly provided me much needed direction and motivation in my early stages of learning. Your thoughts and suggestions then and through some arduous test phases undoubtedly eased the progression of this work. Jay Anderson and Bob Bacon, where else would I have gone with my instant 'fix-it' needs for laboratory equipment and supplies? Your services and readily available answers relieved me of much unwanted stress, thank you.

I would also like to thank some of my classmates with helping me prepare my writing and research approach. Those nagging LATEX sticking points: Julian 'Juj' Jarosh, Pete Cseke and Joe Fulton, thanks for the tips and tricks to make it through all that programming. Providing the basic foundation to begin this research, thank you Amy Cox for your

previous thesis work, computer programs and paving the way around all the dead-ends I never had to experience.

Finally, I would like to thank Jeannine, my fiancée for the love, generous support and sacrifice. Your selflessness and sympathy with all the difficulties we endured together and just for the person you've always been to me, I love you.

Colin J. Duffield

# *Table of Contents*

	Page
Acknowledgements . . . . .	iii
List of Figures . . . . .	viii
List of Tables . . . . .	xiii
List of Abbreviations . . . . .	xv
Abstract . . . . .	xvi
 I. Introduction and Overview . . . . .	 1-1
1.1 Background . . . . .	1-1
1.1.1 High Cycle Fatigue of Turbine Engine Blades . . . . .	1-1
1.1.2 The Behavior of Bladed Disk Assemblies . . . . .	1-2
1.2 Experimental Analysis of Blisk Forced Response . . . . .	1-5
1.3 Periodic Forcing Function . . . . .	1-6
1.4 Response Measurement with Norm Scales . . . . .	1-6
1.5 Thesis Overview . . . . .	1-8
 II. Forced Response Numerical Demonstration . . . . .	 2-1
2.1 Eight Mass RPS Model . . . . .	2-1
2.1.1 Equations of Motion . . . . .	2-1
2.1.2 Free Response of Eight Mass RPS . . . . .	2-6
2.1.3 Forced Response of Eight Mass RPS . . . . .	2-14
2.2 Summary . . . . .	2-20

	Page
III. Experimental Methodology and Equipment . . . . .	3-1
3.1 Experimental Test Methods . . . . .	3-1
3.1.1 Free Response Method . . . . .	3-1
3.1.2 Forced Response Method . . . . .	3-2
3.2 Experimental Equipment . . . . .	3-2
3.2.1 Test Article Description . . . . .	3-2
3.2.2 Excitation System Descriptions . . . . .	3-5
3.2.3 Data Acquisition System . . . . .	3-9
3.2.4 Sensor Descriptions . . . . .	3-12
3.3 Summary . . . . .	3-14
IV. Experimental Procedure . . . . .	4-1
4.1 Overview . . . . .	4-1
4.2 Accelerometer Calibration . . . . .	4-2
4.3 Input Force Characterization . . . . .	4-3
4.3.1 Pulse Phasing and Blade Order . . . . .	4-9
4.4 Blade Characterization . . . . .	4-10
4.4.1 Dimensions and Mass . . . . .	4-11
4.4.2 Blade Natural Frequencies and Mode Shapes . . . . .	4-12
4.4.3 Blades' Natural Frequencies and Damping - Two Cases . . . . .	4-19
4.5 Modal Testing of the Bladed Disk . . . . .	4-23
4.6 Forced Response Experimentation . . . . .	4-30
4.7 Summary . . . . .	4-33
V. Results and Discussion . . . . .	5-1
5.1 Forced Response Data Arrangement . . . . .	5-1
5.2 Presentation of Results . . . . .	5-2
5.2.1 General Observations . . . . .	5-4

	Page
5.2.2 Effects of Mistuning Strength . . . . .	5-10
5.2.3 Variance of Engine Order . . . . .	5-14
5.2.4 Comparison Between Modes . . . . .	5-15
5.3 Summary . . . . .	5-17
VI. Conclusions and Recommendations . . . . .	6-1
6.1 Conclusions . . . . .	6-1
6.2 Recommendations . . . . .	6-2
6.2.1 Experimental Improvements . . . . .	6-2
6.2.2 Future Research . . . . .	6-3
6.3 Summary . . . . .	6-5
Appendix A. Supplemental Graphs - Periodic Forcing Function Figures . .	A-1
Appendix B. Supplemental Graphs - Forced Response Figures . . . . .	B-1
Bibliography . . . . .	BIB-1
Vita . . . . .	VITA-1

## *List of Figures*

Figure		Page
1.1.	Example RPS Model . . . . .	1-2
2.1.	Eight Mass RPS Model . . . . .	2-2
2.2.	Vector Diagram for Equations of Motion . . . . .	2-3
2.3.	Natural Frequencies and Mode Shapes of Tuned Eight Mass RPS .	2-6
2.4.	Modal Characterization of Mistuned Eight Mass RPS - Case I . . .	2-10
2.5.	Modal Characterization of Mistuned Eight Mass RPS - Case II . . .	2-11
2.6.	Modal Characterization of Mistuned Eight Mass RPS - Case III . .	2-11
2.7.	Modal Characterization of Mistuned Eight Mass RPS - Case IV . .	2-12
2.8.	Modal Characterization of Mistuned Eight Mass RPS - Case V . . .	2-12
2.9.	Modal Characterization of Mistuned Eight Mass RPS - Case VI . .	2-13
2.10.	Maximum Blade Amplitude of Mistuned Eight Mass RPS - Case I .	2-17
2.11.	Four/Two and Infinity/Two Norm Scales of Mistuned Eight Mass RPS - Case I . . . . .	2-19
3.1.	Modal Testing Experiment Setup Block Diagram . . . . .	3-1
3.2.	Forced Response Experiment Setup Block Diagram . . . . .	3-3
3.3.	Bladed Disk Test Article . . . . .	3-4
3.4.	Sample Blade Root of Ill-Constructed Test Article . . . . .	3-5
3.5.	Excitation System Flywheel . . . . .	3-6
3.6.	Flywheel as Input Force to Blisk . . . . .	3-7
3.7.	QP10Ni Strain Actuator Drawing (2) . . . . .	3-8
3.8.	Blade Test Configuration . . . . .	3-9
3.9.	BNC Supply Board . . . . .	3-10
3.10.	Data Acquisition Up Block Diagram (8) . . . . .	3-11

Figure		Page
3.11.	Ometron VH300 Laser Vibrometer . . . . .	3-13
4.1.	Calibration Equipment Setup (8) . . . . .	4-3
4.2.	Time Response of E.O. 12 with 0.2 in Spacing . . . . .	4-5
4.3.	PSD of E.O. 12 with 0.2 in Spacing . . . . .	4-6
4.4.	Time Response of Various Engine Orders, 300 Hz, 0.4 in Spacing . . . . .	4-8
4.5.	Pulse Phasing for Engine Order 4 and 12 . . . . .	4-9
4.6.	Pulse Phasing for Engine Order 6 . . . . .	4-10
4.7.	Pulse Phasing for Engine Order 3 . . . . .	4-10
4.8.	Pulse Phasing for Engine Order 2 . . . . .	4-10
4.9.	Mode Shape Construction Experimental Setup . . . . .	4-13
4.10.	Blade Three Mode Shape Measurement Points . . . . .	4-14
4.11.	Hub Frequency Response Function - Point 17 . . . . .	4-17
4.12.	Blade Three Mode Shape - 1 <sup>st</sup> Bending Mode (210.7 Hz) . . . . .	4-18
4.13.	Blade Three Mode Shape - 1 <sup>st</sup> Torsion Mode (553.4 Hz) . . . . .	4-18
4.14.	Blade Three Mode Shape - 2 <sup>nd</sup> Bending Mode (1297.6 Hz) . . . . .	4-19
4.15.	Time Response of Blade 5 during Blade 2 Excitation - 1 <sup>st</sup> Bending, Case II . . . . .	4-25
4.16.	Normalized Mode Shapes - Case I, 1 <sup>st</sup> Bending Mode . . . . .	4-27
4.17.	Normalized Mode Shapes - Case II, 1 <sup>st</sup> Bending Mode . . . . .	4-27
4.18.	Normalized Mode Shapes - Case I, 1 <sup>st</sup> Torsion Mode . . . . .	4-28
4.19.	Normalized Mode Shapes - Case II, 1 <sup>st</sup> Torsion Mode . . . . .	4-28
4.20.	Forced Response Testing with RPM Timing Gun . . . . .	4-32
5.1.	Individual Blade Responses - Case I, E.O. 3, 1 <sup>st</sup> Bending Mode . . . . .	5-2
5.2.	Blade Responses - Case I, E.O. 3, 1 <sup>st</sup> Bending Mode . . . . .	5-3
5.3.	Four/Two and Infinity/Two Norm Plot - Case I, E.O. 3, 1 <sup>st</sup> Bending Mode . . . . .	5-3
5.4.	Experimental Blisk Campbell Diagram . . . . .	5-5

Figure		Page
5.5.	Magnified Bladed Disk 1 <sup>st</sup> Bending Mode and E.O. 3 Intersection .	5-5
5.6.	Subharmonics of E.O. 12 . . . . .	5-6
5.7.	Infinity/Two Norm Scale of E.O. 12, Case I. 1 <sup>st</sup> Torsion . . . . .	5-11
5.8.	Maximum Blade Amplitude - E.O. 3, 1 <sup>st</sup> Bending Mode . . . . .	5-12
5.9.	Global Maximum and Minimum Four/Two Norm Values - 1 <sup>st</sup> Bending Mode . . . . .	5-16
5.10.	Global Maximum and Minimum Four/Two Norm Values . . . . .	5-17
A.1.	Time Response of E.O. 12 with 0.4 in Spacing . . . . .	A-2
A.2.	PSD of E.O. 12 with 0.4 in Spacing . . . . .	A-2
A.3.	Time Response of E.O. 12 with 0.6 in Spacing . . . . .	A-3
A.4.	PSD of E.O. 12 with 0.6 in Spacing . . . . .	A-3
A.5.	Time Response of E.O. 6 with 0.4 in Spacing . . . . .	A-4
A.6.	PSD of E.O. 6 with 0.4 in Spacing . . . . .	A-4
A.7.	Time Response of E.O. 4 with 0.4 in Spacing . . . . .	A-5
A.8.	PSD of E.O. 4 with 0.4 in Spacing . . . . .	A-5
A.9.	Time Response of E.O. 3 with 0.4 in Spacing . . . . .	A-6
A.10.	PSD of E.O. 3 with 0.4 in Spacing . . . . .	A-6
B.1.	Individual Blade Responses - Case I, E.O. 4, 1 <sup>st</sup> Bending Mode . .	B-2
B.2.	Blade Responses - Case I, E.O. 4, 1 <sup>st</sup> Bending Mode . . . . .	B-3
B.3.	Four/Two and Infinity/Two Norm Plot - Case I, E.O. 4, 1 <sup>st</sup> Bending Mode . . . . .	B-3
B.4.	Individual Blade Responses - Case I, E.O. 6, 1 <sup>st</sup> Bending Mode . .	B-4
B.5.	Blade Responses - Case I, E.O. 6, 1 <sup>st</sup> Bending Mode . . . . .	B-5
B.6.	Four/Two and Infinity/Two Norm Plot - Case I, E.O. 6, 1 <sup>st</sup> Bending Mode . . . . .	B-5
B.7.	Individual Blade Responses - Case I, E.O. 12, 1 <sup>st</sup> Bending Mode . .	B-6
B.8.	Blade Responses - Case I, E.O. 12, 1 <sup>st</sup> Bending Mode . . . . .	B-7

Figure		Page
B.9.	Four/Two and Infinity/Two Norm Plot - Case I, E.O. 12, 1 <sup>st</sup> Bending Mode . . . . .	B-7
B.10.	Individual Blade Responses - Case I, E.O. 6, 1 <sup>st</sup> Torsion Mode . . .	B-8
B.11.	Blade Responses - Case I, E.O. 6, 1 <sup>st</sup> Torsion Mode . . . . .	B-9
B.12.	Four/Two and Infinity/Two Norm Plot - Case I, E.O. 6, 1 <sup>st</sup> Torsion Mode . . . . .	B-9
B.13.	Individual Blade Responses - Case I, E.O. 12, 1 <sup>st</sup> Torsion Mode . .	B-10
B.14.	Blade Responses - Case I, E.O. 12, 1 <sup>st</sup> Torsion Mode . . . . .	B-11
B.15.	Four/Two and Infinity/Two Norm Plot - Case I, E.O. 12, 1 <sup>st</sup> Torsion Mode . . . . .	B-11
B.16.	Individual Blade Responses - Case II, E.O. 3, 1 <sup>st</sup> Bending Mode . .	B-12
B.17.	Blade Responses - Case II, E.O. 3, 1 <sup>st</sup> Bending Mode . . . . .	B-13
B.18.	Four/Two and Infinity/Two Norm Plot - Case II, E.O. 3, 1 <sup>st</sup> Bending Mode . . . . .	B-13
B.19.	Individual Blade Responses - Case II, E.O. 4, 1 <sup>st</sup> Bending Mode . .	B-14
B.20.	Blade Responses - Case II, E.O. 4, 1 <sup>st</sup> Bending Mode . . . . .	B-15
B.21.	Four/Two and Infinity/Two Norm Plot - Case II, E.O. 4, 1 <sup>st</sup> Bending Mode . . . . .	B-15
B.22.	Individual Blade Responses - Case II, E.O. 6, 1 <sup>st</sup> Bending Mode . .	B-16
B.23.	Blade Responses - Case II, E.O. 6, 1 <sup>st</sup> Bending Mode . . . . .	B-17
B.24.	Four/Two and Infinity/Two Norm Plot - Case II, E.O. 6, 1 <sup>st</sup> Bending Mode . . . . .	B-17
B.25.	Individual Blade Responses - Case II, E.O. 12, 1 <sup>st</sup> Bending Mode .	B-18
B.26.	Blade Responses - Case II, E.O. 12, 1 <sup>st</sup> Bending Mode . . . . .	B-19
B.27.	Four/Two and Infinity/Two Norm Plot - Case II, E.O. 12, 1 <sup>st</sup> Bending Mode . . . . .	B-19
B.28.	Individual Blade Responses - Case II, E.O. 6, 1 <sup>st</sup> Torsion Mode . .	B-20
B.29.	Blade Responses - Case II, E.O. 6, 1 <sup>st</sup> Torsion Mode . . . . .	B-21

Figure		Page
B.30.	Four/Two and Infinity/Two Norm Plot - Case II, E.O. 6, 1 <sup>st</sup> Torsion Mode . . . . .	B-21
B.31.	Individual Blade Responses - Case II, E.O. 12, 1 <sup>st</sup> Torsion Mode . .	B-22
B.32.	Blade Responses - Case II, E.O. 12, 1 <sup>st</sup> Torsion Mode . . . . .	B-23
B.33.	Four/Two and Infinity/Two Norm Plot - Case II, E.O. 12, 1 <sup>st</sup> Torsion Mode . . . . .	B-23

# *List of Tables*

Table		Page
2.1.	Blade Stiffness Mistuning Distributions for Eight Mass RPS . . . . .	2-9
2.2.	RPS Mistuning and Inter-Blade Coupling Cases . . . . .	2-9
2.3.	Four/Two and Infinity/Two Norm Scale Values of RPS Mistuning Cases . . . . .	2-14
4.1.	Accelerometer Calibration Equipment Settings . . . . .	4-3
4.2.	ENDEVCO® Accelerometer Sensitivities . . . . .	4-3
4.3.	Force Input Characterization Equipment Settings . . . . .	4-4
4.4.	Input Force Phasing at Various Magnet Configurations . . . . .	4-9
4.5.	Individual Blade Physical Properties . . . . .	4-11
4.6.	Blade Modal Characterization Equipment Settings . . . . .	4-13
4.7.	Blade Three Measurement Point Locations . . . . .	4-14
4.8.	Blade Three Natural Frequencies and Damping Ratios . . . . .	4-16
4.9.	Blade Three Mode Shapes . . . . .	4-16
4.10.	Individual Blade Modal Properties Equipment Settings . . . . .	4-20
4.11.	Hankel Matrix Dimensions & Singular Values for Blade Modal Analysis	4-21
4.12.	Blade Natural Frequencies and Damping Ratios - 1 <sup>st</sup> Bending Mode	4-21
4.13.	Blade Natural Frequencies and Damping Ratios - 1 <sup>st</sup> Torsion Mode	4-22
4.14.	Blade Natural Frequencies and Damping Ratios - 2 <sup>st</sup> Bending Mode	4-22
4.15.	Chirp Signal Sweeps for Bladed Disk Modal Tests . . . . .	4-23
4.16.	Bladed Disk Modal Test Equipment Settings . . . . .	4-24
4.17.	Amplifier-Blade Assignments for Blisk Modal Tests . . . . .	4-24
4.18.	Hankel Matrix Dimensions & Singular Values for Bladed Disk Modal Tests . . . . .	4-26
4.19.	Blisk Natural Frequencies and Damping Ratios - 1 <sup>st</sup> Bending Mode	4-26

Table		Page
4.20.	Blisk Natural Frequencies and Damping Ratios - 1 <sup>st</sup> Torsion Mode .	4-26
4.21.	Free Response Norm Scales of Bladed Disk - 1 <sup>st</sup> Bending Mode . .	4-29
4.22.	Free Response Norm Scales of Bladed Disk - 1 <sup>st</sup> Torsion Mode . . .	4-29
4.23.	Modal Frequencies to Flywheel RPM Conversions - 1 <sup>st</sup> Bending . .	4-30
4.24.	Modal Frequencies to Flywheel RPM Conversions - 1 <sup>st</sup> Torsion . . .	4-31
4.25.	Frequency Steps Between Forced Response Data Points . . . . .	4-32
4.26.	Bladed Disk Forced Response Test Equipment Settings . . . . .	4-33
5.1.	Maximum Blade Responses - Case I, 1 <sup>st</sup> Bending Mode . . . . .	5-7
5.2.	Maximum Blade Responses - Case I, 1 <sup>st</sup> Torsion Mode . . . . .	5-8
5.3.	Maximum Blade Responses - Case II, 1 <sup>st</sup> Bending Mode . . . . .	5-8
5.4.	Maximum Blade Responses - Case II, 1 <sup>st</sup> Torsion Mode . . . . .	5-9
5.5.	Global Norm Scale Extremas - E.O. 3, 1 <sup>st</sup> Bending Mode . . . . .	5-13
5.6.	Number of Local Four/Two Norm Scale Extremas - 1 <sup>st</sup> Bending Mode	5-13
5.7.	Number of Local Four/Two Norm Scale Extremas - 1 <sup>st</sup> Torsion Mode	5-13
5.8.	Frequency Distribution of Localization - 1 <sup>st</sup> Bending Mode . . . . .	5-13

## *List of Abbreviations*

Abbreviation	Page
HCF High Cycle Fatigue . . . . .	1-1
RPS Rotationally Periodic Structure . . . . .	1-2
FEM Finite Element Model . . . . .	1-4
ROM Reduced Order Model . . . . .	1-4
STD Standard Deviation . . . . .	2-8
RMS Root Mean Square . . . . .	2-17
PC Personal Computer . . . . .	3-2
HP Hewlett Packard . . . . .	3-2
RPM Revolutions Per Minute . . . . .	3-6
GUI Graphical User Interface . . . . .	3-9
FRF Frequency Response Functions . . . . .	3-10
DLL Dynamic Linked Library . . . . .	3-10
PSD Power Spectral Densities . . . . .	4-4
ERA Eigensystem Realization Algorithm . . . . .	4-13
AFRL Air Force Research Laboratory . . . . .	4-13
EMAC Eigensystem Modal Assurance Criterion . . . . .	4-15
SIMO Single Input Multiple Output . . . . .	4-15
MIMO Multiple Input Multiple Output . . . . .	4-25

## *Abstract*

Turbine engine blades are subject to extreme dynamic vibrational loads during normal operations. Harmonic forcing produced from periodic wakes created by fixed stators can excite blade resonant frequencies. Prolonged or repeated exposure to these forces can cause vibration-induced fatigue, otherwise known as High Cycle Fatigue (HCF). HCF effects are magnified by small material, manufacturing and geometrical irregularities among the blades, called mistuning. Structural mistuning can result in some blades experiencing stresses much higher than would be encountered in a perfect structure. Blade amplitude increases of over 100% have been observed in blades with natural frequencies less than 2% off their nominal value. Premature blade failures, operational costs and engine servicing all increase due to the HCF problem.

This study offered a novel approach to characterize mistuning effects on forced vibration behavior of bladed disks. A model fan reduced in dynamic scale from an operational jet engine fan and with weak inter-blade coupling was fabricated. Aerodynamic disturbances produced by the stators were replicated by magnets attached to a rotating flywheel interacting with similar magnets epoxied to the model fan blades. Flywheel magnets were spatially placed to represent various multiples of flywheel rotational frequency, or engine orders. Forced vibratory responses were measured by accelerometer transducers glued to the blade tips. Transducer response signals were analyzed by an appropriately configured data acquisition system.

The first bending and first torsion blade modes were selected for analysis. Additionally, two distinct mistuning cases were chosen. The first case was of the original, untouched model fan while the second represented a closely tuned first bending mode among all blades. Four flywheel engine orders of three, four, six and twelve were used as the periodic forcing function. A total of twelve test runs were conducted amongst all the configurations.

The flywheel excitation system performed very well in its ability to impart periodic forcing onto the bladed disk. The periodic forcing input, varying in magnitude and frequency distribution with engine order, produced an assortment of forced vibration results.

Several mechanisms, including changing mistuning levels, engine order and stimulated modal group substantially altered the system response. Areas influenced include localization levels, response profiles of individual blades, number of maximum blade amplitude peaks and the localization frequency range.

Norm scales featured in previous cyclic structure free response studies were utilized as localization indicators for this research. Unfortunately, the four/two and infinity/two norm scales used were inadequate to correlate the two traits of system localization and peak blade responses.

# EXPERIMENTAL INVESTIGATION ON PERIODIC FORCED VIBRATIONS OF A BLADED DISK

## *I. Introduction and Overview*

### *1.1 Background*

*1.1.1 High Cycle Fatigue of Turbine Engine Blades.* Bladed disk assemblies are comprised of numerous near-identical turbine blades attached to a central hub. Should the blades and disk be manufactured from a single metal piece, it may be referred as a blisk. A typical jet engine contains dozens of these blisks. Further, bladed disks must be manufactured to operate across broad engine RPM ranges and varied airflow inlet speeds. Hence, the performance of gas turbines are largely dependent upon the structural integrity of these sophisticated components. A modern jet engine contains rotating blisks interspersed among multiple fixed stators. The aeroelastic and aeroacoustic loading effects upon the blisks are largely unknown (35). However, it is understood that external forcing occurs from the periodic wakes created by the fixed stators at integer multiples of the bladed disk's rotational frequency, commonly called engine order. When a natural frequency of the blisk coincides with an integral engine order frequency, the blades are excited into a resonant condition. At these forcing frequencies, turbine blades can experience high stress and strain. Prolonged or repeated exposure to these dynamic loads can cause vibration-induced fatigue (11), otherwise known as High Cycle Fatigue (HCF).

HCF advances turbine blade wear and degradation with potentially catastrophic damage to jet engine subsystems. Man-hour losses, increased operational costs and repetitive engine servicing are all symptoms of the HCF problem. Several hundred incidents of aircraft engine failure in the past three decades have been reported due to the effects of HCF. Furthermore, HCF has been explicitly identified as the primary unexpected engine

failure mode from 1989 to 1994 (39). Because of these circumstances, HCF of turbomachinery rotors is a persistent problem which has drawn much attention in recent years.

**1.1.2 The Behavior of Bladed Disk Assemblies.** In attempt to resolve bladed disk assembly HCF, researchers have developed a multitude of numerical, analytical and statistical models in hope of gaining insight into the phenomena. Although these analysis techniques have been well documented (35)(36), a brief mention of significant themes contained throughout the studies will be explored.

**1.1.2.1 Rotationally Periodic Structures.** Bladed disks belong to a unique class of systems known as rotationally periodic structures (RPS). An RPS example is shown in Figure 1.1. Since they consist of spatially repetitive substructures, cyclic symmetry is a convenient, frequent assumption made when analyzing RPS dynamics (31). With this assumption, all system substructures are geometrically and dynamically similar. In the case of a bladed disk assembly, this implies all the blades are identical, uniformly spaced and the hub is symmetric. If these criteria are met, the RPS is known as a tuned, or ordered, system.

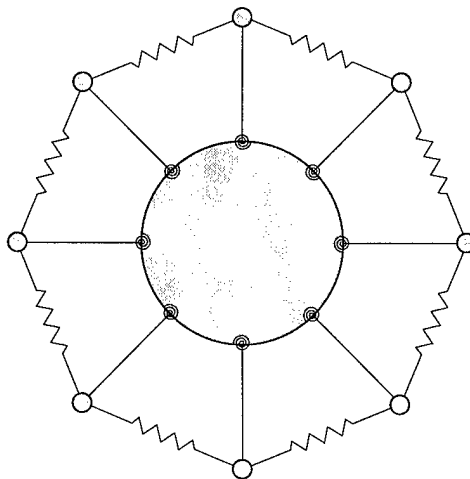


Figure 1.1 Example RPS Model

A bladed disk possesses several modal vibration families. Each family, or band, correlates to a specific cantilever bending mode. There are as many linear modes within a

modal band as substructures. Further, an ordered RPS possesses a distinguishing vibration characteristic. At system modes, a constant phase difference exists between all substructures with varying participation from each substructure. However, the system response is always symmetric in appearance. These vibrations are known as global, or extended modes (38).

Early structural analyses took advantage of RPS cyclic symmetry to drastically reduce the computational cost involved with examining an entire disk assembly. Cyclic symmetry enabled engineers to uncouple the blisk equations of motion and reduce the problem scope to that of analyzing a single blade (31).

**1.1.2.2 Mistuning of Bladed Disk Assemblies.** If bladed disk assemblies were perfectly tuned, the HCF problem plaguing aircraft engines would be significantly reduced. Unfortunately, globally extend modes throughout a blisk are an unattainable ideal. In actual assemblies, the cyclical symmetry of a blisk is destroyed by material, manufacturing and geometrical irregularities among the turbine blades. Normally, the blade differences are in the form of mass, stiffness or damping variances (27). These random discrepancies are known as mistuning, or system disorder (5). Hence, the repeated nature of the substructures is lost, and a qualitatively different dynamic behavior than that of the tuned assembly results.

**1.1.2.3 Mode Localization Phenomena.** The rotational periodicity breakdown can transition the global modes to that of highly localized ones. Instead of vibration energy being equally diffused throughout all substructures, energy can become concentrated to a few specific substructures. In an extreme case, the energy can become focused onto a single blade. This phenomena, known as mode localization, results in the steady state amplitude of some blades being much larger than those of a perfectly tuned system (6). Furthermore, research has shown mode localization and peak blade deflections are amplified by weak or variable inter-blade coupling throughout the blisk (40). This coupling may be structural or aerodynamic in nature.

Consequently, the problem of HCF is magnified, with blisk structural failures occurring at a much accelerated rate. The sensitivity of bladed disks to mistuning perturbations is extreme. For instance, blade amplitude increases over 100% have been observed in blade natural frequency variations of less than 2% from blade to blade (27).

**1.1.2.4 Advanced Techniques to Analyze Mistuning Effects.** Since mistuning effects dramatically impact bladed assembly dynamics, their existence must be included in any analysis if reliable solutions to severe vibratory response amplitudes are to be found. However, the obvious approach of formulating a complete finite element model (FEM) to replace the cyclic symmetry method is an extremely expensive, if not impossible undertaking. Therefore, useful models must take alternative, less complex approaches to predict blade amplitude levels.

Current research efforts of bladed disk forced response are divided into three primary categories (29).

1. The first category consists of obtaining system behavior approximations through statistical analyses. Monte Carlo simulations or other probabilistic methods are typically utilized for these studies.
2. The second strategy is of a deterministic type, where models are generated, mistuned and the results analyzed. Here, reduced order models (ROM) are often used which reduce computational effort while providing reasonable accuracy of mistuning effects.
3. Lastly, underlying mechanisms such as blade damping are studied to determine which factors influence mistuning sensitivity.

Unfortunately, the results found among these studies can vary substantially. In general, there is a lack of agreement toward the degree of system localization and vibratory increase resulting from mistuning effects. These areas of inconsistency include, among others, blade amplitude magnification levels, blade of greatest vibration response and blade damping effects (35). For these (and other) aspects of forced response behavior, it is often difficult to surmise which findings or combinations are accurate and which directions future research should focus.

Furthermore, a vast majority of these models are mathematical in nature. Little research into the forced vibration behavior has been investigated experimentally. Since HCF is an operational problem on real-life turbomachinery rotors, perhaps an approach that relied on experimental data would yield results presumably consistent to that observed in practice.

## ***1.2 Experimental Analysis of Blisk Forced Response***

Instead of attempting forced vibrations measurements on a full scale operational jet engine fan, this study offers a novel approach to investigate bladed disk forced response behavior. The proposal has three main elements:

1. A model fan reduced in dynamic scale from an operational jet engine fan will be fabricated. This model will capture the dynamic variations of repeated structures, yet be simple enough to keep modal identification uncomplicated.
2. Attempting to collect vibration data by spinning this generic fan between stators in a high speed wind tunnel would be of enormous cost. Therefore, rather than rotate the test article, the forcing input will be revolved. To replicate aerodynamic disturbances produced by the fixed stators, magnets attached to the outer diameter of a spinning flywheel will interact with like-polarity magnets epoxied to the model fan blades. The flywheel magnets will be properly distributed around the flywheel rim to simulate an engine order of interest.
3. Accelerometer transducers glued to the blade tips will measure the dynamic vibratory response. These response signals will, in turn, be analyzed by an appropriately configured data acquisition system.

Several tests involving different mistuning sets and engine orders will be conducted to determine the validity of such an approach. The success of this measurement system would offer a new method to further progress the field of characterizing bladed disk dynamics.

### ***1.3 Periodic Forcing Function***

A fluctuating axial force, periodic in nature, must be successfully modeled to localize the blisk modes. The experiment proposes an original design to recreate this forcing environment. Repulsive magnetic pulses will replicate wakes impinging upon the blades. These repelling pulses will occur via magnets bonded to both the disk and a rotating flywheel. The flywheel angular velocity will be generated from electric motor torque. By having magnets around the flywheel rim, forcing frequencies are multiples of flywheel rotational speed. The number of impulses a blade experiences during one full rotation of the flywheel will mimic an engine order. Theoretically, resonant excitation of blade modes will occur when an engine order coincides with a blisk natural frequency. Although the approach appears reasonable, verification that this mimicked forcing input is similar to that witnessed by operational blisks must be incorporated into the experimental procedure.

### ***1.4 Response Measurement with Norm Scales***

A fundamental consideration of the experiment procedure is the ability to quantify the degree of localization and peak blade deflections each of these experimental cases would produce. Past approaches have focused around determining relative blade amplitudes through an amplitude magnification factor (6). This is the ratio of maximum mistuned forced response amplitude to the maximum tuned forced response amplitude. While this method is suitable for deterministic models where a tuned system response is available, the likelihood a highly tuned response could be extracted from the model test fan is remote. Further, dual effects of localization and peak blade deflections are not considered by this ratio alone. A more rounded methodology to assess forced response behavior is required.

This study proposes modal length scales to measure the forced vibration behavior. By defining a length scale, different frequency responses can be readily compared (7). Previous research utilized modal length scales to measure localization occurrences in radially deflected ribs with great success (8)(7). These length scales were combinations of the two norm, four norm and infinity norm of a given mode shape's deflections at a specific distance from the center of a radial rib reflector.

Because of their uniqueness, some background is necessary in the area of norm scales (8). The  $n^{th}$  norm of a mode is found by the following relation:

$$norm_n = \frac{\sqrt[n]{\sum_{i=1}^N |\psi_i|^n}}{N} \quad (1.1)$$

The norm taken is denoted by  $n$ , an individual component of a specified mode is given by  $\psi_i$ , and the total number of components in a mode is represented with  $N$ . Lower norms are not as sensitive to extreme differences between values for a given set. Norms can range from 1 to  $\infty$ , from the mean to absolute maximum of a set, respectively. Lower norms are useful for characterizing system behavior as a whole. Higher norms are best for understanding significant deviations in system behavior. In the extreme, the infinity norm is useful to quantify severe deflections, hence potential substructure failures, in a system.

Of significant importance, modal length scales were previously only used to investigate free vibrations (8)(7). For these free response studies, the norm scales were normalized by the ordered system norms. Since modal frequencies do not exist in the same sense for forced vibrations, this study will disregard the normalization step. Rather, norm scales evaluated at a certain frequency will be compared relative to surrounding modal family frequencies to determine the degree of localization. As a result, resolving when a system transitions from a global to a localized state is a somewhat subjective undertaking. Localization and maximum blade deflections will be measured with the four/two and infinity/two norm scales, respectively. With this approach, the appropriateness of these norms for forced vibrations will be assessed. The four/two and infinity/two norm scale relations are shown in Equations 1.2 and 1.3 respectively. Normalized four/two and infinity/two values are given by Equations 1.4 and 1.5.

$$\Lambda_{kfour}(x) = \frac{(\sum_{i=1}^N \nu_i^2(x))^2}{\sum_{i=1}^N \nu_i^4(x)} \quad (1.2)$$

$$\Lambda_{k\infty}(x) = \frac{\sqrt{\sum_{i=1}^N \nu_i^2(x)}}{\max(|\nu(x)|)} \quad (1.3)$$

$$L_{four}(x) = \frac{\Lambda_{four}(x)}{\Lambda_{0four}(x)} \quad (1.4)$$

$$L_{\infty}(x) = \frac{\Lambda_{\infty}(x)}{\Lambda_{0\infty}(x)} \quad (1.5)$$

## 1.5 Thesis Overview

This thesis has two principle objectives:

1. Determine the validity of the proposed forced vibration excitation system through experimental testing.
2. Extract any information gained from the forced response experiments to augment the existing body of knowledge on mistuned bladed disk vibrations.

To accomplish these goals, the remaining study has been segmented into five chapters:

1. First, Chapter 2 contains a numerical demonstration to familiarize the reader with the cyclic mistuning phenomena. A numerical model similar to the experiment test article will be constructed. Tuned and mistuned configurations of this model will be created. The subsequent free and forced responses will be investigated, discussed and compared.
2. Next, Chapter 3 presents the experimental test article and laboratory equipment used throughout the study. Details of the test methods, model bladed disk and flywheel excitation system will be specifically discussed.
3. A compilation of the experimental procedure, including analysis methods and problems encountered during testing are included in Chapter 4. The input forcing function produced by the flywheel excitation system will be fully characterized. This information will be used to determine the viability of the forcing input methodology and to help understand the test article response. Next, using the test equipment, the model fan will undergo modal parameter identification. This procedure will include both individual blades and the complete disk assembly. Mistuning cases for free

and forced vibrations analysis will also be determined. Following this, the forced response behavior of the test article will be collected through various flywheel magnet configurations (i.e. engine orders) and the mentioned mistuning sets.

4. The forced response mistuning results are discussed in Chapter 5. Forced vibrations data sets will be compared amongst themselves and, where feasible, prior research and this study's numerical model results.
5. Lastly, Chapter 6 contains significant conclusions of the study, lessons learned and opportunities for future research.

Since the figures generated in some sections are too numerous to present without distracting the reader, two appendices were created. These appendices provide complete documentation of all tests conducted. Appendix A contains extraneous input forcing function graphs. Supplemental figures of forced vibration experimental cases can be found in Appendix B.

## ***II. Forced Response Numerical Demonstration***

To better acquaint the reader with the forced localization phenomena, a lumped parameter numerical model will first be analyzed. Understanding an RPS forced localization response originates with examining behavior of a perfect, cyclical system. Therefore, the ordered system's free mode shapes and frequency distributions will initially be determined. These free response characteristics will be useful when exploring the forced response attributes of the same system. In both free and forced response analyses, mistuning cases will be introduced to disrupt the perfect system symmetry and bring about free and forced localization behavior.

### ***2.1 Eight Mass RPS Model***

The model system considered for the numerical analysis is shown in Figure 2.1. It is similar to a closed loop pendulum system used in prior research (8). However, it is representative of the eight bladed disk test article used throughout the experimental portion of this study.

Each blade is modeled as a lumped mass,  $m$ , at a distance  $l$  from the hub outer diameter.  $N$  is the total number of substructures (i.e blades). Blade coupling stiffness and individual blade stiffness is represented by the even and odd stiffness coefficients  $k$ , respectively. Coupling can be thought of as the strength of blade to blade influence (29). The blade-disk interface is assumed rigid, thus all inter-blade coupling occurs through the blade coupling coefficients. The tuned values for the mass ( $m$ ), length ( $l$ ), blade stiffness ( $k_b$ ), and coupling stiffness ( $k_c$ ) are 1, 1, 1 and 0.1 respectively.

***2.1.1 Equations of Motion.*** Lagrangian dynamics will be used to obtain the discrete equations of motion (23). The Lagrangian,  $L$ , is defined as the difference between the system kinetic and potential energy,  $T$  and  $V$  respectively. Specific derivatives are taken with respect to system generalized coordinates in what are known as Lagrangian equations:

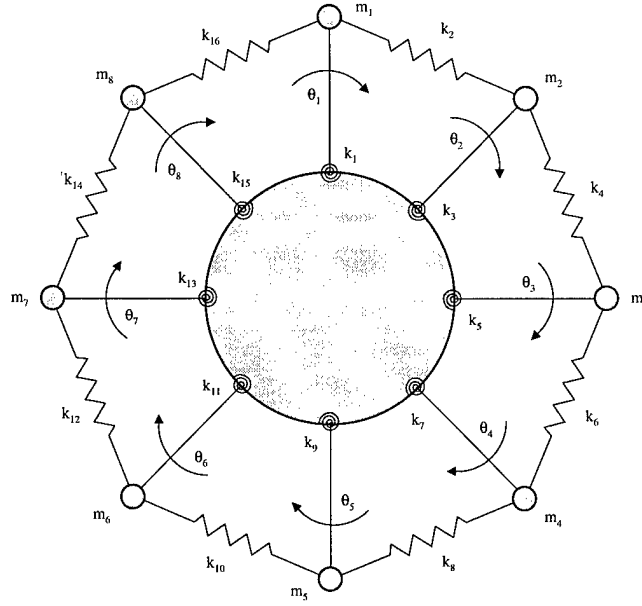


Figure 2.1 Eight Mass RPS Model

$$L = T - V \quad (2.1)$$

$$\frac{d}{dt} \left( \frac{\partial L}{\partial \dot{\theta}_i} \right) - \frac{\partial L}{\partial \theta_i} = Q_i^n \quad (2.2)$$

Lagrange's equations of motion are generated equal in quantity to system degrees of freedom. The non-conservative forces,  $Q_i^n$ , for this system are zero. However, expressions for the kinetic and potential energy must be derived.

Both the potential energy and kinetic energy expressions can be obtained through vector dynamics. Figure 2.2 shows a two mass system representative of two system blades with length  $l$ , separated by  $45^\circ$ . The kinetic energy function,  $T$ , is comprised of the individual blade masses kinetic energy. Linearizing the equation with a small angle assumption, arc lengths  $l\theta$  are substituted for horizontal tip displacements. The kinetic energy function is:

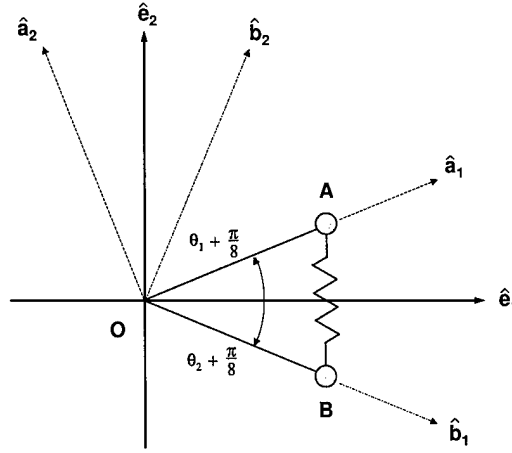


Figure 2.2 Vector Diagram for Equations of Motion

$$T = \frac{1}{2} \sum_{i=1}^8 (m_i \dot{\theta}_i^2 l^2) = m_1 \dot{\theta}_1^2 l^2 + m_2 \dot{\theta}_2^2 l^2 + m_3 \dot{\theta}_3^2 l^2 + m_4 \dot{\theta}_4^2 l^2 + m_5 \dot{\theta}_5^2 l^2 + m_6 \dot{\theta}_6^2 l^2 + m_7 \dot{\theta}_7^2 l^2 + m_8 \dot{\theta}_8^2 l^2 \quad (2.3)$$

To develop the potential energy function,  $V$ , spring deflections between the blades must be determined. Referring to Figure 2.2, a deflection is equal to the magnitude of the vector  $\vec{r}_{AB}$  minus the unstretched length of the spring. The spring deflection vector is obtained by adding the position vectors of both masses, as shown in Equations 2.4 through 2.7.

$$\vec{r}_{AO} = l \hat{a}_1 = l \cos \left( \theta_1 + \frac{\pi}{8} \right) \hat{e}_1 + l \sin \left( \theta_1 + \frac{\pi}{8} \right) \hat{e}_2 \quad (2.4)$$

$$\vec{r}_{BO} = l \hat{b}_1 = l \cos \left( \theta_2 - \frac{\pi}{8} \right) \hat{e}_1 + l \sin \left( \theta_2 - \frac{\pi}{8} \right) \hat{e}_2 \quad (2.5)$$

$$\vec{r}_{AB} = \vec{r}_{AO} - \vec{r}_{BO} \quad (2.6)$$

$$\begin{aligned} \vec{r}_{AB} = & \left[ l \cos \left( \theta_1 + \frac{\pi}{8} \right) - l \cos \left( \theta_2 - \frac{\pi}{8} \right) \right] \hat{e}_1 \\ & + \left[ l \sin \left( \theta_1 + \frac{\pi}{8} \right) - l \sin \left( \theta_2 - \frac{\pi}{8} \right) \right] \hat{e}_2 \end{aligned} \quad (2.7)$$

Taking the magnitude of  $\vec{r}_{AB}$ :

$$\begin{aligned} |\vec{r}_{AB}| &= \left[ l^2 \left[ (2 - 2 \cos \left( \theta_1 + \frac{\pi}{8} \right) \cos \left( \theta_2 - \frac{\pi}{8} \right) - 2 \sin \left( \theta_1 + \frac{\pi}{8} \right) \sin \left( \theta_2 - \frac{\pi}{8} \right)) \right] \right]^{\frac{1}{2}} \\ &= l \left[ 2 - 2 \cos \left( \theta_1 - \theta_2 + \frac{\pi}{4} \right) \right] \\ &= 2l \left[ \sin \left( \frac{\theta_1 - \theta_2}{2} + \frac{\pi}{8} \right) \right] \\ &= 2l \left[ \sin \left( \frac{\theta_1 - \theta_2}{2} \right) \cos \left( \frac{\pi}{8} \right) + \cos \left( \frac{\theta_1 - \theta_2}{2} \right) \sin \left( \frac{\pi}{8} \right) \right] \end{aligned} \quad (2.8)$$

Again using the small angle assumption, a linear relationship can be created between  $\theta_1$ ,  $\theta_2$  and  $l$ :

$$|\vec{r}_{AB}| \approx l \left[ (\theta_1 - \theta_2) \cos \left( \frac{\pi}{8} \right) + 2 \sin \left( \frac{\pi}{8} \right) \right] \quad (2.9)$$

The unstretched length of the spring,  $X$ , is determined through the law of sines:

$$\begin{aligned} \frac{\sin \left( \frac{\pi}{4} \right)}{X} &= \frac{\sin \left( \frac{3\pi}{8} \right)}{l} \\ X &= 2 \sin \left( \frac{\pi}{8} \right) \end{aligned} \quad (2.10)$$

The total deflection,  $\Delta X$ , is the difference between  $\vec{r}_{AB}$  and  $X$ :

$$\Delta X = l \left[ (\theta_1 - \theta_2) \cos \left( \frac{\pi}{8} \right) \right] \quad (2.11)$$

The total potential energy of the system is the summation of energy stored in both the blade and coupling springs. Using  $\Delta X$  as the change in distance for each inter-blade stiffness coefficient and the small angle assumption for every blade stiffness coefficient yields:

$$\begin{aligned} V = & \frac{1}{2} \cos^2 \left( \frac{\pi}{8} \right) \left[ k_2(\theta_1 - \theta_2)^2 + k_4(\theta_2 - \theta_3)^2 + k_6(\theta_3 - \theta_4)^2 + k_8(\theta_4 - \theta_5)^2 \right. \\ & + k_{10}(\theta_5 - \theta_6)^2 + k_{12}(\theta_6 - \theta_7)^2 + k_{14}(\theta_7 - \theta_8)^2 + k_{16}(\theta_8 - \theta_1)^2 \left. \right] + \frac{1}{2} k_1 \theta_1^2 \\ & + \frac{1}{2} k_3 \theta_2^2 + \frac{1}{2} k_5 \theta_3^2 + \frac{1}{2} k_7 \theta_4^2 + \frac{1}{2} k_9 \theta_5^2 + \frac{1}{2} k_{11} \theta_6^2 + \frac{1}{2} k_{13} \theta_7^2 + \frac{1}{2} k_{15} \theta_8^2 \end{aligned} \quad (2.12)$$

Returning to Equations 2.1 and 2.2, the tuned system Equations of Motion can now be obtained:

$$[M]\{\ddot{\theta}\} + [K]\{\theta\} = 0 \quad (2.13)$$

Where the eight individual EOMs are:

$$\begin{aligned} m_1 l^2 \ddot{\theta}_1 + \left[ \cos \left( \frac{\pi}{8} \right) l^2 (k_2 + k_{16}) + k_1 \right] \theta_1 - \left[ \cos \left( \frac{\pi}{8} \right) l^2 k_2 \right] \theta_2 - \left[ \cos \left( \frac{\pi}{8} \right) l^2 k_{16} \right] \theta_8 &= 0 \\ m_2 l^2 \ddot{\theta}_2 - \left[ \cos \left( \frac{\pi}{8} \right) l^2 k_2 \right] \theta_1 + \left[ \cos \left( \frac{\pi}{8} \right) l^2 (k_4 + k_2) + k_1 \right] \theta_2 - \left[ \cos \left( \frac{\pi}{8} \right) l^2 k_4 \right] \theta_3 &= 0 \\ m_3 l^2 \ddot{\theta}_3 - \left[ \cos \left( \frac{\pi}{8} \right) l^2 k_4 \right] \theta_2 + \left[ \cos \left( \frac{\pi}{8} \right) l^2 (k_6 + k_4) + k_1 \right] \theta_3 - \left[ \cos \left( \frac{\pi}{8} \right) l^2 k_6 \right] \theta_4 &= 0 \\ m_4 l^2 \ddot{\theta}_4 - \left[ \cos \left( \frac{\pi}{8} \right) l^2 k_6 \right] \theta_3 + \left[ \cos \left( \frac{\pi}{8} \right) l^2 (k_8 + k_6) + k_1 \right] \theta_4 - \left[ \cos \left( \frac{\pi}{8} \right) l^2 k_8 \right] \theta_5 &= 0 \\ m_5 l^2 \ddot{\theta}_5 - \left[ \cos \left( \frac{\pi}{8} \right) l^2 k_8 \right] \theta_4 + \left[ \cos \left( \frac{\pi}{8} \right) l^2 (k_{10} + k_8) + k_1 \right] \theta_5 - \left[ \cos \left( \frac{\pi}{8} \right) l^2 k_{10} \right] \theta_6 &= 0 \\ m_6 l^2 \ddot{\theta}_6 - \left[ \cos \left( \frac{\pi}{8} \right) l^2 k_{10} \right] \theta_5 + \left[ \cos \left( \frac{\pi}{8} \right) l^2 (k_{12} + k_{10}) + k_1 \right] \theta_6 - \left[ \cos \left( \frac{\pi}{8} \right) l^2 k_{12} \right] \theta_7 &= 0 \\ m_7 l^2 \ddot{\theta}_7 - \left[ \cos \left( \frac{\pi}{8} \right) l^2 k_{12} \right] \theta_6 + \left[ \cos \left( \frac{\pi}{8} \right) l^2 (k_{14} + k_{12}) + k_1 \right] \theta_7 - \left[ \cos \left( \frac{\pi}{8} \right) l^2 k_{14} \right] \theta_8 &= 0 \end{aligned}$$

$$m_8 l^2 \ddot{\theta}_8 - \left[ \cos\left(\frac{\pi}{8}\right) l^2 k_{16} \right] \theta_1 - \left[ \cos\left(\frac{\pi}{8}\right) l^2 k_{14} \right] \theta_7 + \left[ \cos\left(\frac{\pi}{8}\right) l^2 (k_{16} + k_{14}) + k_1 \right] \theta_8 = 0 \quad (2.14)$$

**2.1.2 Free Response of Eight Mass RPS.** The reader may inquire why researching free response characteristics is necessary when forced excitations are the focus of the study. Free response analysis can lend helpful insights into a system's sensitivity to mistuning. Further, if any relationships between the free and forced response behavior can be established, pursuing the more simple free response analysis may be sufficient. Consequently, it may be unnecessary to proceed with the more costly forced response analysis.

**2.1.2.1 Tuned System Analysis.** Performing an eigenanalysis (22) on the tuned system EOMs yields the eigenvectors and natural frequencies shown in Figure 2.3. These eigenvectors are the blade deflections of a perfectly tuned system, commonly known as the extended mode shapes.

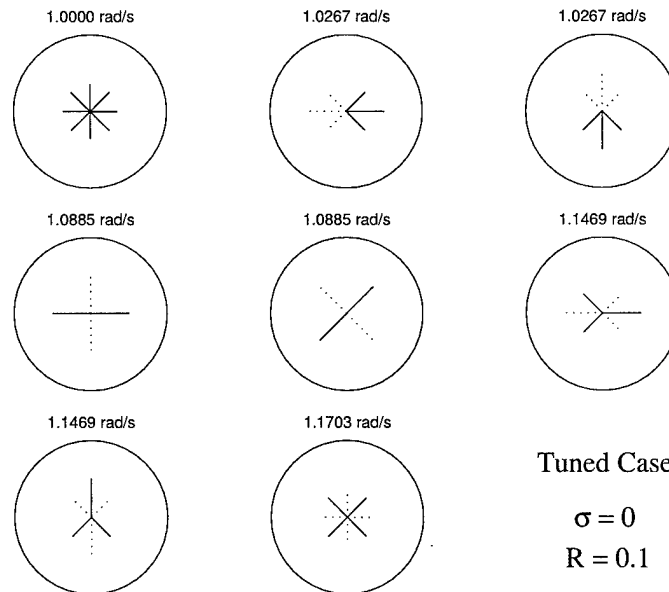


Figure 2.3 Natural Frequencies and Mode Shapes of Tuned Eight Mass RPS

Blade one is represented by the radial line in the 12 o'clock position. The remaining blades are incrementally numbered clockwise. The length of a radial line represents the normalized modal length of a particular blade, with all modes normalized by the first component. Solid lines are vibrating 180° out of phase with the dotted lines.

As expected, for an RPS, there are as many mode shapes as substructures,  $N$ . Because the ordered system features perfect cyclic symmetry, Pierre and Murthy (31) suggest that the mode shapes be mathematically written according to Equation 2.15:

$$e_j = \frac{1}{\sqrt{N}} \left[ 1, e^{i\phi_j}, \dots, e^{i(N-1)\phi_j} \right]^T \quad \phi_j = \frac{2\pi(j-1)}{N} \quad j = 1, \dots, N \quad (2.15)$$

Where  $\phi_j$  is the interblade phase angle for the  $j$ th mode.

Each tuned mode has constant interblade phase angles between substructures. Motion of the  $j$ th mode can be modeled as waves traveling through the assembly with a phase change  $\phi_j$  at each blade. Consequently, the mode shapes of the eight mass RPS can be described in the following manner:

- The first mode shape,  $e_1$ , corresponds to a zero interblade phase angle where all blades vibrate in-phase with the same amplitude.
- The fifth mode shape,  $e_5$ , has an interblade phase angle equal to  $\pi$ , meaning adjacent blades vibrate out of phase with equal amplitudes.
- Modes with  $\phi_j$  values between 0 and  $\pi$  contain waves that travel backwards through the assembly.
- Modes with  $\phi_j$  values between  $\pi$  and  $2\pi$  possess waves that travel forward through the assembly.
- A pair of forward and backward traveling waves have the same number of (traveling) nodal diameters and are referred as 'standing waves'.

A more common approach to labeling the mode shapes of the first type of modal group (bending and torsion) is by the number of nodal diameters (35). Hence, the mode with the

least number of nodal diameters is the first mode while the mode with the largest number of nodal diameters would be the eighth mode. This is the representation of Figure 2.3, where the lowest natural frequency is the first mode and the largest natural frequency the eighth mode. In addition, as the modal group number increases, the number of nodal circles increases. This means the second torsion mode would have one nodal circle, the third torsion mode would have two nodal circles, and so on.

It is important to note that the first, second and third nodal diameter patterns are repeated by two neighboring modes, respectively, in Figure 2.3. These dual nodal patterns are also accompanied by repeated natural frequency values. Each such pair is referred to as a 'double' mode. This mode pair is identical in every respect except orientation, where they are orthogonal. This occurs because of the 'standing' wave phenomena mentioned by Pierre and Murthy. The first and eighth mode are the exception, each possessing a unique natural frequency.

**2.1.2.2 Mistuned System Analysis.** Unfortunately, the tuned system analysis is an idealization since mistuning exists, to some degree, in all cyclic structures. To simulate the effects of mistuning on the eight mass RPS system free response, the nominal stiffness of each blade was altered with slight stiffness additions or deductions. Further, the standard deviation (STD),  $\sigma$ , of the mistuned values was based on the statistical results of Castanier and Pierre (6). These researchers showed the maximum amplitude magnification factor of a bladed compressor stage with various random mistuning strengths peaked at an STD of approximately 0.01. These findings were particular to forced vibration behavior but, for the purposes of this study, can also be applied to free analysis. Using this criteria, a random mistuning pattern with  $\sigma \cong 0.01$  was created in MATLAB® using the `rand` function. A random mistuning pattern with an STD of nearly 0.03 was also created to demonstrate the effects of a more severely mistuned case. For both scenarios, several stiffness sets were produced until a mean close to the nominal blade stiffness value, 1, was found. The two selected mistuning patterns are shown in Table 2.1.

Pierre (41) also recognized the effects of inter-blade coupling on mode localization. Therefore, in addition to the mistuning sets, four coupling ratios ( $R = k_c/k_b$ ) of 0, 0.01, 0.1

Blade #	Case 1	Case 2
1	0.0122	0.0367
2	0.0003	-0.0043
3	-0.0003	0.0189
4	-0.0038	0.0365
5	-0.0117	-0.0105
6	-0.0012	-0.0373
7	-0.0074	-0.0148
8	0.0126	-0.0352
Mean	0.0001	-0.0013
Std. Dev. ( $\sigma$ )	0.0086	0.0293

Table 2.1 Blade Stiffness Mistuning Distributions for Eight Mass RPS

and 0.5 were selected to represent none, very weak, weak and strong inter-blade coupling respectively. These coupling ratios will be combined with the mistuning cases to study their dual effects on free localization. Overall, six combinations of mistuning/coupling were created and are shown in Table 2.2. These cases are sufficient to demonstrate the fundamental characteristics of free localization.

	Case					
	I	II	III	IV	V	VI
$k_b$ Std. Dev. ( $\sigma$ )	0.0086	0.0293	0.0086	0.0293	0.0086	0.0086
Coupling Ratio ( $R$ )	0.1	0.1	0.01	0.01	0	0.5

Table 2.2 RPS Mistuning and Inter-Blade Coupling Cases

The stiffness matrix created in the EOMs derivation was appropriately altered with these mistuning patterns and inter-blade coupling values. The EOMs were recreated and an eigenanalysis (22) performed on each case. To begin with a situation of mild mistuning, Figure 2.4 demonstrates the effects of Case I. Like the tuned analysis, mode shapes have been normalized by the first modal component.

Several observations are immediately noticeable. As seen, when slight mistuning is introduced, vibration energy is no longer equally distributed among the blades, but tends to concentrate (i.e localize) in certain blades. The implication is some blades undergo amplitudes larger than their tuned counterparts while others experience less. Furthermore, the passband of the natural frequencies spread further apart compared to the tuned variation. Of particular interest the repeated modes, while maintaining much of their orthogonality,

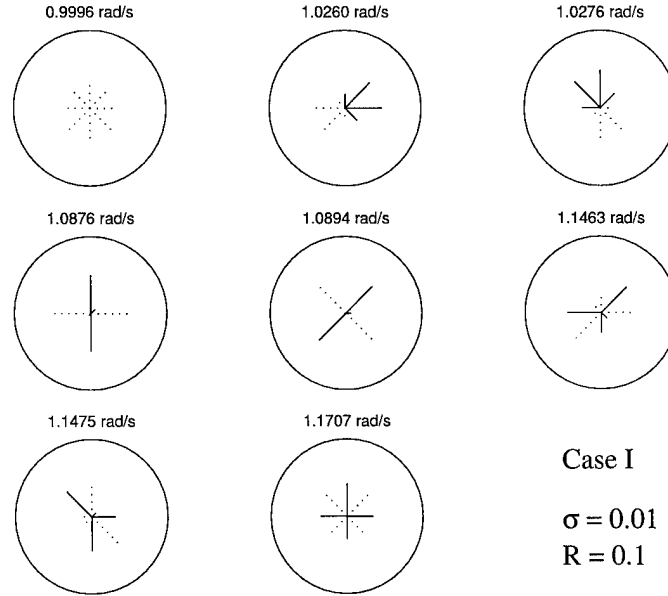


Figure 2.4 Modal Characterization of Mistuned Eight Mass RPS - Case I

suffer a distinct natural frequency split. Hence, a new 'double' mode, close in frequency, emerges in place of the 'single' mode. This phenomena is commonly referred to as mode splitting. Consequently, all RPS modes are visually detectable. Typically, increasing  $\sigma$  will intensify mode localization. For illustration, increased mistuning effects are depicted in Figure 2.5 with Case II.

Figure 2.5 portrays the extent of frequency splitting among repeated modes is related to the degree of mistuning. The orthogonal property of these once repeated modes, still somewhat noticeable, further deteriorates. Similarly, the frequency bandwidth containing all modes expands beyond that of Case I. Also, the apparent randomness of blade amplitudes is more noticeable with a larger mistuning standard deviation. Adjusting the blade coupling ratio will have even more pronounced effects on free localization. This is proven by examining Figures 2.6 and 2.7 where  $R$  is altered to reflect a very weakly coupled RPS.

In both cases, the reduction in system coupling drastically reduced the bandwidth of the system modes. Any orthogonality between the once double modes is now completely lost. Also, the modes are more strongly localized than in any previous case. For instance, some Case IV modes near complete localization around a single blade. As Pierre (41) demonstrated, the ratio of mistuning to inter-blade coupling strength primarily governs

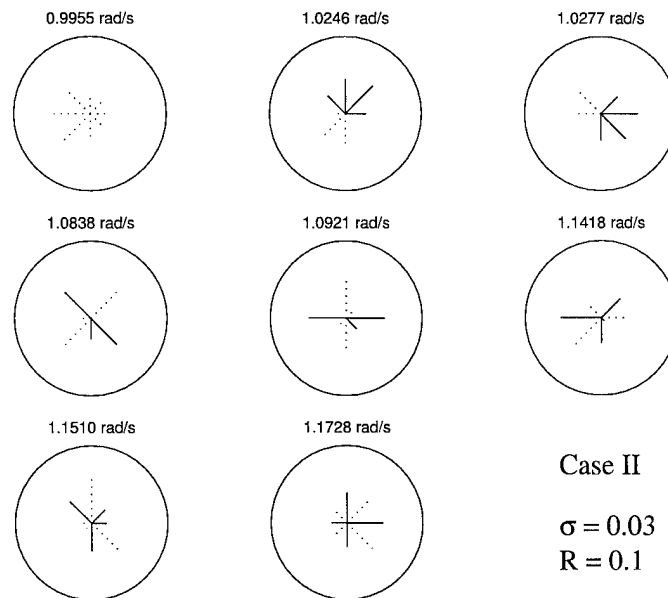


Figure 2.5 Modal Characterization of Mistuned Eight Mass RPS - Case II

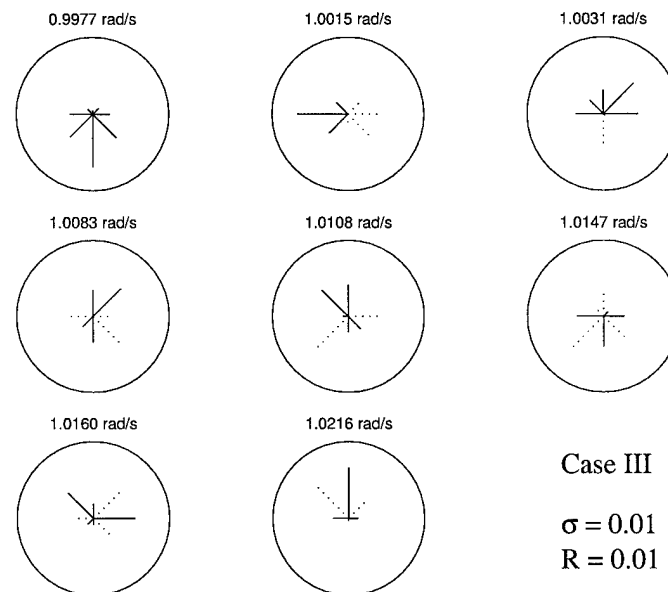


Figure 2.6 Modal Characterization of Mistuned Eight Mass RPS - Case III

the degree of free localization. Typically, mode localization increases monotonically with this ratio. Case IV, therefore, should exhibit more severe mode localization than Case III. This is exactly what occurred.

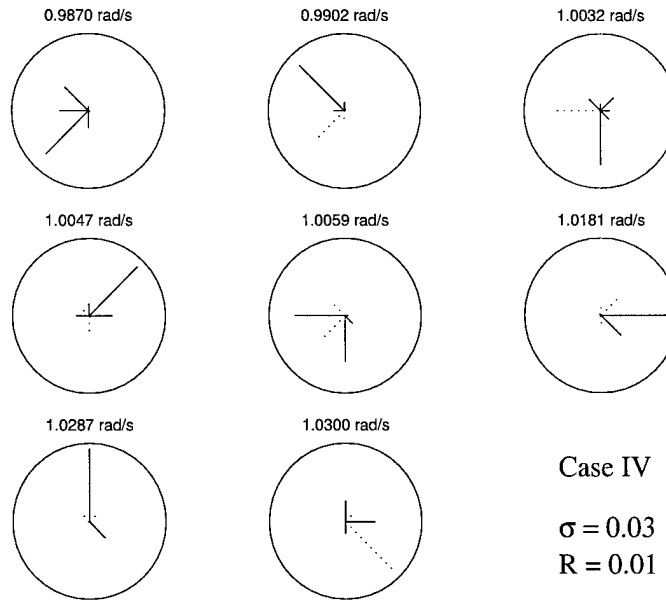


Figure 2.7 Modal Characterization of Mistuned Eight Mass RPS - Case IV

Of academic interest are cases of inordinate inter-blade coupling values. Specifically, what will result if no coupling exists or, the other extreme, a case of very high coupling strength. These situations are investigated with the final two cases. The modal characteristics of Cases V and VI are shown in Figures 2.8 and 2.9.

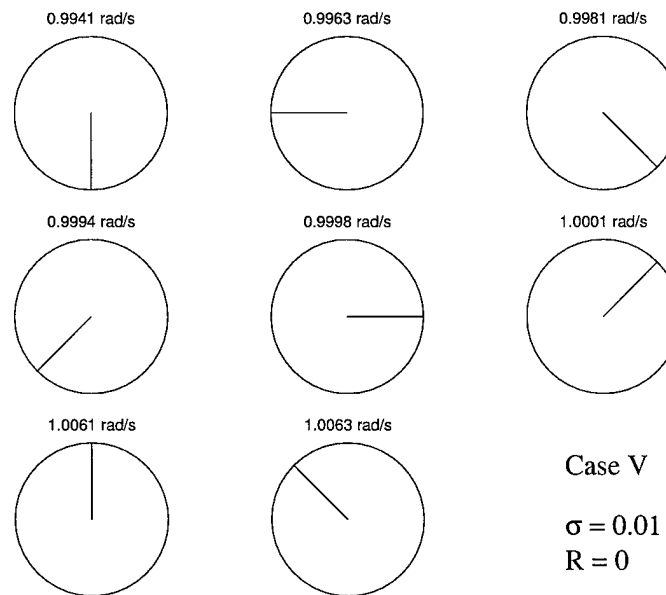


Figure 2.8 Modal Characterization of Mistuned Eight Mass RPS - Case V

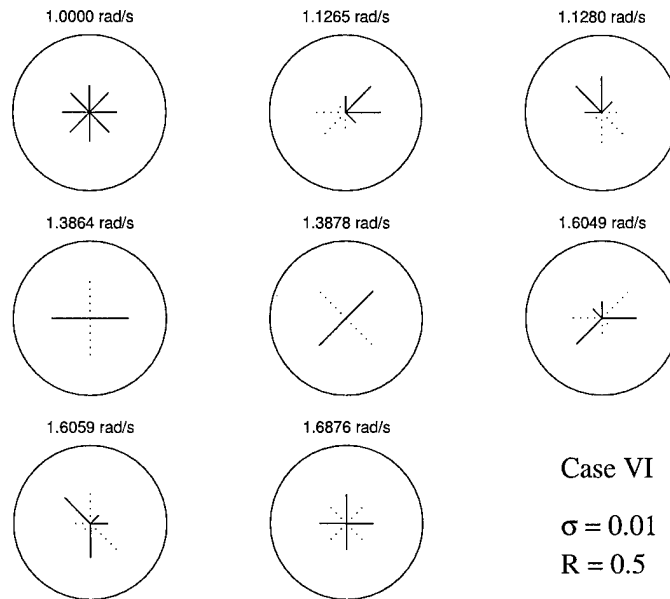


Figure 2.9 Modal Characterization of Mistuned Eight Mass RPS - Case VI

A lack of inter-blade coupling, as illustrated in Figure 2.8, produces completely localized blades, each at its own independent natural frequency. Since the RPS is uncoupled, each blade can be thought of as an individual oscillator with no participation from surrounding substructures. High levels of coupling, shown in Figure 2.9, result in behavior similar to the tuned system. Modes are largely extended and little localization occurs. Considering the small mistuning to coupling ratio of Case VI, this reduced ratio agrees with the more global state observed.

To quantitatively evaluate localization levels, Table 2.3 lists the four/two norm and infinity/two norm scale values of all modes for each mistuning/coupling case. All norm scales values are normalized by their respective ordered mode.

Table 2.3 further verifies the mode localization discussions presented for all six cases. Low four/two norm scale values are indicative of more severe mode localization, and correlate very well to the high mistuning to coupling ratio introduced by Pierre. Additionally, low infinity/two norm scale values are connotative of large blade deflections, hence increased stresses and fatigue. It is intuitive that greater free localization is synonymous with larger blade amplitudes. Hence, both norm scales should be in good agreement, following similar trends among all cases. Analyzing the table, this is the observed pattern. Of

	Case I		Case II		Case III		Case IV		Case V		Case VI	
Mode	$L_{four}$	$L_{\infty}$	$L_{four}$	$L_{\infty}$	$L_{four}$	$L_{\infty}$	$L_{four}$	$L_{\infty}$	$L_{four}$	$L_{\infty}$	$L_{four}$	$L_{\infty}$
1	0.951	0.859	0.706	0.711	0.411	0.512	0.286	0.451	0.125	0.354	0.998	0.968
2	0.991	1.037	1.006	0.985	0.702	0.752	0.342	0.598	0.188	0.500	0.999	1.068
3	1.012	1.042	1.037	1.029	0.903	0.889	0.497	0.718	0.188	0.500	1.002	1.062
4	1.027	1.006	1.173	1.038	1.211	0.905	0.382	0.559	0.250	0.500	1.001	1.000
5	1.022	0.997	1.126	0.992	1.131	0.874	0.734	0.755	0.250	0.500	1.001	1.000
6	1.001	1.001	0.869	0.873	0.971	0.890	0.327	0.582	0.188	0.500	1.001	1.052
7	0.988	0.979	0.869	0.873	0.851	0.915	0.249	0.538	0.188	0.500	0.998	1.045
8	0.941	0.845	0.758	0.750	0.340	0.533	0.219	0.412	0.125	0.354	0.998	0.964

Table 2.3 Four/Two and Infinity/Two Norm Scale Values of RPS Mistuning Cases

interest, the modes at the edges of the modal band appear most susceptible to localization. This observation is consistent with previous numerical and experimental findings (7)(30).

**2.1.2.3 Free Response Synopsis.** Some general conclusions can be drawn from the preceding free response analysis.

1. First, when mistuning is introduced, system modes can rapidly transition from a globalized to localized state. Mistuning causes significant alteration of the base system's eigenstructure. A distinct frequency split occurs between the repeated natural frequencies of the ordered system. Also, the extended free modes shapes disintegrate into isolated resonances among the substructures.
2. Second, the level of localization is highly dependent on two variables, mistuning strength and inter-blade coupling levels. The larger the mistuning to coupling ratio, the more pronounced the localization becomes. Also, increased amounts of mistuning lead to a proportional widening range of RPS natural frequencies. Similarly, increased inter-blade coupling values radically separate the modal frequencies.
3. Finally, norm scale values can adequately track the degree of free localization and extreme blade deflections between system modes.

Equipped with a balanced understanding of the RPS free response, the forced response behavior can next be examined. Similarities between the two responses will be discussed, in addition to unique forced vibration characteristics.

### **2.1.3 Forced Response of Eight Mass RPS.**

**2.1.3.1 EOM alterations.** Some modifications to the EOMs introduced earlier must be performed to analyze forced vibrations of the same RPS system. To obtain finite resonant amplitudes, the EOMs were augmented with a damping coefficient matrix,  $[C]$ . Due to the lightly damped nature of the experimental system, damping ratios ( $\zeta$ ) will be approximated at 0.002. A steady state external forcing vector,  $[F]$ , was also added to create the new EOMs:

$$[M]\{\ddot{\theta}\} + [C]\{\dot{\theta}\} + [K]\{\theta\} = [F] \quad (2.16)$$

For the steady state response the external forcing vector, which portrays a harmonic excitation differing only in phase from blade to blade (41), can be modeled:

$$[F] = \tilde{f}e^{j\omega t} \begin{Bmatrix} 1 \\ e^{j\phi_1} \\ \vdots \\ e^{j\phi_{N-1}} \end{Bmatrix} \quad (2.17)$$

where the inter-blade phase angle,  $\phi$ , is

$$\phi_i = \frac{2\pi c(i-1)}{N} \quad i = 1, \dots, N \quad (2.18)$$

The variable  $c$  is the engine order excitation, while  $\tilde{f}$  is the force acting on a lone substructure.

The damping matrix,  $C$ , is formed with the following relationships:

$$C = \Phi \left[ 2\zeta (\Phi^T K \Phi)^{\frac{1}{2}} \right] \Phi^T \quad (2.19) \quad \Phi^T C \Phi = \begin{bmatrix} 2\zeta\omega_1 & & 0 \\ & \ddots & \\ 0 & & 2\zeta\omega_N \end{bmatrix} \quad (2.20)$$

Where  $\Phi$  is the system mass normalized modal matrix.

The new forced response EOMs were then converted to a state-space realization of the form:

$$\begin{bmatrix} \dot{\theta} \\ \ddot{\theta} \end{bmatrix} = \begin{bmatrix} 0 & I \\ -K & -C \end{bmatrix} \begin{bmatrix} \theta \\ \dot{\theta} \end{bmatrix} + \begin{bmatrix} 0 \\ F \end{bmatrix} \quad (2.21)$$

Coefficient  $I$  represents the identity matrix. This state variable model was numerically solved with the MATLAB® `ode45` function. The steady state solution of all substructures was found throughout a frequency sweep encompassing the RPS natural frequencies. Blade amplitudes were collected after the transients died out, approximately 3000 seconds after forced excitation commenced. Small frequency steps of 0.005 rad/s ensured high resolution of the data solution. At each frequency increment, the largest blade amplitude of all substructures was retained. This was done for both the tuned and mistuned system.

As with the free response analysis, the fewest number of cases to demonstrate the main characteristics of forced vibrations are desired. This is particularly true of forced vibration characterization due to the great expense involved with conducting a multiple case numerical survey. Returning to the mistuning STD suggested by Castanier and Pierre (6),  $\sigma \cong 0.01$ , with a coupling ratio  $R = 0.1$  yielded results comprehensive of the forced response phenomena. It should be remembered, as mentioned in Chapter 1, varying mistuning levels, inter-blade coupling ratios, blade number and damping coefficients can have profound influences on forced response behavior (40)(29). However, altering these parameters would shed little further insight toward the investigation beyond increasing complexity of cases studied. They have therefore been ignored and only the Case I mistuning/coupling set was used for the forced analysis portion. This particular case should provide a good representation of the blisk test article and offer legitimate comparisons between numerical and experimental models.

**2.1.3.2 Tuned and Mistuned System Analysis.** Five sets of equations were numerically solved, each for different forcing vectors representing the second, third, fourth, sixth and twelfth engine orders, E.O. for short. For better comparison of the

tuned and mistuned systems, Figure 2.10 shows the steady state Root Mean Square (RMS) maximum overall blade forced vibration of both responses.

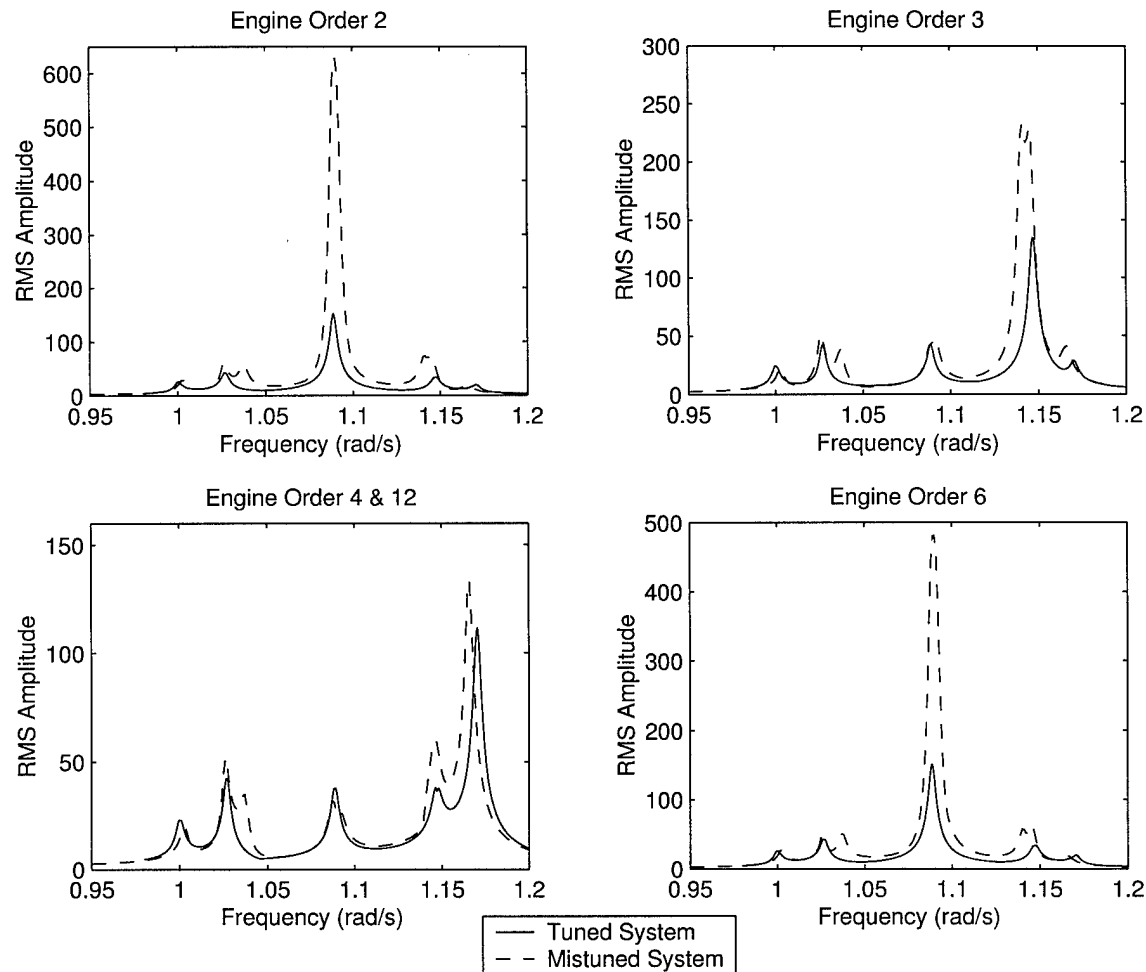


Figure 2.10 Maximum Blade Amplitude of Mistuned Eight Mass RPS - Case I

The first most noticeable observation in Figure 2.10 is the distinct increase in maximum blade amplitude between the tuned and mistuned systems, reaching a near 500% increase for E.O. 2. In particular, these peak amplitudes are centered around a single excitation frequency. For multi-span beams, Hodges (14) verified a confinement of forced vibration energy at the source of excitation. For RPS forced response behavior, this confinement effect can be correlated to maximum peaks occurring at modes not orthogonal to a given engine order. As an example, the inter-blade phase angle given by Equation 2.18 for E.O. 6 is  $180^\circ$ . This angle is equal to the inter-blade phase angle of the seventh eigenvector

located at 1.089 rad/s according to Equation 2.15. Consequently, the largest blade amplitude is achieved at this forcing frequency for E.O. 6. Similar occurrences are witnessed throughout all engine orders. In theory, the remaining orthogonal modes of the tuned system should not experience local peak deflections. However even these modes exhibit some degree of peak vibration, hence non-orthogonality, which may be an indication of an ill-conditioned system.

Another noticeable forced response characteristic is different peak amplitudes at varied engine order. For instance, E.O. 4 affects much less response at its respective non-orthogonal mode than E.O. 2. Pierre further observed that the largest peak amplitude amongst engine orders would occur for  $c/N = 1/2$  (40). This is consistent with the model RPS, where E.O. 4 experiences the lowest peak blade response. Obviously, engine order must be considered in forced response design in order to avert subcomponents from exceeding a critical failure amplitude.

Further, duplicate forcing vector inter-blade phase angles will produce identical vibrational behavior throughout a frequency spectrum. Returning to Equation 2.18, E.O. 4 and E.O. 12 have identical phase angles of  $180^\circ$ . Hence, both engine orders produce the same forced response, shown in Figure 2.10.

Despite these mentioned distinctions, certain similarities are shared across both free and forced system responses. For instance, the mode splitting phenomena observed in the free response also occurs in the forced analysis. With this frequency split, two amplitude peaks appear in the vicinity of the once present single mode resonance. Also common to both responses, some mistuned substructures undergo less deflections than those of the corresponding tuned case.

Since only the substructure of maximum amplitude is plotted in Figure 2.10, the remaining subcomponents experience less intense vibration movement. With individual blade deflections varying across the forcing frequency bandwidth, the mistuned localization effects for each engine order should change across the same frequency spectrum. To quantitatively observe these differences, the localization norm values are portrayed in Fig-

ure 2.11. As stated in Chapter 1, since there is no ordered response for comparison, the four/two and infinity/two norm scales are not normalized.

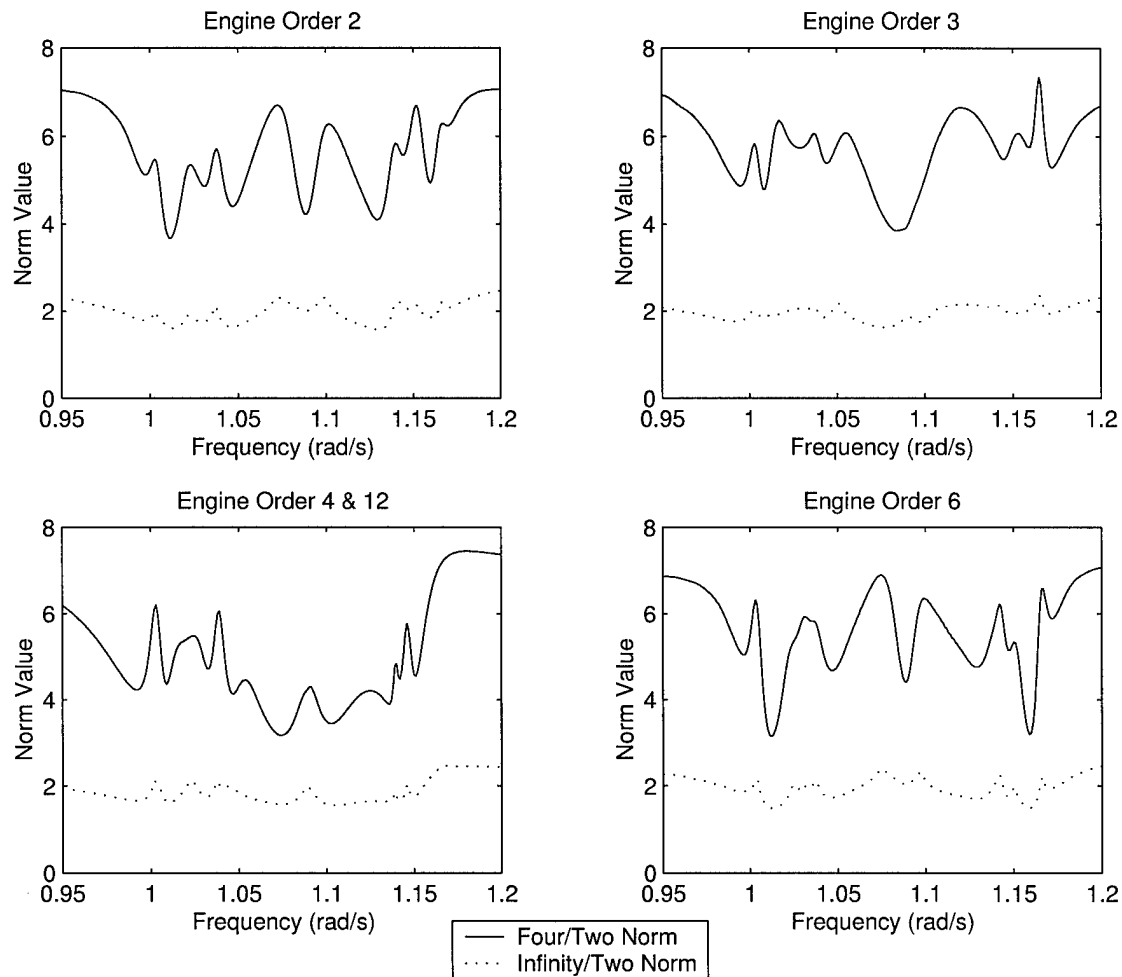


Figure 2.11 Four/Two and Infinity/Two Norm Scales of Mistuned Eight Mass RPS - Case I

The four/two and infinity/two norm values fluctuate across the frequency spectrum, indicating localization's dependency on input frequency. Like the free response, the norm values seem to follow similar trends. Accordingly, different engine orders produce varying localization responses. Of major significance, neither the four/two nor infinity/two norm scales necessarily reach minimum values at maximum blade deflections. Although maximum blade deflections are not a primary focus in a free response analysis, abnormally high amplitudes can lead to substructure failures if prolonged exposure to certain

forcing frequencies persists. Hence, initial estimations of the norm scales question their usefulness for complete forced response behavior examination. A possible explanation for this behavior may be lack of the normalization step used during free response analysis. However, these first impressions indicate the norm scales' effectiveness needs to be further scrutinized during experimental tests.

**2.1.3.3 Forced Response Synopsis.** Like the free response, forced vibrations of an RPS are highly sensitive to mistuning perturbations. However, with the introduction of an external force and damping, several additional response phenomena not observed in the system's free analysis occur.

1. Blade amplitudes reach peak magnifications in the vicinity of tuned and mistuned system natural frequencies, yet the degree to which mistuned deflections exceed nominal tuned amplitudes is a function of not only mistuning but, among others, the external forcing vector phasing (i.e engine order). As noted, several other parameters affect the RPS system forced response but were not investigated in this analysis.
2. Throughout a frequency band, forced localization effects are significant and varying, similar to the norm values at free response system modes. Yet, unlike free vibrations, the confinement of energy in certain blades at forcing frequencies equal to system modal frequencies can raise the possibility of subcomponent failure.
3. Unfortunately the norm scale values, while excellent in monitoring degrees of forced localization, did not appear to correlate well to peak substructure deflections.

## **2.2 Summary**

In this chapter, the reader was briefly oriented with the RPS mistuning phenomena. Through a numerical model, the key effects of mistuning on free and forced response system behavior were investigated. Due to the RPS model's relative simplicity, not all results witnessed here are expected to be replicated by the experimental bladed disk. However, the results gathered from this investigation will be compared, where suitable, to the experimental analysis.

### ***III. Experimental Methodology and Equipment***

#### ***3.1 Experimental Test Methods***

Two different types of test cycles were conducted on the bladed disk. The first method determined the free modal characteristics of the test article. The second method entailed using the flywheel excitation system to induce forced vibrational behavior. Although a detailed outline of both methods are included with the data acquisition system description, a brief overview of these testing methodologies is presented below.

**3.1.1 Free Response Method.** Modal testing is the fundamental methodology used to characterize free response characteristics of any test structure. Simply stated, modal testing is the processes employed to determine a structure's response properties via controlled vibration inputs. From this, a mathematical model of a test article's structural dynamics can be obtained and manipulated (12). A generic block diagram of this method is depicted in Figure 3.1 and elaborated below.

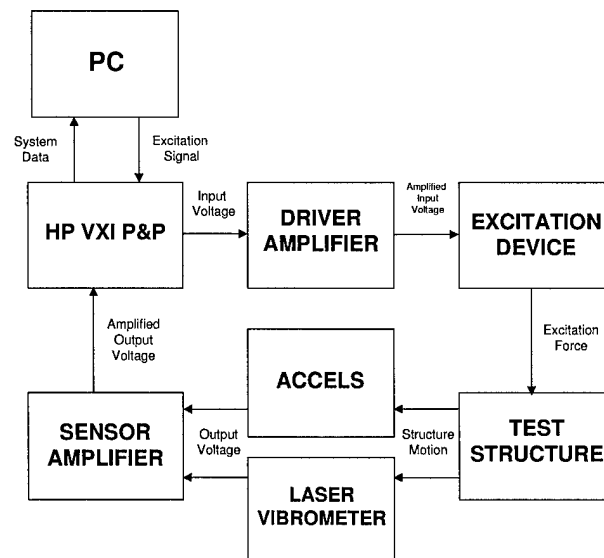


Figure 3.1 Modal Testing Experiment Setup Block Diagram

As illustrated in Figure 3.1, a Pentium 233MHz Personal Computer (PC) was used as the user's interface to the test system. This PC would receive output signals and deliver input signals through an excitation device. The interface between the PC and the remaining equipment was a Hewlett Packard (HP) VXI Plug and Play system. A complete test cycle occurred as follows. PC generated signals were sent to the HP VXI bus. These signals underwent amplification and were converted to some input motion (i.e. force) through driving actuators attached to the test structure. The test structure experienced a physical deformation from this force, and transducers measured the subsequent response. The transducers' low voltage signal was amplified before returning to the HP. Finally, the HP sent the signal to the PC for analysis.

**3.1.2 Forced Response Method.** Figure 3.2 shows a schematic of the second test approach for forced response experiments. Although similar to the first method, two key differences exist. First, blisk forced response behavior, not modal properties, were the test objectives. Second, the excitation signals were not generated from the PC/HP hardware. Rather, a manually operated voltmeter delivered a voltage input to the flywheel motor. The motor converted this voltage into torque, which was transferred to the flywheel. Repulsive forces occurred between the spinning flywheel magnets and blade magnets, hence generating a periodic input. The remaining sequence of events were identical to those of the free response approach.

## **3.2 Experimental Equipment**

The model test fan was the centerpiece of every experimental test. However, several additional hardware components were needed to support all aspects of experimentation. These included the flywheel excitation system, PZT actuators, data acquisition system, laser vibrometer, accelerometer transducers and force sensor.

**3.2.1 Test Article Description.** To accurately model dynamic responses of rotating bladed disks, a representative test specimen was needed that embodies the

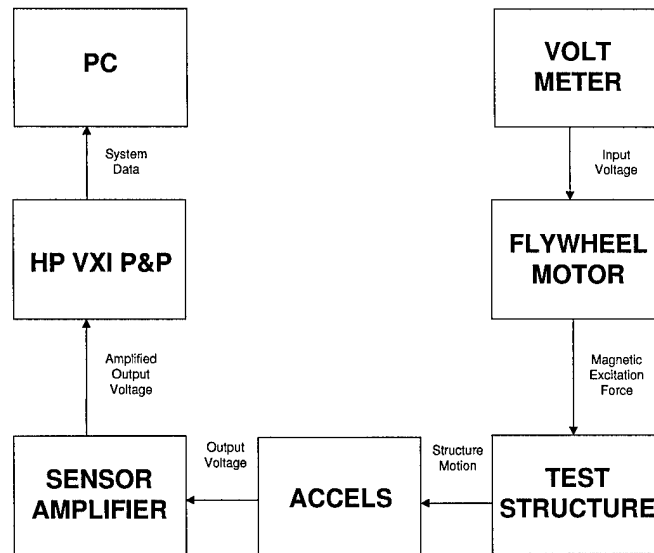


Figure 3.2 Forced Response Experiment Setup Block Diagram

significant properties found in such cyclic structures. Therefore, the design requirements of the test article included (15):

- Geometry of disk dynamically similar to an operational fan
- Enough blades to capture the complexities of cyclic structures
- Small enough aspect ratio to excite modes of interest
- Light coupling of vibration energy between blades through disk hub
- Similar modulus of elasticity-to-density ratio of titanium alloy, the material commonly founded in operational bladed disk assemblies

An eight bladed disk, shown in Figure 3.3, with flat plates representing the blades was selected. More blades would increase the difficulty to identify closely spaced modes. A similar test model was used by researchers for bladed disk modal tests (15). The blades were epoxied into shallow slots at equal spatial intervals along the disk. Further, each blade's stagger angle was 45°. Although flat plates were adequate to display the general structural dynamics of cyclic turbomachinery rotors, it is worth noting that they were a

very simplified replication of real-life turbine blades. Predominant factors that exist in operational rotor blades not exhibited by the flat plates include (33):

- Taper of blade cross section area
- Pretwist of the blades
- Asymmetry of the blades
- Shrouding
- Lacing Wire
- Root Fixing

Including factors such as these would have complicated the experimental analysis without providing any additional dynamic characteristics of interest. These factors were therefore ignored, although they could be considered for future test articles.

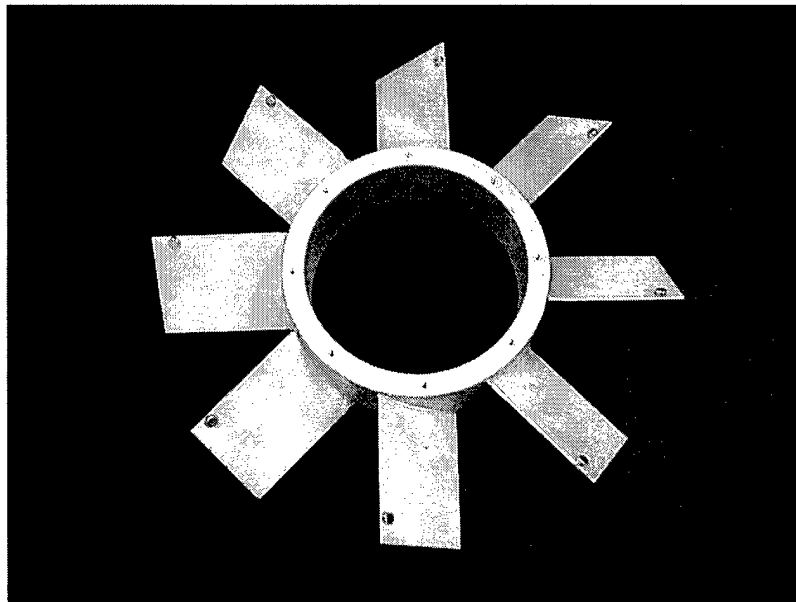


Figure 3.3 Bladed Disk Test Article

As seen in Figure 3.3, glued to the forward face (facing flywheel) of each blade was a small magnet. Located on the counterclockwise edge, 0.5 inches from the blade tip, it was the location of the excitation input for each individual blade. A small ring of teflon was affixed to the front of the disk hub in case the flywheel detached from the spinning motor

shaft during operation. A teflon surface was a better suited barrier to contact the spinning flywheel as opposed to the metal hub. The blades and hub were made of aluminum. The model fan was securely bolted to a bracket. This bracket, in turn, was mounted to an axial rod permanently affixed to a pneumatic isolated optical table.

Two test articles needed to be fabricated for the experiment. The first article was severely mistuned due to weakly brazed slots and small sections of missing blade mass occurring from the manufacturing process. During preliminary testing, these factors yielded widely spread modal families and excessive stress localization beyond that desired for a slightly mistuned test article. An example of these unfavorable features is shown in Figure 3.4, which displays a flawed root of this bladed disk. As a result, a second test article with the same physical characteristics was constructed and used throughout the experiment. Followup research of the first test article is recommended to further study localization effects on a more seriously mistuned system.



Figure 3.4 Sample Blade Root of Ill-Constructed Test Article

### ***3.2.2 Excitation System Descriptions.***

***3.2.2.1 Flywheel Excitation System.*** The means to provide forced periodic excitation of the system were through a uniquely configured flywheel and motor

generator. Figure 3.5 shows the flywheel. The outer diameter was 12 inches, identical to the bladed disk. However, 12 spatially periodic circular slots ( $30^\circ$  separation), each 0.75 inches in diameter, were machined into the flywheel. The radius of each circular slot from the flywheel center was 5.5 inches. Within each slot, a small aluminum or magnet disk, equal in diameter to the slot, could be inserted. The magnets and aluminum disks were arranged depending on the type of forcing function (i.e engine order) desired. A 0.375 inch hole was tapped through the center in order to mount the flywheel upon an electric motor shaft. Four miniature screws through the center hub diameter connected the flywheel to the motor shaft.

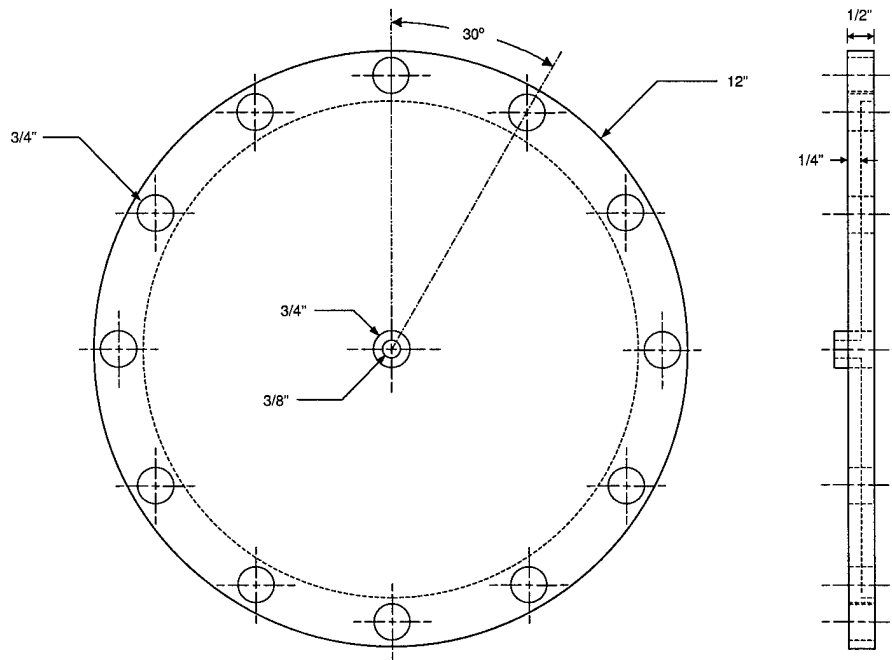


Figure 3.5 Excitation System Flywheel

Driving this motor shaft was a Electro-Craft Motor Model 3622-4B-N. The motor was capable of generating up to 20000 Revolutions Per Minute (RPM) with a voltage input range of  $\pm 10V$ . To directly measure the motor RPM real-time, an HP Two Channel Optical Encoder (Model HEDS-550X) was connected to the motor circuitry. This encoder translated rotary motion into electrical pulses, which were interpreted by an HP Tachome-

ter installed in the HP VXI system. The motor was powered manually by a ME Model 83-B-829 Digital Voltmeter capable of  $\pm 40V$ .

The entire motor/flywheel structure was housed inside an aluminum test stand. Aluminum was chosen for its easy manufacturing capabilities and non-interference with magnetic fields. The excitation system was mounted upon a cantilever table bolted into a wall next to the isolated optical table. The cantilever table was also made from aluminum. Threaded holes were drilled into the table and test stand in order to bolt them together during test runs. Through these measures, undesirable ground vibration, noise or rattling to the test article was eliminated. Figure 3.6 portrays this entire setup.

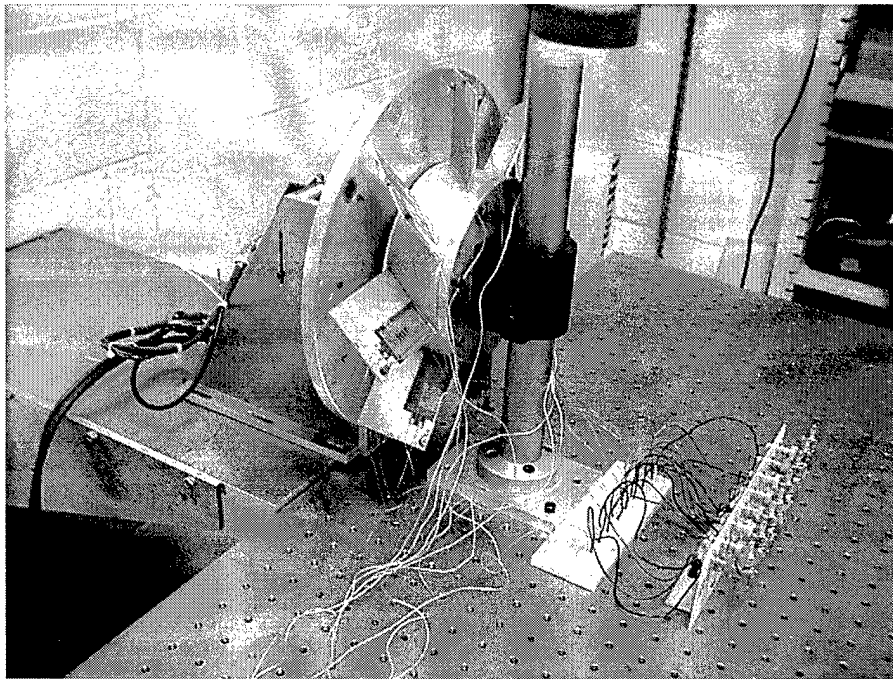


Figure 3.6 Flywheel as Input Force to Blisk

During flywheel-motor operation, a plexiglass housing surrounded the mounted blisk and flywheel excitation system as a safety precaution. If any magnets, aluminum plugs or bolts detached from the flywheel or blades during forced response testing, they would literally become high speed projectiles. The plexiglass shielded the operator from these object and consequently from any harm.

**3.2.2.2 Piezoelectric Strain Actuators.** To convert the electrical excitation signal into mechanical motion during modal testing, eight Active Controls Experts (ACX) model QP10Ni Quickpack IDE strain actuators were selected to drive each disk blade. A drawing of the actuator is shown in Figure 3.7.

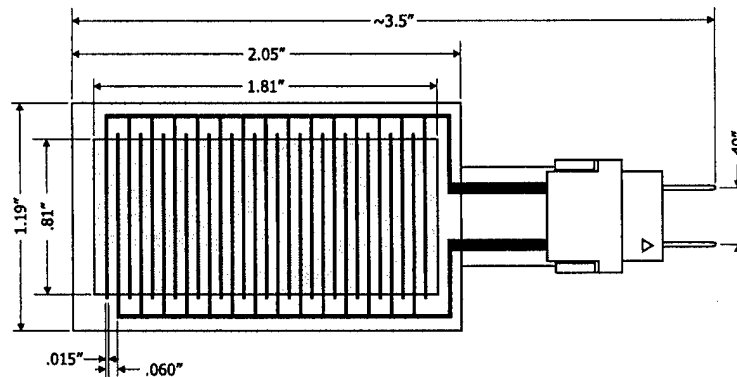


Figure 3.7 QP10Ni Strain Actuator Drawing (2)

The actuator consisted of a single active piezoelectric element packaged in a polyimide skin (2). These PZTs were bonded to the blades with M-bond 2000, a common strain gauge adhesive. At the root, each Quickpack was situated on the blade surface facing away from the flywheel, along the counterclockwise edge as Figure 3.8 shows. This positioning enabled excitement of both bending and torsional modes.

Due to its unique construction, this particular piezoelectric actuator was more efficient over other strain actuators. Unlike traditional piezoelectric devices which are poled transversely through the material thickness, the QP10Ni poling direction is oriented along the material length by a special interdigital electrode pattern. Since the QP10Ni polarization is parallel rather than perpendicular to the generated electric field, the stronger  $k_{33}$  coupling coefficient is utilized rather than the weaker  $k_{31}$  coupling coefficient. This translates into more than twice the electromechanical coupling efficiency of the QP10Ni Quickpacks compared to standard strain actuators (2).

Excitation of the PZT actuators was achieved through the ACX 1224 QuickPack Power Amplifier (1). Eight separate amplifiers were acquired, one for each PZT actuator. For all experiments, the amplifier voltage and current settings were set to 200V and 50mA

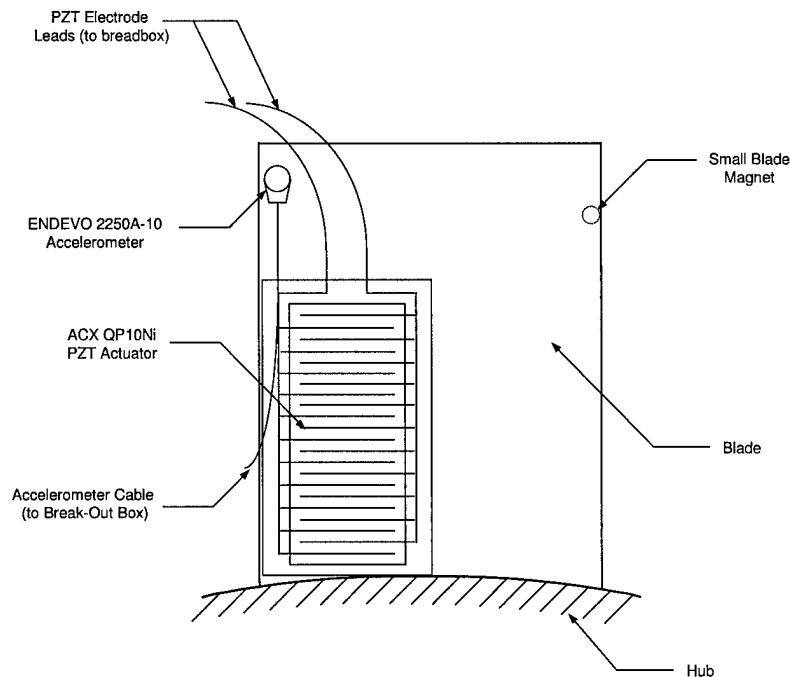


Figure 3.8 Blade Test Configuration

respectively. The amplifiers supplied input voltage through a BNC Connector Board. Positive and negative leads from the BNC connectors were connected to a breadboard. In turn, the PZT Quickpack leads were appropriately wired to the correct BNC connectors through the breadboard. The BNC board conveniently allowed the user to select which PZT Quickpack was driven for each test. A picture of these connections is shown in Figure 3.9.

**3.2.3 Data Acquisition System.** Figure 3.10 displays the hardware and software components of the data collection system. The Graphical User Interface (GUI) software utilized throughout the experiment was the SignalCalc 620 Dynamic Signal Analyzer. Created by the Data Physics Corporation, it was a modal acquisition and vibrational analysis toolbox. This program served two primary functions. First, it generated output voltage to drive excitation devices. Second, it collected time response data from sensors attached to an excited test structure. The software then manipulated these input and output signals to produce several graphical representations. These visuals, including frequency

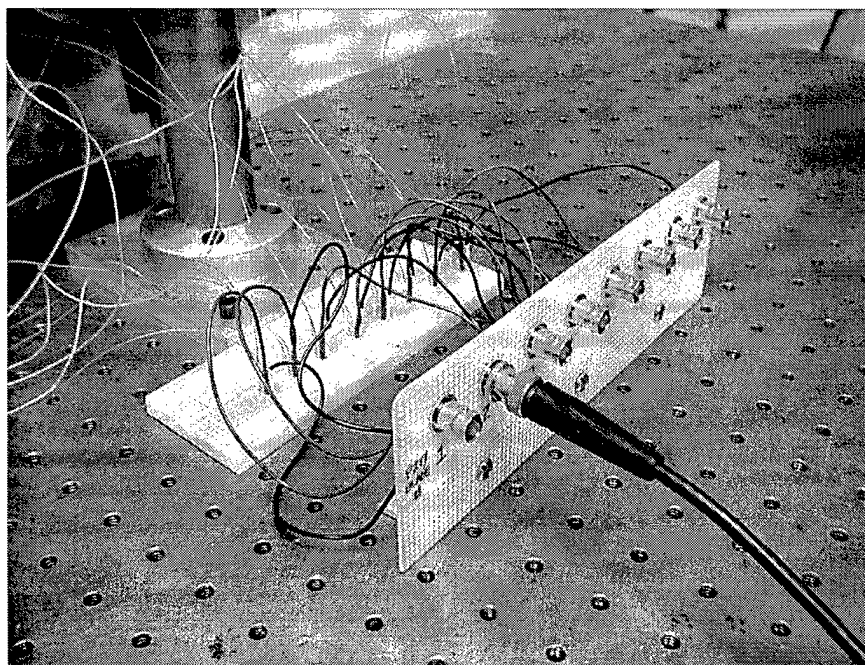


Figure 3.9 BNC Supply Board

response functions (FRF), power spectral densities and coherence plots, were constructed to characterize the modal behavior of the actual test structure.

The software interface between SignalCalc and the data acquisition hardware was a Dynamic Linked Library (DLL) driver. The DLL allowed the SignalCalc software to initiate instrument calls to the HP hardware. The DLL and SignalCalc programs reside on the host PC hard drive. The physical interface between this software and the HP equipment was an Adaptec® AHA-8940 1394-to-PCI Host Adapter card, installed into a PCI slot within the PC.

In order to best convey the process of free response data acquisition, the succeeding discussion involves a user excitation input which will flow through the PC based GUI software program and pass through the various hardware and software elements. The process ends with output data returned to the user through the same GUI software. The only alteration for forced vibration tests is that the input voltage signal is manually controlled instead of generated by the PC/HP system.



and output sensor signals retrace the input signal steps until received by the PC. Lastly, the GUI software plots this response data for the user to analyze.

**3.2.4 Sensor Descriptions.** Since accurate measurements of both the input to the structure and its subsequent response were essential, reliable transducers were important elements of any vibration test conducted. Therefore, piezoelectric accelerometers and a laser vibrometer were selected to measure system response levels while a force sensor was utilized to quantify the input forcing function.

**3.2.4.1 Accelerometers.** Eight accelerometers measured the force vibration response of the blisk blades. The accelerometers used were ENDEVCO® model 2250A-10 with a nominal sensitivity 10 mV/g and a range of  $\pm 500g$ . These ENDEVCO® accelerometers were selected for three primary reasons. First, the frequency range of the accelerometers was 4 to 15000 Hz. The frequency band measured throughout the experiments varied from 30 to 1600 Hz, well within the accelerometer usable range. Also, with a nominal weight of 0.4 grams each, the change in mass properties for each blade was minimal. Lastly, the accelerometers proved reliable in experiments by prior Master Degree candidates (8) and students in laboratory work.

Each accelerometer was attached, using M-Bond 2000 adhesive, on the blade surface facing away the flywheel. Further, each was located along the counterclockwise edge, 0.5 inches from the blade tip. This ensured that any electrical interference from the small magnets would be eliminated. This arrangement was previously shown in Figure 3.8. To reduce accelerometer cable tension and whip, the electrical leads were taped to blade edges and the pneumatic test table throughout the experiment.

Measurements were taken at room temperature, 65 to 75°F with magnitude error of approximately 1% (9). The accelerometer voltage amplifier was a Kistler® model 5124A Piezotron Coupler. The accelerometer signal passed through this amplifier onto the HP breakout boxes.

**3.2.4.2 Laser Vibrometer.** Unfortunately, while the accelerometers were suitable sensors for the majority of vibration experiments, they were inappropriate

for determining the individual blade natural frequencies and mode shapes. Due to the blades light mass and thin cross section, repositioning the accelerometers around each blade collection point would alter total mass distribution for each measurement. Therefore, a non-contact, non-intrusive method of collecting response data for building deflected blade shapes was needed. To remedy this problem, an Ometron Laser Doppler Vibrometer, model VH300, was operated for constructing mode shapes and determining initial modal frequency groupings. A picture of the vibrometer is shown in Figure 3.11.

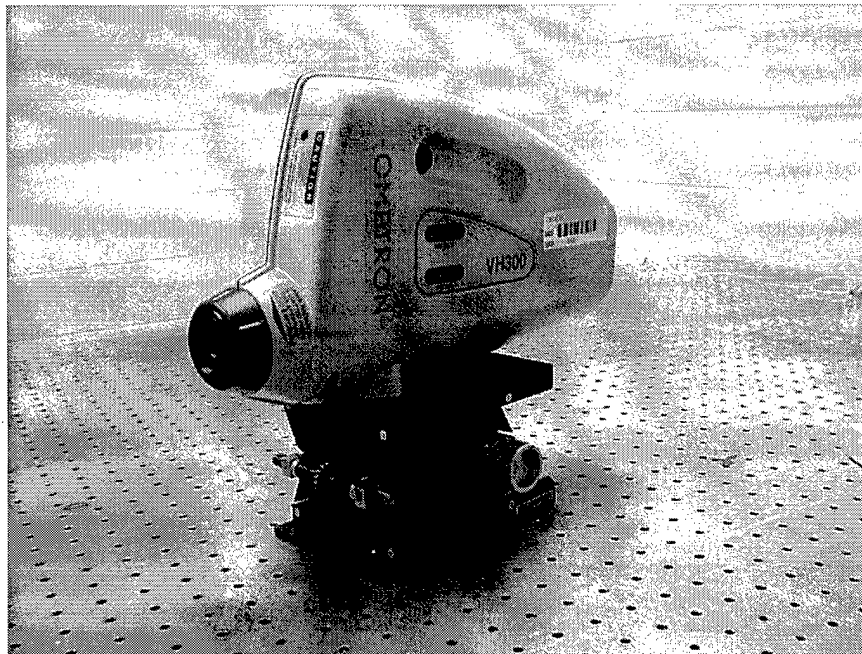


Figure 3.11 Ometron VH300 Laser Vibrometer

Ideally, the VH300 would be used as the response measurement system for all testing including entire fan modal testing and the forced response experiments (19). However, only one vibrometer was available for testing, hence accelerometers were the primary measurement transducer. The VH300 was a compact, lightweight, digital vibrometer which measured the response velocity of a test structure. With an effective velocity measurement range of  $\pm 300$  mm/s and a measurable frequency range up to 25000 Hz the VH300 capabilities, like the ENDEVCO® accelerometers, exceeded those needed for the modal testing (28). The VH300 had a maximum output voltage and sensitivity of  $\pm 20V$  and 33.3 mV/(mm/s) respectively (28). A test surface moving towards the VH300 generated

a positive analog velocity signal. Similar to the accelerometers, measurements were taken at room temperature, 65 to 75°F. The output signal was directly fed to the HP breakout boxes. The vibrometer was bolted upon a pedestal, which could be raised or lowered off the table to aid in aiming the laser head. To secure the entire structure, the pedestal was bolted to the pneumatic table.

**3.2.4.3 Force Transducer.** A PCB Piezotronic ICP® Model 208C01 Force Sensor was used to measure the harmonic forcing input. The force gauge had a sensitivity of 531.7 mV/lbf with a maximum suggested force load of 10 lbf. Since the anticipated force magnitude produced by the magnets were anticipated to be only a fraction of a pound, this sensitivity was adequate. A small magnet was fastened to the head of the gauge to produce similar repulsive effects experienced by the blades during forced response tests with the flywheel excitation system. Measurements were taken at room temperature, 65 to 75°F. Also, the sensor's output voltage was first amplified by the Kistler® Piezotron Coupler and sent onward to the HP breakout boxes before received by the SignalCalc 620 software.

### **3.3 Summary**

The preceding sections presented the basic experimental approach, test article and supporting test equipment. The two testing methods with their similarities and differences were defined. Further, explicit features of the bladed disk were discussed and the individual components comprising the flywheel excitation system were delineated. Also, the function of individual measurement sensors and their usage throughout the study were explained. The next chapter will step through the experimental procedure and discuss findings useful for the subsequent forced response analysis.

## *IV. Experimental Procedure*

### *4.1 Overview*

The experimental method can be separated in four major divisions.

First, the harmonic forcing input generated by the flywheel excitation system will be investigated and documented. Specifically, elements of periodicity and forcing magnitudes will be specifically identified.

Second, the modal parameters of a representative substructure (i.e blade) must be determined. Resolving which modes are identifiable and excitable will provide considerable guidance for the succeeding steps. Afterwards, all remaining substructures will be individually characterized.

Third, the system as a whole will be modal tested. The system is considered the test article and attached PZT Quickpacks. This free response structural characterization will identify modal groups and their distinguishing features.

Lastly, the forced response of the system will be measured to determine global and localized modes within the targeted modal bands. Various observations will be recorded to determine validity of the forcing method and characteristics of system mode localization and peak blade responses with past research findings. Along with other peripheral experimentation, these steps are summarized below.

1. Calibrate accelerometers used throughout experiment
2. Measure and characterize the forcing function of the flywheel magnets at various frequency and distance separations
3. Determine the physical properties of each blade
  - (a) Measure the geometry of the individual blades
  - (b) Measure the mass of the individual blades
4. Determine the set of modal properties for each blade

- (a) Determine the modal characteristics of a test blade
  - (b) Construct mode shapes of the test blade for the modal families of interest
  - (c) Measure the natural frequencies and damping of each blade
5. Modal test the entire disk assembly through MIMO reference sets
  6. Record the forced response behavior of the bladed disk for each modal family at various mistuning levels and engine orders
  7. Discuss and compare the forced vibrations results to draw significant conclusions

These chronological events outlay the experimental processes necessary to achieve this study's objectives. The first of these steps, transducer calibration, will help ensure succeeding free and forced vibrational experimental results are reliable and accurate.

## ***4.2 Accelerometer Calibration***

Over periods of extended use, accelerometer sensitivity is prone to drift from the initial manufacturer calibrated value. To ensure accuracy of response measurements, all ENDEVCO® accelerometer sensitivities were re-calibrated and recorded. The voltage outputs of the accelerometers were compared to that of a standard accelerometer, an ICP Piezoelectronics Model 301A10 with a sensitivity of 100 mV/g. HP generated excitation signals were amplified by an MB Dynamics Model SS530 Power Amplifier and then sent to a MB Dynamics Cal 50 Electromagnetic Vibration Shaker. The 301A10 standard accelerometer was fastened to the shaker. The ENDEVCO® accelerometers were mounted to an aluminum baseplate with model wax. This baseplate, in turn, was bolted to the top of the 301A10 transducer. Accelerometers were placed toward the baseplate center to prevent plate flexure modes from interfering with the calibration. Figure 4.1 shows the equipment setup.

The amplifier input level control knob was set to its middle setting. FRFs were constructed between the standard accelerometer and each ENDEVCO® accelerometer to ensure a level response in the frequency range of interest. Coherence plots were also analyzed to ensure the quality of data. Table 4.1 displays equipment settings for the

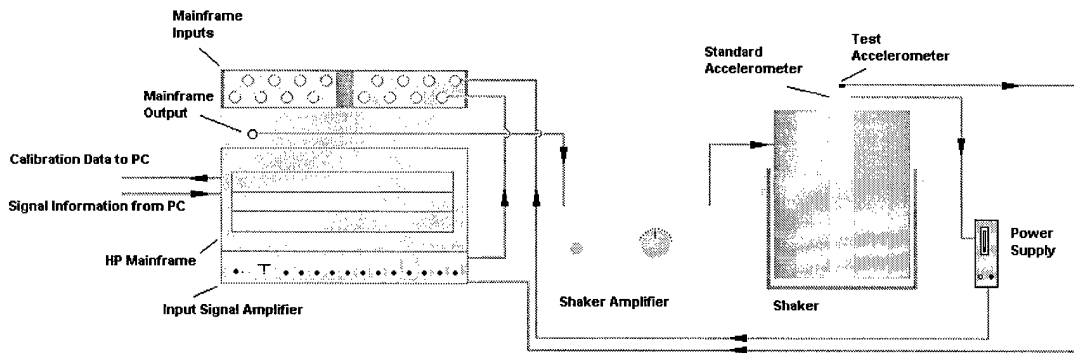


Figure 4.1 Calibration Equipment Setup (8)

calibration test. Table 4.2 shows the average sensitivity value of each accelerometer between 50 Hz and 1600 Hz. As indicated, each accelerometer was assigned to a specific blade throughout all experimentation.

Signal	Freq Bandwidth (Hz)	Input Range (V)	Accel Range (V)	Sampling Rate (Hz)	Averages	Data Points	Block Size
Random	1600	$\pm 3.0$	$\pm 0.1$	3200	10	1600	2048

Table 4.1 Accelerometer Calibration Equipment Settings

Blade #	Accelerometer	Sensitivity (mV/g)
1	CB96	9.94
2	CD47	10.44
3	CD27	10.04
4	CB77	10.17
5	CH75	10.10
6	CD05	10.32
7	CD36	10.15
8	CD10	10.41

Table 4.2 ENDEVCO® Accelerometer Sensitivities

### 4.3 Input Force Characterization

The essential properties between the magnet forcing function and periodic forcing witnessed by operational blisks can be appropriately simulated if the following criteria is met. First, the excitation system must be spatially periodic. Second, the input must be harmonic in nature. Lastly, for a detuned bladed disk, any engine order should excite

multiple system natural frequencies (11). Since the last requirement involves testing the bladed disk, it will be investigated later during the forced response experimental section.

Returning to Figure 3.5, it is apparent the flywheel drilled magnet slots are spatially periodic, spaced at equidistant angles around the outer flywheel rim. The magnets, positioned at fixed angles of rotations, are similar to the forward stators obstructing the upstream airflow to rotating compressor blades. Selecting twelve magnet slots allowed for different magnet arrangements, hence any factor of twelve is an engine order that can be simulated. Therefore, excitation inputs can mimic either the 2<sup>nd</sup>, 3<sup>rd</sup>, 4<sup>th</sup>, 6<sup>th</sup> or 12<sup>th</sup> engine order.

To fully describe the nature of the input function, the magnitude and subsequent frequency spectrum of the interacting magnets, hence each engine order, needed to be measured. The PCB Piezotronic ICP® Force Gauge would serve as the force measuring transducer. A small magnet was attached to the gauge head. The force gauge was mounted on a metal bracket at various distances from the flywheel magnets. To insure the flywheel experienced equal forcing around the magnet circle, another small magnet was mounted upon another metal bracket 180° across from the force gauge. The gauge and magnet pair were permanently bolted to the pneumatic table at a predetermined distance from the flywheel.

To begin an experiment run, the force gauge magnet and flywheel magnets were separated at a predetermined distance. The flywheel was spun up to achieve a set RPM speed. When the flywheel RPM of interest was reached, a snapshot of the force gauge time response data was recorded with the SignalCalc 620 software. With this time domain data, the force magnitude, period and power spectral densities (PSD) were plotted to visualize the essential forcing input characteristics. Table 4.3 displays equipment settings for all tests. The software trigger was set to free run (i.e. no signal input by the PC/HP). Flywheel RPM measurements were made with the HP Tachometer.

Signal	Time Span (s)	Force Gauge Range (V)	Sampling Rate (Hz)	Data Points
N/A	0.04	± 0.2	20000	800

Table 4.3 Force Input Characterization Equipment Settings

Several magnet distances and flywheel RPM combinations were recorded to characterize the excitation system. Plotted in Figure 4.2 is the time response of E.O. 12. The figures corresponding to 12 magnets in the flywheel, at three RPM levels with a magnet spacing of 0.2 in. Different RPM speeds were chosen to visualize the periodic features of the engine order.

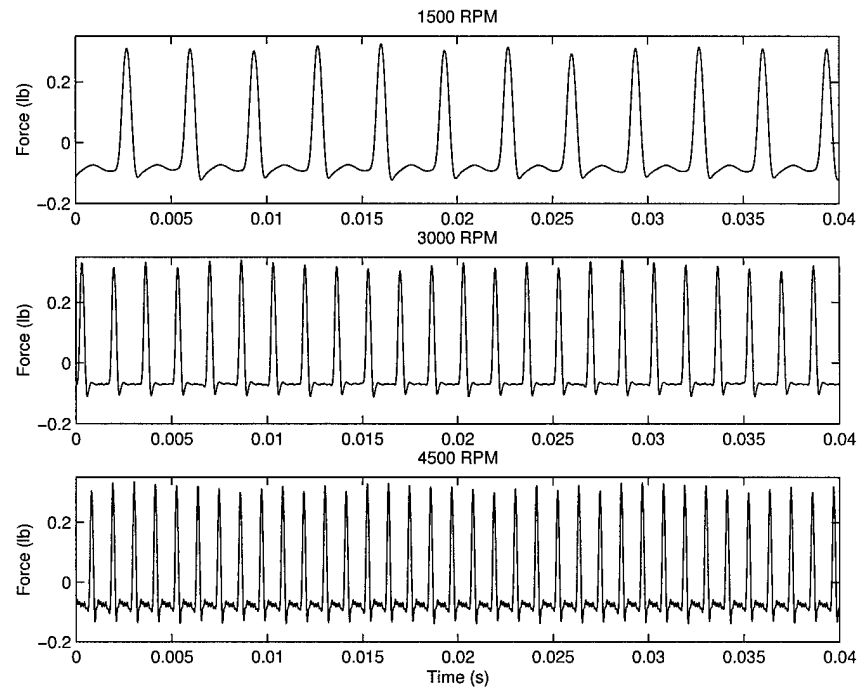


Figure 4.2 Time Response of E.O. 12 with 0.2 in Spacing

Figure 4.2 shows positive and negative forces, indicating repulsive and attractive forces respectively, are occurring during input forcing. Of interest is the attractive force between pulses possibly resulting from the flywheel and blade magnet edges, having similar polarity, interacting at the beginning and end of each blade passing. Further, Figure 4.2 shows the periodic nature of the forcing input by pulse time intervals proportionally decreasing as the RPM level rises. Not all pulses are of equal magnitude, although the pattern is repetitive. Apparently, many sinusoidal functions comprise the forcing input. At this magnet spacing, the largest peak force input for all flywheel RPMs is approximately 0.28 lbf.

The previously mentioned attractive force between each peak pulse consists of smaller pulses that increase in number with the flywheel RPM. This is explained through a waterfall plot of PSDs in Figure 4.3. Here, the periodic character of the force input is further revealed. Several distinct forcing frequencies are shown, all integer multiples of the lowest frequency. This is expected for any periodic function can be represented by a convergent series of harmonic functions whose frequencies are integral multiples of a certain fundamental frequency. As shown in Figure 4.3, the fundamental frequencies of E.O. 12 is 300 Hz, 600 Hz and 900 Hz for 1500 RPM, 3000 RPM, and 4500 RPM respectively. Again, as anticipated, the fundamental frequency and corresponding higher harmonics spread apart proportionally to RPM increases. Further, since the input force magnitude varies for each harmonic, every harmonic has a different degree of participation in the excitation.

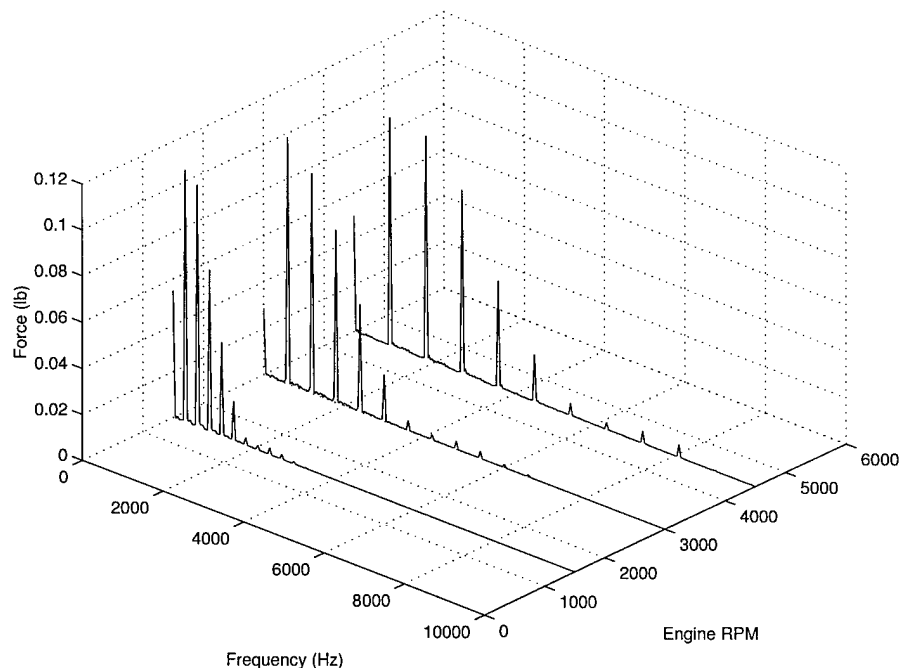


Figure 4.3 PSD of E.O. 12 with 0.2 in Spacing

To see the effects of distance on the force input, 0.4 in and 0.6 in magnet spacing test runs were also recorded for E.O. 12. Since these figures contain similar characteristics as the 0.2 in data, they have been included in Appendix A. However a few differences regarding magnet spacing should be noted. First, attractive and repulsive forces have decreased with

increased magnet spacing. The PSD figures provide the explanation, showing a quicker convergence of higher harmonics for each fundamental frequency. Hence, the frequency spectrum bandwidth diminishes.

Considering these previous discussions, the 0.4 in magnet spacing will be used for the bladed disk forced response testing. This separation provided a suitable combination of force magnitude and harmonic components without risk of exceeding the forcing vibration limits of the ENDEVCO® accelerometers. Several other E.O./RPM combinations were plotted at this spacing to compare behavior with E.O. 12. Refer to Figures A.5, A.6, A.7, A.8, A.9 and A.10 in Appendix A to observe these RPM and PSD plots.

Similarities and differences between the various engine orders are summarized in a few general statements. First, as the engine order decreases for a given flywheel RPM, the number of higher harmonic frequencies increases. Thus, input forcing is spread across a broader frequency spectrum. As a result, the periodic forcing function contains more sinusoidal components and characterizing the force becomes increasingly complex. Second, with the transmitted energy spread over many more frequency multiples, peak amplitudes of each harmonic diminish with the decreasing engine order.

Figure 4.4 further illustrate these engine order distinctions. Although the forcing frequency is constant at 300 Hz, pulse duration decreases as engine order decreases. However, the magnitude of the pulses increases with the same decreasing magnet number. Additionally, due to increased number of sinusoidal components at lower engine orders, the attractive forces between pulses is more jagged. These observations indicate, during forced response tests, more energy could be transmitted to the bladed disk at higher engine orders. To mathematically verify this hypothesis, a simplified convolution analysis modeling the periodic input and the bladed disk response as an impulse function and impulse response function, respectively, should be investigated for future research.

During the forcing function analysis, the flywheel motor could not sustain steady state speeds above 6000 RPM. The high motor shaft speeds caused overheating and raised concerns of potential motor damage. The previous time and frequency domain plots were brief snapshots of the force transducer response, therefore the peak flywheel speeds needed

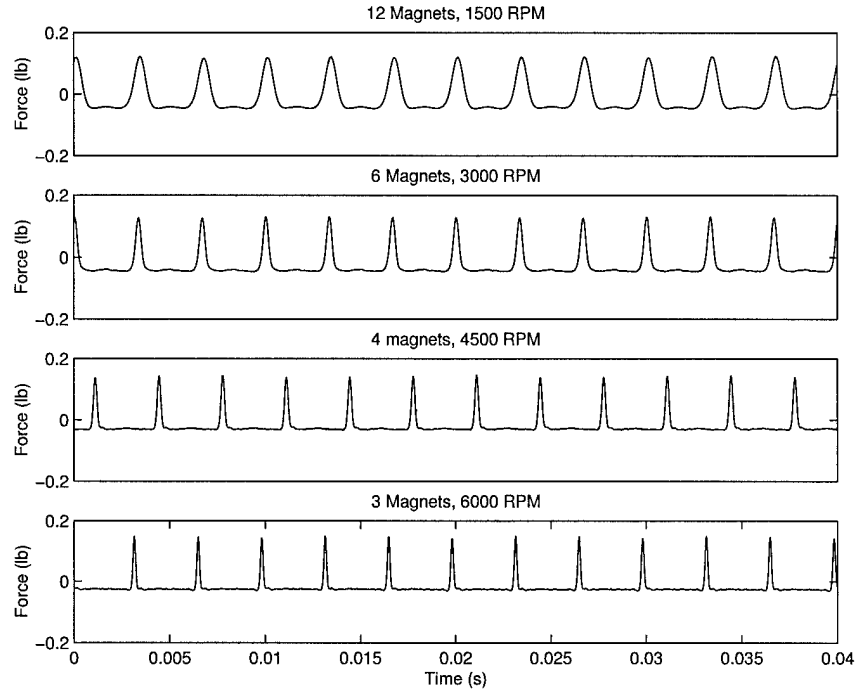


Figure 4.4 Time Response of Various Engine Orders, 300 Hz, 0.4 in Spacing

for each run were held less than 10 seconds. Specifically for lower engine orders, the forced response analyses would require high flywheel RPM speeds maintained for several minutes. As a result, to alleviate the possibility of motor failure, the flywheel would not be commanded to rotational speeds in excess of 6000 RPM for the forced vibrations analysis of the experiment.

During spin-up of the flywheel, several resonant frequencies of the flywheel/cantilever table system were excited. Apparently, the flywheel was not perfectly symmetric and behaved as a unbalanced rotating mass. Through the operating range of the spinning flywheel, resonant frequencies for the flywheel/table pair occurred at roughly 2100 RPM (35 Hz) and 4200 RPM (70 Hz). These intense vibrations would interfere with the alignment of the flywheel and blisk magnets, thereby corrupting the forced response experimentation. Two steps were taken to resolve the problem. First, the flywheel was rotationally balanced by shaving a small section around one third of the rim. Second, to counteract possible energy transmission and reflection across the cantilever table and the concrete wall, a vibration absorption pad was cushioned between the table and wall. With these remedies

in place, the resonant responses were effectively eliminated and the flywheel could be operated throughout the entire RPM envelope without disruption.

**4.3.1 Pulse Phasing and Blade Order.** As discussed in Chapter 2, the combination of eight blades and five flywheel magnet configurations, both with equal rotational spacing, yielded unique force phasing for each engine order. These phase differences may be significant for the forced response experiment. Should the number of disk blades or engine order alter, the phasing would also change. Like the numerical analysis, similar considerations of these phase differences on the forced response characteristics will be made later in the experiment. Table 4.4 cites this information while Figures 4.5, 4.6, 4.7 and 4.8 visually highlight the blades involved in each pulse for a given engine order.

Magnets	Pulses/Rev	Phase Angle
2	8	45°
3	24	15°
4	8	45°
6	24	15°
12	24	15°

Table 4.4 Input Force Phasing at Various Magnet Configurations

For each pulse, dark blades indicate excited blades while light blades are transient. Of note, the 12 and 4 magnet configurations are identical in blades involved for each pulse. These similarities of engine order phasing were also mentioned in the numerical forced response portion of Chapter 2. However, the differing phase angle between pulses is indicated in Table 4.4.

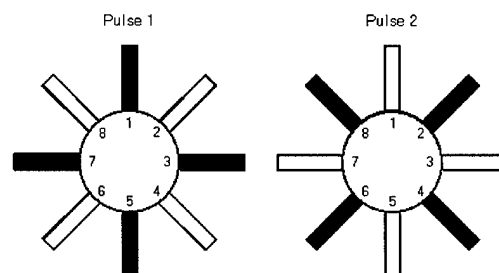


Figure 4.5 Pulse Phasing for Engine Order 4 and 12

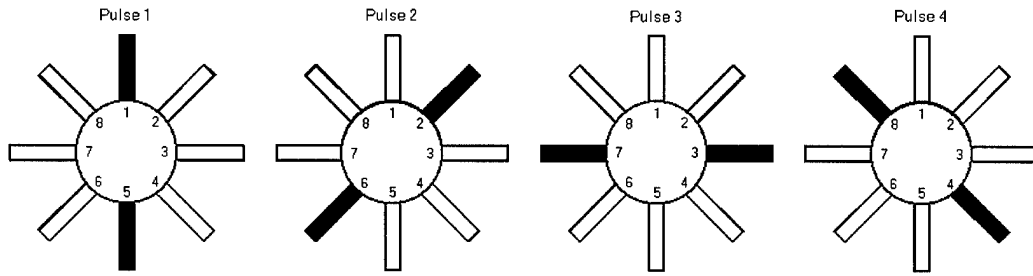


Figure 4.6 Pulse Phasing for Engine Order 6

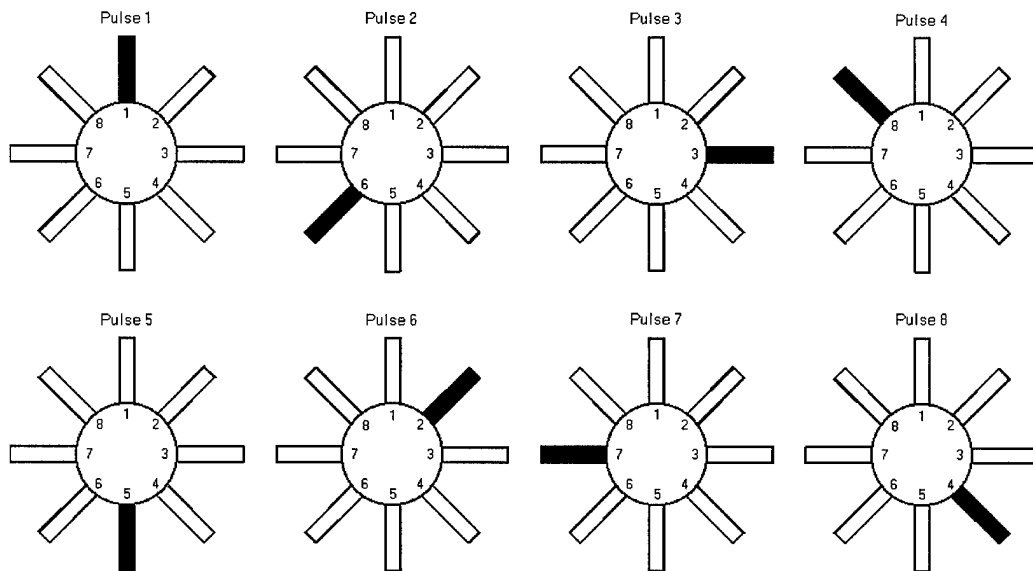


Figure 4.7 Pulse Phasing for Engine Order 3

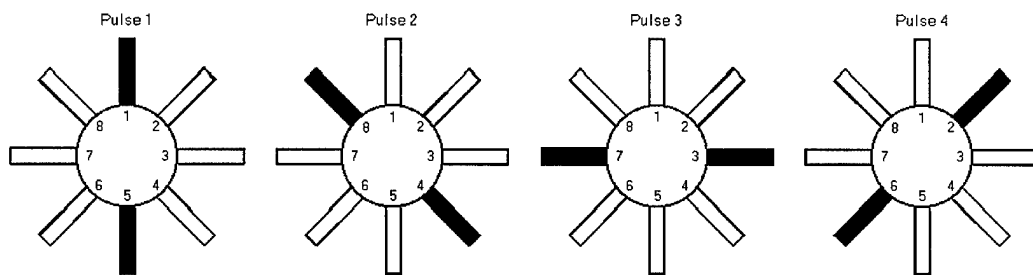


Figure 4.8 Pulse Phasing for Engine Order 2

#### 4.4 Blade Characterization

Before modal properties of the entire bladed disk can be gathered, each individual substructure (i.e. blade) physical properties and modal characteristics must be identified.

This will not only reveal how well tuned is the bare system, but the data can be used to identify which specific modal families to concentrate the remaining experiments. Further, to visualize these modes, contour plots depicting the mode shapes will be constructed to understand deflections and strain energy distribution throughout the blades.

**4.4.1 Dimensions and Mass.** Each blade length, width and thickness geometry was measured with a Fowler Precision Dial Caliper (model MH 18600). Multiple measurements were taken and averaged for increased accuracy. The mass of each blade was computed by multiplying the blade volume by the density of aluminum, 0.0975 lb/in<sup>3</sup>. This information is displayed in Table 4.5 along with mean and standard deviation values.

Blade masses do not include the bonded PZT Quickpacks. Dimensional measurements were taken with the blades soldered to the disk and were particularly challenging. It should be recognized that the blade length was measured along the centerline, from the blade tip to the hub. However, the length is not constant across the root since each blade was attached along a curved hub surface. The outside edge distance is 0.1 in longer than that recorded in Table 4.5. It should be noted that this difference in measured to actual length would introduce error if the natural frequencies were cross referenced to plate theory.

Blade #	Length (in)	Width (in)	Thickness (in)	Mass (g)
1	2.999	2.400	0.0640	20.372
2	3.001	2.400	0.0640	20.386
3	3.000	2.400	0.0641	20.411
4	2.999	2.400	0.0641	20.404
5	3.000	2.399	0.0640	20.371
6	3.002	2.399	0.0639	20.352
7	3.000	2.399	0.0640	20.294
8	3.000	2.400	0.0640	20.379
Mean	3.0001	2.3996	0.0640	20.3711
Std. Dev (%)	0.0330	0.0216	0.100	0.179

Table 4.5 Individual Blade Physical Properties

The STD for all these values is well below 1%. As the STD approaches zero, the more probable the system will resemble a tuned test article. Despite this, small mistuning levels such as these can have significant effects on mode localization of weakly coupled systems (41).

**4.4.2 Blade Natural Frequencies and Mode Shapes.** Preliminary experimental tests are necessary to pinpoint the general location of blade natural frequencies. Because of their structural characteristics, each disk blade can be modeled as a cantilever flat plate with fixed-free-free-free boundary conditions. Therefore, each blisk modal family can be associated to the modal shapes of this particular constrained cantilever plate. Each modal family possess a unique number of nodal circles and diameters. By plotting these mode shapes, we can graphically understand what nodal patterns subject the blades to more severe stress and strain energy distributions (3). In addition, which modal families and engine order combinations are testable under the maximum rotating flywheel speed constraint must be determined.

**4.4.2.1 Blade Three Modal Frequency Identification.** Blade three was selected to obtain the generic modal patterns and frequencies. Facing the flywheel, this blade was situated between the 10 and 11 o'clock position. It was chosen among the blades for its unobstructed view from the VH300 Vibrometer. The modal fan structure was grounded to the test table through a bolted axial rod. The small magnet and accelerometer were adhered to the blade, previously shown in Figure 3.8, to authentically replicate the blade during the upcoming forced response tests. The blade was excited with the epoxied PZT QP10Ni strain actuators, driven by an ACX EL 1224 Amplifier. PZT actuators on the remaining blades were configured with open electrical boundary conditions. The Ometron VH300 Laser Vibrometer was the measurement sensor used to collect the modal test data. The laser head was positioned approximately 48.2 inches from the blade to promote optimal working distance (28). Since each blade was angled at the axis of rotation, the laser line of sight was approximately  $45^\circ$  off each blade's normal. This canted blade angle slightly affected the 48.2 inch distance from point to point, although variance was within  $\pm 0.5$  inches. Due to limited space on the vibration isolated table, an elevated mirror redirected the laser beam  $90^\circ$  towards the blade. The laser vibrometer setup is shown in Figure 4.9.

The remaining seven blades were artificially localized, whereby their natural frequencies would not interfere with the test blade. Tip masses of 20 grams where added for this 'detuning'. The modal test was conducted while the blade three PZT actuator was driven

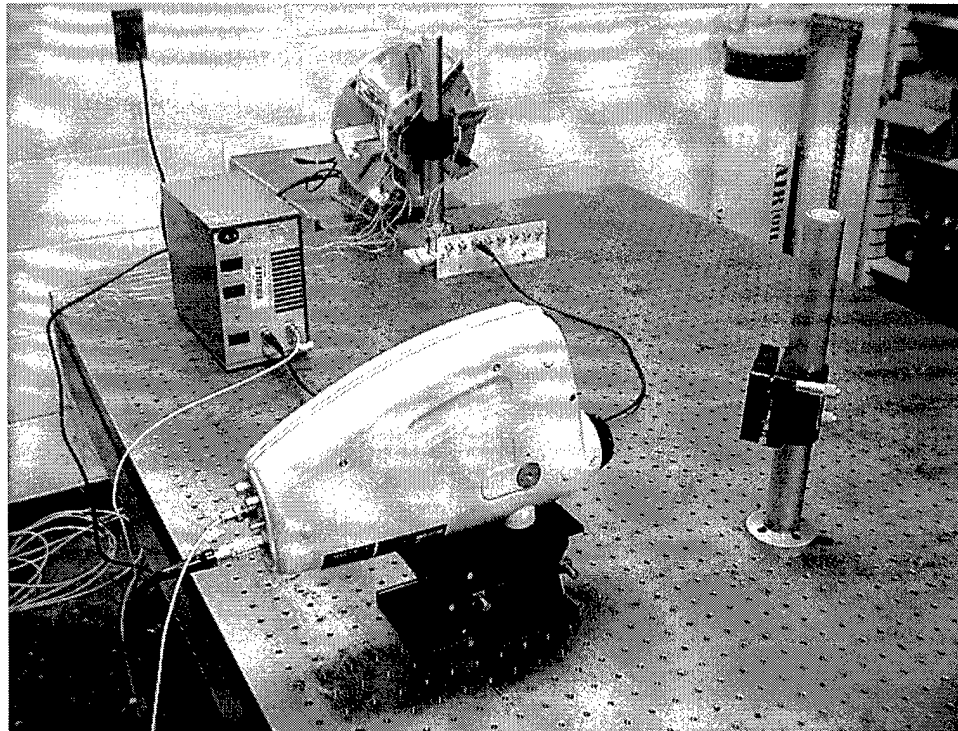


Figure 4.9 Mode Shape Construction Experimental Setup

with a random input signal. The laser was manually steered on the blade to collect 16 separate data points, shown in Figure 4.10, each point analyzed with a separate run. Data point positions are displayed in Table 4.7. To increase optical signal feedback, reflective tape was placed over each collection point. Due to the limitations with the motor speed, the frequency span was selected at 1562.5 Hz, well beyond the maximum measurable forcing frequency of 1200 Hz with E.O. 12. A complete reference of equipment settings are shown in Table 4.6.

Signal	Freq Bandwidth (Hz)	PZT Range (V)	Vibrometer Range (V)	Sampling Rate (Hz)	Averages	Data Points	Block Size
Random	1562.5	$\pm 10.0$	$\pm 2.3529$	4000	10	3200	8192

Table 4.6 Blade Modal Characterization Equipment Settings

An Eigensystem Realization Algorithm (ERA) was used to perform the modal parameter identification (21). The routine utilized throughout the experiments was a MATLAB® based ERA analysis program written by Dr. Joseph Hollkamp of the Air Force Research Laboratory (AFRL) (17). The algorithm is based upon the construction of a data matrix, called the generalized block-Hankel matrix, from free response time data. The user selects

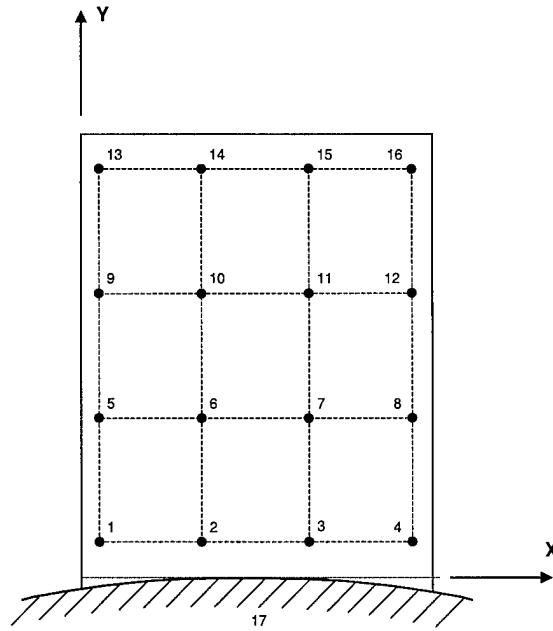


Figure 4.10 Blade Three Mode Shape Measurement Points

	Pt 1	Pt 2	Pt 3	Pt 4	Pt 5	Pt 6	Pt 7	Pt 8
X (in)	0.125	0.8333	1.5417	2.25	0.125	0.8333	1.5417	2.25
Y (in)	0.375	0.375	0.375	0.375	1.167	1.167	1.167	1.167
	Pt 9	Pt 10	Pt 11	Pt 12	Pt 13	Pt 14	Pt 15	Pt 16
X (in)	0.125	0.8333	1.5417	2.25	0.125	0.8333	1.5417	2.25
Y (in)	1.958	1.958	1.958	1.958	2.75	2.75	2.75	2.75

Table 4.7 Blade Three Measurement Point Locations

the size of the Hankel matrix, guided by the following criteria. Two columns are needed for each expected system mode. For noisy data, this column number is typically increased to ten. Further, the number of rows is at least 2-3 times the total number of columns. Again, for particularly noisy data, the row multiplication factor can be increased (4). Having selected the Hankel matrix size, a singular value decomposition is performed. The Hankel matrix is decomposed and time shifted for each Hankel column to form a minimum order realization. The user selects a truncated number of singular values to retain, each value representing either a system or noise mode. Half the number of singular values represents the number of modes that will be identified by the algorithm (19). In practice, it is difficult to cleanly separate system and noise mode. As a result, several retained singular values

must be tried to deliver an accurate modal estimation. Unfortunately, by observation, it is difficult to distinguish between the two types of modes. Therefore, an accuracy indicator called the Eigensystem Modal Assurance Criterion (EMAC) is used to distinguish authentic modes from the noise. Values can range anywhere from 0 to 100. EMACs greater than 90 are typically considered system modes, while remaining modes are discarded as noise. The eigenvectors and eigenvalues associated with each singular value of the acceptable EMAC level are the system modal properties. Each eigenvector represents a system mode shape. The real portion of an eigenvalue is the natural frequencies while the imaginary portion is the damping ratio (21).

Before an ERA analysis can be conducted, the FRFs of the sixteen collection points must be converted to impulse response data. An inverse Fourier transform was performed on each FRF via inverse fast Fourier transforms before insertion into the algorithm (20). The sixteen individual time histories were synchronized and treated as a pseudo single input multiple output (SIMO) as if all sixteen points were recorded simultaneously.

Analysis on a fixed-free-free-free boundary condition plate with the dimensions and material properties of blade three foretold of three anticipated cantilever modes within the test frequency bandwidth (26):

- First Bending Mode
- First Torsion Mode
- Second Bending Mode

Although only the first two modes were testable because of maximum flywheel rotational speed restrictions, it required no more computational effort to modal identify the second cantilever bending modal family with the given equipment settings. As a result, this second bending mode will be presented in addition to the first bending and torsion, whereby providing a broader characterization of the system.

To accommodate these three modal groups, unforeseen hub modes, table modes and exceptionally noisy data, a Hankel matrix of 500x100 was selected. A singular value of 16 yielded results that gave consistent frequencies and damping values while generating

high EMACs. The ERA identified natural frequencies and damping ratios are shown in Table 4.8. Corresponding mode shapes are shown in Table 4.9, normalized by the first component.

Mode	Frequency	Damping Ratio (%)	EMAC
1	210.7	0.4546	99.95
2	381.5	1.783	60.71
3	553.4	0.2227	99.71
4	1039.9	1.001	85.90
5	1246.7	3.806	0.005
6	1297.6	0.5439	99.41

Table 4.8 Blade Three Natural Frequencies and Damping Ratios

Mode 1	Mode 2	Mode 3	Mode 4	Mode 5	Mode 6
0.152	0.3551	0.0406	0.2125	0.1183	0.0877
0.0187+0.0003i	0.3119+0.0007i	0.0097+0.0002i	0.2074-0.00601i	0.1121+0.0446i	0.0788+0.0004i
0.0173+0.0001i	0.2747+0.0008i	-0.0200+0.0001i	0.2123-0.0109i	0.1103+0.0662i	0.0794+0.0002i
0.0154-0.0003i	0.2382-0.0006i	-0.0557+0.0005i	0.2352-0.0134i	0.15940.0815i	0.10803-0.0000i
0.1117+0.0057i	0.3769-0.0024i	0.2110+0.0008i	0.3111+0.0081i	0.0718+0.0578i	0.3431-0.0006i
0.1173+0.0047i	0.3119-0.0049i	0.0675+0.0003i	0.2797+0.0007i	0.0718+0.0578i	0.3431-0.0006i
0.1139+0.0045i	0.2520-0.0074i	-0.0881+0.0010i	0.2991-0.0022i	0.2213+0.1158i	0.3003+0.0003i
0.1032+0.0036i	0.2110-0.0107i	-0.2282+0.0019i	0.3571-0.0048i	0.2213+0.1158i	0.3003+0.0003i
0.2504+0.01171i	0.3356-0.0191i	0.3809-0.0003i	0.1358+0.0037i	0.3823+0.2461i	0.3686+0.0015i
0.2532+0.0084i	0.2476-0.0246i	0.1031+0.0016i	0.1034+0.0000i	0.1870-0.0104i	0.1769+0.0013i
0.2553+0.0141i	0.1809-0.0280i	-0.1462+0.0017i	0.1241+0.0034i	0.2592+0.531i	0.1907+0.0015i
0.2411+0.0102i	0.1274-0.0352i	-0.4124+0.0030i	0.2001+0.0125i	0.4403+0.1168i	0.2926+0.0006i
0.4301+0.0224i	0.1921-0.0187i	0.4209+0.0020i	-0.3334-0.0131i	-0.3160+0.0199i	-0.3270+0.0042i
0.4096+0.0222i	0.1487-0.0329i	0.1601+0.0016i	-0.2983-0.0083i	-0.2274-0.383i	-0.2971+0.0029i
0.4147+0.0219i	0.0693-0.0412i	-0.1946+0.0026i	-0.2811+0.0059i	-0.2804-0.0506i	-0.2923+0.0000i
0.4142+0.0237i	0.0037-0.0642i	-5459+0.0040i	-0.2329+0.0236i	-0.1434-0.0385i	-0.2206-0.0027i

Table 4.9 Blade Three Mode Shapes

There are three modes with EMACs above 90, very close to 100. These particular modes also possess extremely low modal damping ratios, as anticipated with a lightly damped structure. With a high degree of confidence, these were identified blade modes. However, the fourth mode at 1039.9 Hz has a high enough EMAC value that it should not be prematurely disregarded as unwanted noise. Further modal testing needed to be conducted to determine its origin.

Initial analysis of the FRFs showed a stronger response for Mode 4 at the blade/hub interface, data points 1 through 4. This insight led to the addition of a seventeen data point, 0.5 inches below the blade root as shown in Figure 4.10. This data point would

verify if the mode was indeed from the hub. Using the same equipment settings as shown in Table 4.6, a transfer function plot of the hub response to PZT Quickpack input was generated and is shown in Figure 4.11.

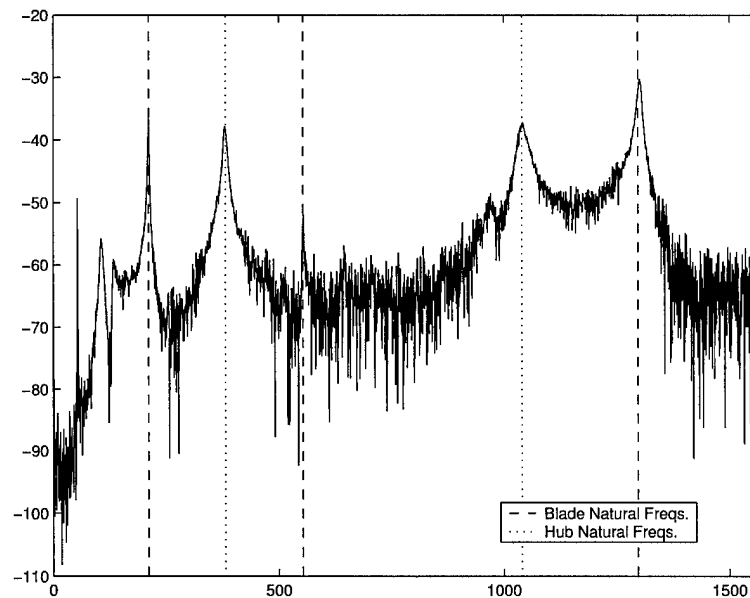


Figure 4.11 Hub Frequency Response Function - Point 17

As expected, the response magnitude is quite small across the bandpass indicating high hub stiffness and rigidity as compared to the blades. It is apparent from the sharp peaks shown in Figure 4.11 both Mode 2 and Mode 4 originate from the hub structure. Fortunately, neither hub mode's presence should interfere with blade modal parameter identification since both are positioned at frequencies far removed from the blade modes.

**4.4.2.2 Display of Mode Shapes.** A graphic display of the normalized mode shape data provides visual insight into the manner which the structure is vibrating. Upon examination, the mode components have phase angles roughly  $0^\circ$  or  $180^\circ$  from neighboring elements. Therefore, imaginary portions of the mode shapes vectors have been dropped due to their minimal size relative to the real portions. Static plots are adequate to depict the essential features of the three modes and are illustrated in Figures 4.12 through 4.14. A basic, dotted grid of the undeformed test region is shown in each figure.

Stars on the deformed mode shape depict the actual sixteen data collection points. A spline interpolation was performed between these points for visual aesthetics.

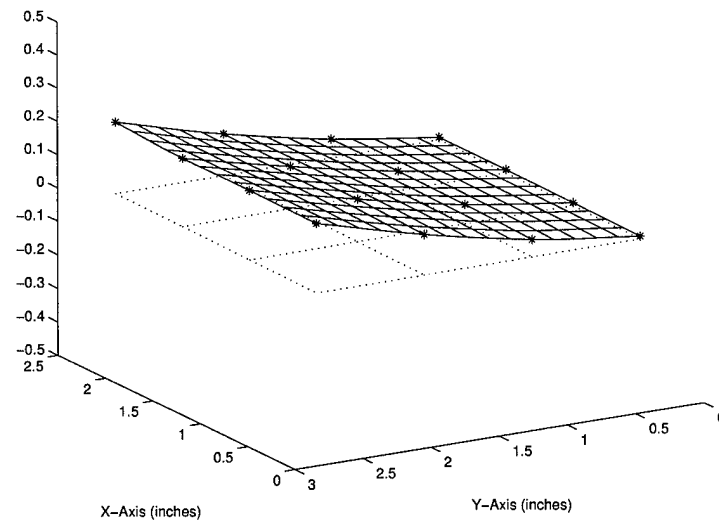


Figure 4.12 Blade Three Mode Shape - 1<sup>st</sup> Bending Mode (210.7 Hz)

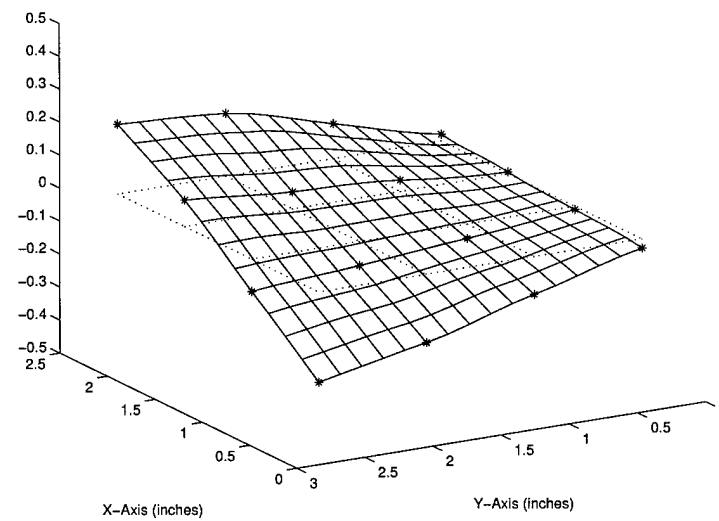


Figure 4.13 Blade Three Mode Shape - 1<sup>st</sup> Torsion Mode (553.4 Hz)

All modes appear as expected, with the appropriate number of nodal diameters and nodal circles for each respective mode. A slightly larger 'hump' is found on one

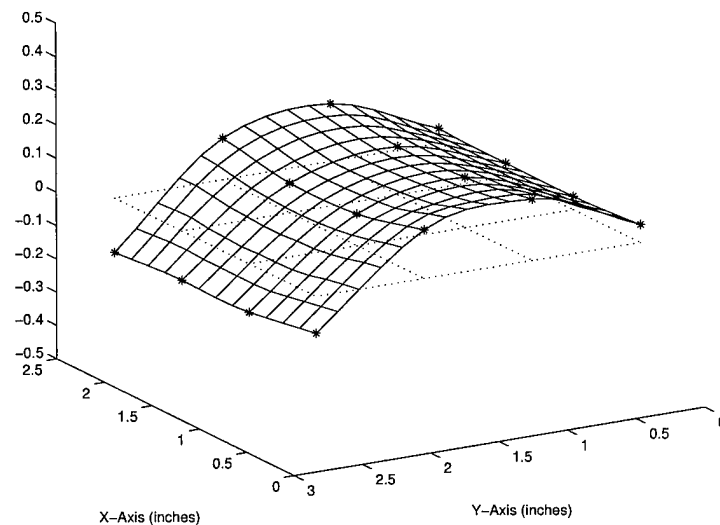


Figure 4.14 Blade Three Mode Shape - 2<sup>nd</sup> Bending Mode (1297.6 Hz)

outside blade edge in the second bending mode. This can be attributed to inaccuracies in exact position of the vibrometer laser and irregular mass distribution resulting from the added lump mass of the accelerometer and small magnet. Similar natural frequencies and damping values for the remaining blades are anticipated.

#### 4.4.3 *Blades' Natural Frequencies and Damping - Two Cases.*

Although the blades of the test article are intended to be identical, random deviations in the structure are an unavoidable reality. Hence, the individual natural frequencies and damping ratios of each original blade need be evaluated to determine the level of initial mistuning. For comparison and to provide additional data, it was desired to test the bladed disk in a more, nearly-tuned configuration. Due to the improbability of tuning both the first cantilever bending and torsion modes simultaneously, the first bending mode was selected as the candidate to be modified toward a closely tuned modal group. More mistuning sets were desirable, however time limitations of the study restricted any additional cases.

Experiments to modal test the remaining blades were performed. Eight test runs were conducted, one for each blade, and repeated on blade three to compare these results with those collected from the mode shape analysis. Similar to the previous section, each

individual blade's PZT Quickpack was driven separately with an ACX EL 1224 Amplifier while the surrounding blades were 'detuned' with 20 grams of fishing weights. The ENDEVCO® accelerometers were used as the response transducers instead of the laser vibrometer. Each accelerometer was positioned at the thirteenth data point of its respective blade, as previously shown in Figure 4.10. The small magnets were also in place during the testing. For a given test run, all 'detuned' blades' respective PZT bundles were electrically open for consistent boundary conditions. Equipment settings for the test runs are listed in Table 4.10.

Signal	Freq Bandwidth (Hz)	PZT Range (V)	Accel Range (V)	Sampling Rate (Hz)	Averages	Data Points	Block Size
Random	1562.5	$\pm 10.0$	$\pm 0.5$	4000	10	3200	8192

Table 4.10 Individual Blade Modal Properties Equipment Settings

To tune the model fan for Case II, small fishing weights of approximately 1.087 grams apiece were added to all blades excluding blade five. To not disrupt the torsion mode, the small masses were epoxied at the centerline of the blade tip. Based on the calculated blade masses shown in Table 4.5, the intent was to lower the natural frequencies into the proximity of blade five. Generally, the extra weight dropped the natural frequencies below 200 Hz for each modified blade. Through iterative modal measurements, the fishing weights were filed until enough mass remained to bring each blade's fundamental frequency within 1% of blade five.

An ERA analysis was performed on the test data. Several Hankel matrix sizes were constructed for each blade's test data before one was found that yielded consistency in the estimated natural frequency values and damping ratios. Since the accelerometers were situated on each blade tip, the hub modes discovered during the modal shape analysis should not be detected. Only the three blade modes were anticipated in the results. Hankel matrix size and singular value cutoffs are shown for each blade in Table 4.12.

Due to a slightly noisier data sample, a larger Hankel matrix was required for blade seven, Case I. Singular value cutoffs varied significantly within each data set. This was an unexpected result, however each cutoff number was still larger than the anticipated number of blade modes. For both cases, the natural frequencies of each blade for the three modes are listed in Tables 4.12 through 4.14.

Blade #	Case I		Case II	
	Hankel Matrix	SV Cutoff	Hankel Matrix	SV Cutoff
1	250x50	25	250x50	17
2	250x50	11	250x50	22
3	250x50	22	250x50	19
4	250x50	21	250x50	19
5	350x70	12	250x50	17
6	250x50	21	250x50	23
7	250x50	22	250x50	16
8	250x50	16	250x50	21

Table 4.11 Hankel Matrix Dimensions & Singular Values for Blade Modal Analysis

Blade #	Case I			Case II		
	Freq. (Hz)	Zeta (%)	EMAC	Freq. (Hz)	Zeta (%)	EMAC
1	208.7	0.5465	99.20	203.6	0.5066	99.65
2	208.2	0.6332	99.73	203.8	0.4043	99.78
3	210.7	0.4546	99.95	203.3	0.5628	99.30
4	212.4	0.5733	99.51	204.0	0.5551	99.85
5	204.0	0.5948	99.57	204.1	0.5573	99.48
6	209.5	0.5052	99.68	203.2	0.4270	99.83
7	211.6	0.3394	99.88	203.8	0.3491	99.68
8	208.9	0.4157	99.92	203.9	0.3104	99.69
Mean	209.22	0.5078	99.68	203.71	0.4591	99.66
Std. Dev. (%)	1.24	19.52	0.25	0.16	21.80	0.19

Table 4.12 Blade Natural Frequencies and Damping Ratios - 1<sup>st</sup> Bending Mode

As shown from the spread of blade frequencies in Case I, there is a slight inherent amount of mistuning preexisting within the model fan. The blade frequency distribution standard deviation varies for all families in the range of 1%. However, Case II shows that with intentionally added tip masses the first bending frequencies have a much smaller frequency distribution, over an 80% STD reduction compared to Case I. As intended, the tip masses had only a slight effect on the higher modal groups. In contrast, there is significant variance in the damping ratios for both cases, throughout all three frequency groupings. The worst damping disparity is nearly 40% STD among the second bending mode frequencies. The 'tuning' weights appeared to have little overall effect on this modal property. There also does not appear to be a specific correlation of damping ratio alteration with blade to blade mistuning. This demonstrates the sensitivity of damping to mistuning

Blade #	Case I			Case II		
	Freq. (Hz)	Zeta (%)	EMAC	Freq. (Hz)	Zeta (%)	EMAC
1	553.9	0.2988	99.29	554.2	0.2121	99.66
2	555.6	0.2247	99.24	558.1	0.1973	99.68
3	553.4	0.2227	99.71	553.7	0.2124	99.85
4	558.7	0.2605	99.05	558.6	0.2119	99.64
5	553.6	0.2991	99.13	554.2	0.2121	99.66
6	558.2	0.2122	99.72	558.1	0.1973	99.67
7	553.9	0.1711	99.85	558.9	0.1941	99.91
8	554.6	0.1948	99.58	554.5	0.2170	99.69
Mean	555.24	0.2355	99.45	556.29	0.2068	99.72
Std. Dev. (%)	0.38	19.87	0.31	0.42	4.30	1.00

Table 4.13 Blade Natural Frequencies and Damping Ratios - 1<sup>st</sup> Torsion Mode

Blade #	Case I			Case II		
	Freq. (Hz)	Zeta (%)	EMAC	Freq. (Hz)	Zeta (%)	EMAC
1	1285.1	0.9433	96.45	1240.9	0.7473	97.73
2	1284.1	0.7473	98.32	1251.5	0.6197	97.00
3	1297.6	0.5439	99.41	1245.2	0.3773	99.55
4	1306.9	0.5802	99.40	1242.9	0.5236	99.79
5	1266.9	0.4528	93.82	1267.5	0.4340	97.13
6	1292.2	0.4051	95.07	1239.7	0.4179	98.14
7	1305.9	0.3556	98.46	1259.3	0.3366	97.83
8	1296.4	0.3392	99.95	1261.0	0.2812	99.59
Mean	1292.3	0.5459	97.61	1251.0	0.4672	98.35
Std. Dev. (%)	1.00	38.38	2.30	0.84	33.18	1.16

Table 4.14 Blade Natural Frequencies and Damping Ratios - 2<sup>nd</sup> Bending Mode

variations. Further, it was difficult to obtain consistent damping values among the blades. This prompts a suspicion that damping deviation is a byproduct of the ERA analysis (8). In any event, the high EMACs bring confidences to the accuracy of the identified frequencies. These two mistuning cases should provide a variety of data results and broad areas of analysis during forced response of each modal family.

The reader should note that a spinning operational engine fan would have blade elastic properties change due to centrifugal stiffening. As a result, blade natural frequencies would be somewhat higher than that of a stationary bladed disk (10).

## 4.5 Modal Testing of the Bladed Disk

The free response characteristics of the complete bladed disk are also needed for inclusion with the forced vibration analysis. Therefore, complete bladed disk modal tests were conducted before the forced response data was gathered. Including the second bending mode in the modal parameter identification process would complicate these tests without added benefit for the forced response analysis. Therefore, for the remainder of the study, only the first bending and first torsion modes will be investigated.

Due to the narrowly spaced blade natural frequencies and light inter-blade coupling of the structure, the modal tests were particularly challenging. As demonstrated in Chapter 2, eight global mode shapes exist in each family, although the modal bandwidth and exact frequency location of the modes are unknown. Furthermore, several excitation inputs were required to correctly identify the eight closely spaced modes. Several approaches to excite the whole structure were attempted with varying success. Hammer impacts to the individual blade tips did not energize the blisk sufficiently for proper modal analysis. The MB Dynamics Cal 50 Electromagnetic Shaker proved a better input force than the hammer, although the coherence plots dropped dramatically from unity after 250 Hz. There simply was not enough cross blade response for adequate analysis of the first torsion mode.

Ultimately, the PZT Quickpacks used for the individual blades were again utilized as the input devices. Rather than excite the testpiece throughout a broad frequency range, the tests were conducted via chirp free decay excitation. This technique has been performed by previous modal testers with great success (8)(19). Each PZT actuator was driven separately about a modal family natural frequency while data from the eight ENDEVCO® accelerometers was collected by the HP/PC. The bandwidth of each chirp signal sweep throughout both cases is shown in Table 4.15. The equipment settings are listed in Table 4.16.

Case I		Case II	
1 <sup>st</sup> Bending	1 <sup>st</sup> Torsion	1 <sup>st</sup> Bending	1 <sup>st</sup> Torsion
195Hz - 220Hz	545Hz - 560Hz	195Hz - 210Hz	545Hz - 560Hz

Table 4.15 Chirp Signal Sweeps for Bladed Disk Modal Tests

Signal	Freq Bandwidth (Hz)	PZT Range (V)	Accel Range (V)	Sampling Rate (Hz)	Averages	Data Points	Block Size
Random	1600	$\pm 10.0$	$\pm 0.5$	4096	1	1600	4096

Table 4.16 Bladed Disk Modal Test Equipment Settings

The chirp provided a method to precisely control the frequency range of interest and not excite modes outside this bandwidth. Also, the resolution of the data could be increased by focusing on a narrower frequency pass. This would help facilitate the identification process of the tightly spaced modes. The amplifiers were connected to each PZT sensor. The random excitation input source was circulated throughout all eight actuators, giving eight different excitation locations. Unstimulated PZTs had their respective amplifier inputs shorted for consistent electrical boundary conditions. Unfortunately, due to unforeseen difficulties in acquiring equipment, only six ACX Amplifiers were available for the test. Two Piezoelectric System Incorporated (PSI) Amplifiers, maximum 150 V rating, were substituted for the missing ACX amplifiers. Input voltages to the amplifiers were altered to ensure consistent driving voltages for all PZT Quickpacks. Table 4.17 shows the amplifier to blade connections.

Blade #	Amplifier #
1	ACX #1
2	PSI #2
3	ACX #2
4	ACX #3
5	ACX #5
6	PSI #1
7	ACX #4
8	ACX #6

Table 4.17 Amplifier-Blade Assignments for Blisk Modal Tests

As performed by previous researchers (19), during the first 0.25 seconds of the response data the PZT actuator was driven by the chirp. The free decay response was recorded during the succeeding 0.75 seconds. During the Case II, first bending mode tests, the time response of the fifth blade while driving the second blade PZT was plotted and is shown in Figure 4.15. Rather than a gradual, exponential decay, this example visually illustrates the differing sinusoidal responses of the closely spaced modes through a beat phenomena.

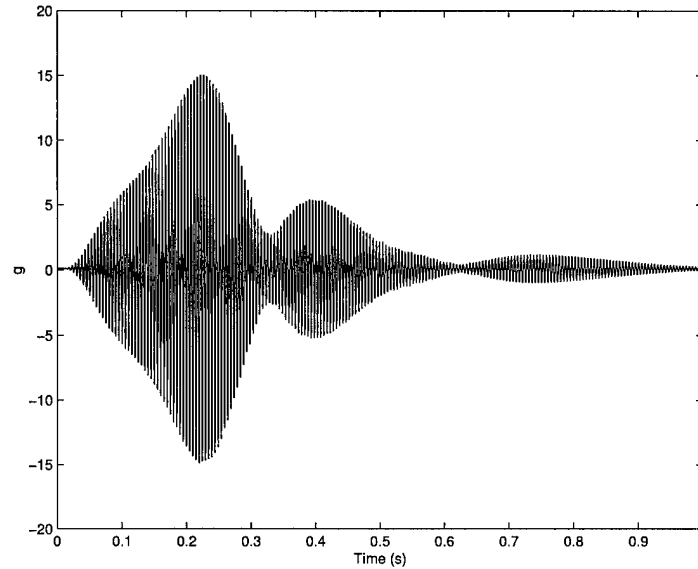


Figure 4.15 Time Response of Blade 5 during Blade 2 Excitation - 1<sup>st</sup> Bending, Case II

By weaving the eight SIMO test runs into a psuedo-Multiple Input Multiple Output (MIMO) (18) data set, an ERA analysis was employed on the decay data. The beginning of the decay portion analysis began at the 1100<sup>th</sup> data point, or 0.2686 seconds after the forcing input commenced. The cutoff for data analysis was the 3147<sup>th</sup> data point, or at 0.7683 seconds. This bracketed set contained only free response data of the structure and was more than ample for the modal identification task.

Because of mode splitting, several approaches to analyze the data were made before all eight modes in each family were successfully identified. In similar tests, decimating free decay data by factors of 5 and 10 produced favorable outcomes (8). Unfortunately, for this study, these attempts did not identify all the individual modes. Ultimately, Hankel matrix sizes were widely varied before finding a data matrix of suitable columns and rows that yielded good results. Increasing the Hankel matrix well beyond that previously recommended (4)(19) was the only method found that allowed the ERA to completely separate the modes and characterize the system. The Hankel Matrix dimensions and singular value truncations for both cases are listed in Table 4.18. The modal results of the analysis are displayed in Tables 4.19 and 4.20.

	Case I		Case II	
	1 <sup>st</sup> Bending	1 <sup>st</sup> Torsion	1 <sup>st</sup> Bending	1 <sup>st</sup> Torsion
Hankel Matrix	1200x600	1200x600	1200x600	1200x600
SV Cutoff	59	59	55	57

Table 4.18 Hankel Matrix Dimensions & Singular Values for Bladed Disk Modal Tests

	Case I			Case II		
Mode #	Freq. (Hz)	Zeta (%)	EMAC	Freq. (Hz)	Zeta (%)	EMAC
1	203.2	0.5341	96.66	201.1	0.3928	99.67
2	207.5	0.3999	99.23	202.6	0.3789	99.79
3	208.8	0.3702	99.43	202.9	0.3945	99.77
4	209.2	0.5871	98.87	203.1	0.4083	99.80
5	209.5	0.5018	99.36	203.5	0.5011	99.80
6	210.3	0.5196	99.40	203.9	0.4989	99.54
7	211.4	0.4462	99.03	204.1	0.5928	99.57
8	213.8	0.8740	97.92	207.2	0.7330	97.41
Mean	209.21	0.5291	98.84	203.55	0.4844	99.42
Std. Dev. (%)	1.47	29.64	1.97	0.86	24.00	0.82

Table 4.19 Blisk Natural Frequencies and Damping Ratios - 1<sup>st</sup> Bending Mode

	Case I			Case II		
Mode #	Freq. (Hz)	Zeta (%)	EMAC	Freq. (Hz)	Zeta (%)	EMAC
1	553.4	0.2097	98.25	553.9	0.1651	97.88
2	554.5	0.2123	99.16	554.5	0.2229	98.75
3	554.5	0.2360	98.24	554.6	0.1728	98.68
4	555.1	0.2134	99.37	555.2	0.1786	99.24
5	555.3	0.3067	98.90	555.5	0.2226	99.48
6	558.2	0.1746	98.81	557.8	0.1802	99.19
7	559.0	0.2251	97.19	559.3	0.1617	99.28
8	559.6	0.2850	97.69	559.5	0.2917	98.68
Mean	556.20	0.2329	98.45	556.29	0.1994	98.90
Std. Dev. (%)	0.42	18.49	0.76	0.40	22.19	0.52

Table 4.20 Blisk Natural Frequencies and Damping Ratios - 1<sup>st</sup> Torsion Mode

Figures 4.16 through 4.19 display the ERA generated mode shapes, normalized by the first component. The four/two norms and infinity/two norms, as outlined in Chapter 1, are shown in Tables 4.21 and 4.22. The tuned system norms of Chapter 2 are used as the base set to compare localization effects.

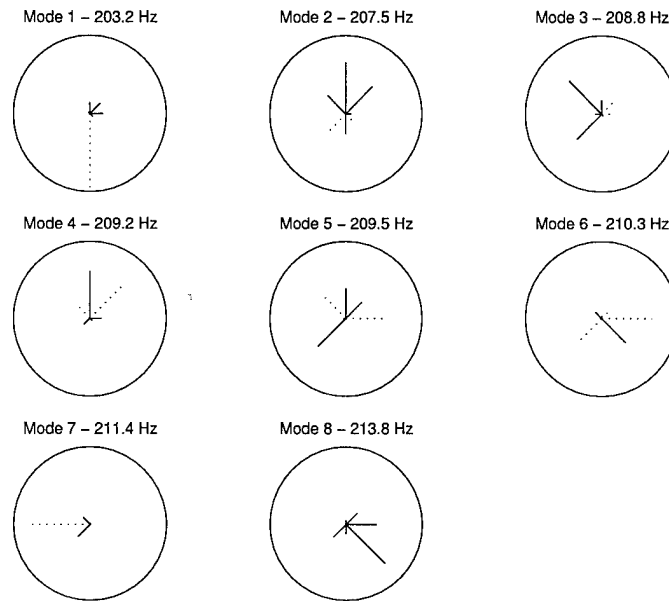


Figure 4.16 Normalized Mode Shapes - Case I, 1<sup>st</sup> Bending Mode

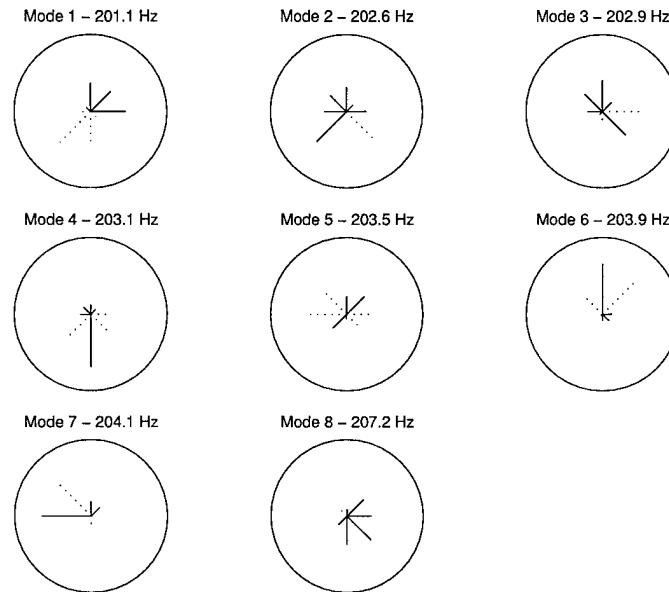


Figure 4.17 Normalized Mode Shapes - Case II, 1<sup>st</sup> Bending Mode

As anticipated, the STD of the first bending modal frequencies is significantly lower for Case II compared to Case I. In contrast, there is no significant difference between the two cases for the first torsion mode. Overall, the spread of damping ratios is rather high,

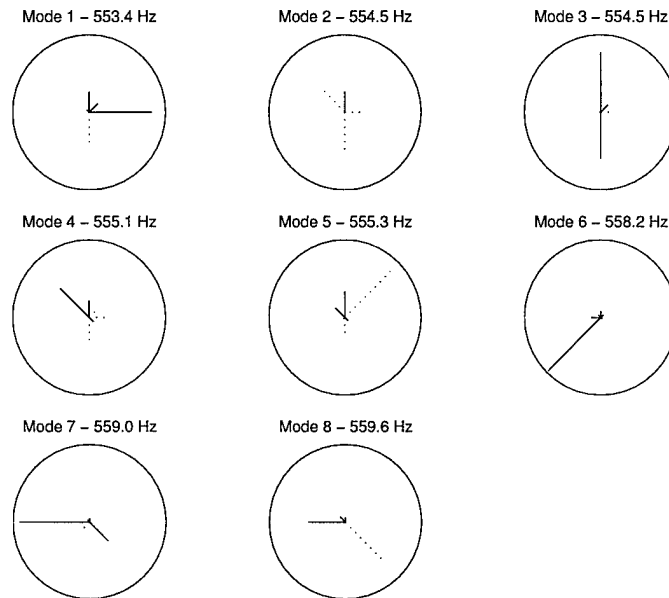


Figure 4.18 Normalized Mode Shapes - Case I, 1<sup>st</sup> Torsion Mode

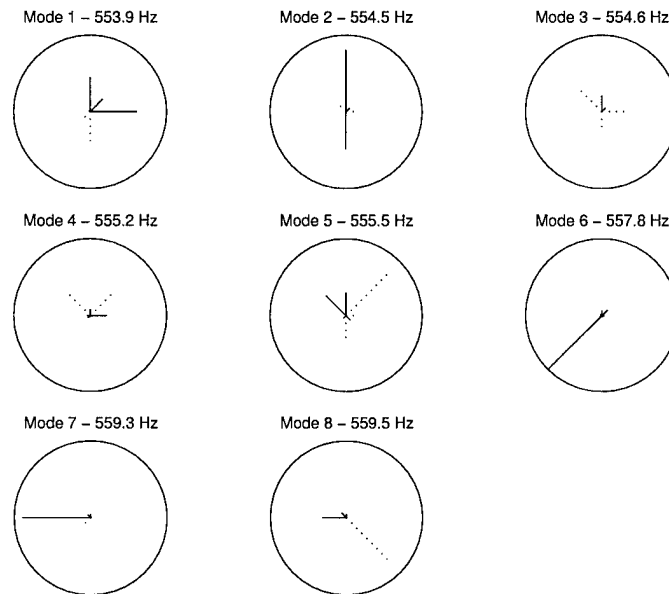


Figure 4.19 Normalized Mode Shapes - Case II, 1<sup>st</sup> Torsion Mode

indicating the difficulty of obtaining consistent damping ratios throughout a specific modal band.

Comparing the norm scales of the first bending family, all eight global mode shapes are less localized for Case II compared to Case I. In particular, modes on the band ends

	Case I		Case II	
Mode #	$L_{four}$	$L_{\infty}$	$L_{four}$	$L_{\infty}$
1	0.152	0.372	0.601	0.625
2	0.657	0.753	0.832	0.889
3	0.500	0.691	0.818	0.845
4	0.632	0.740	0.695	0.672
5	1.117	0.938	1.303	0.885
6	0.498	0.686	0.523	0.749
7	0.233	0.529	0.459	0.737
8	0.263	0.437	0.533	0.606

Table 4.21 Free Response Norm Scales of Bladed Disk - 1<sup>st</sup> Bending Mode

	Case I		Case II	
Mode #	$L_{four}$	$L_{\infty}$	$L_{four}$	$L_{\infty}$
1	0.233	0.421	0.384	0.519
2	0.524	0.721	0.345	0.602
3	0.376	0.642	0.559	0.710
4	0.745	0.702	0.633	0.719
5	0.405	0.938	0.605	0.641
6	0.199	0.508	0.196	0.505
7	0.256	0.543	0.196	0.506
8	0.234	0.435	0.171	0.385

Table 4.22 Free Response Norm Scales of Bladed Disk - 1<sup>st</sup> Torsion Mode

were most significantly improved. This is more pronounced in the four/two norm than the infinity/norm. There are arguably similar overall localization effects throughout the torsion mode for Case I and Case II. However, since localization improvement of this modal band was not the emphasis of the Case II mass additions, the results are reasonable.

There were two unanticipated discrepancies with the mode shapes. Although the disordered mode shapes had different blade amplitude responses than their tuned counterparts, they should still have semblance of inter-blade phase angle. Observing the figures, this is not the case. Consequently, the mode shapes determined by the ERA analysis contained significant complexity. Complex mode shapes are expected in any real-life structure due to damping, however the severity was much greater than expected. Normalization of the mode shapes by the first component reduced the complexity, although a substantial portion of remained. Therefore, the mode shapes have been plotted with the imaginary

portions dropped. Being extremely sensitive to mistuning and other perturbations, these complex mode shapes further indicate the extreme difficulty of modal testing a real-life bladed disk assembly. Similar difficulties were encountered in past studies, although suitable explanations to the exact cause were uncertain (16). Some steps that might help reduce the modal complexity include:

1. Using similar amplifiers to drive all PZT actuators. Although input levels were closely controlled, subtleties in different models can lead to an ERA analysis of inconsistent time response data.
2. Lag in alignment of the chirp decay data by the ERA due to delays in energy transmitted from the driving PZT, through the hub on to individual blades.
3. Minor variations in individual PZT Quickpack coupling properties.

In any event, the existence of complex modes in disordered periodic systems is a region where further research is required.

## 4.6 *Forced Response Experimentation*

Having gathered the essential transient response data of the bladed disk, the bladed disk forced response can be undertaken. The intent of these particular experiments is to construct blade forced resonant response curves at various engine orders throughout a predetermined frequency region. The frequency band will encompass a single modal family of interest. Knowing the frequency band for both vibrational modes of interest, calculations were required to determine the flywheel RPM speed necessary to excite a specific modal band at a given engine order. These rotational velocity conversions for both the first bending and torsion vibrations are exhibited in Tables 4.23 and 4.24.

Case #	Freq. Range	E.O. 2	E.O. 3	E.O. 4	E.O. 6	E.O. 12
I	200 - 215 Hz	6000-6450 RPM	4000-4300 RPM	3000-3225 RPM	2000-2150 RPM	1000-1075 RPM
II	197 - 210 Hz	5910-6300 RPM	3940-4200 RPM	2955-3150 RPM	1970-2100 RPM	985-1050 RPM

Table 4.23 Modal Frequencies to Flywheel RPM Conversions - 1<sup>st</sup> Bending

As previously outlined, the limitations of the flywheel motor speed were evident here. Due to the high RPM speeds necessary for various E.O./mode combinations, certain test

Case #	Freq. Range	E.O. 2	E.O. 3	E.O. 4	E.O. 6	E.O. 12
I	548 - 565 Hz	16440-16950 RPM	10960-11300 RPM	8220-8475 RPM	5480-5650 RPM	2740-2825 RPM
II	543 - 575 Hz	16290-17250 RPM	10860-11500 RPM	8145-8625 RPM	5430-5750 RPM	2715-2875 RPM

Table 4.24 Modal Frequencies to Flywheel RPM Conversions - 1<sup>st</sup> Torsion

runs were impossible to conduct. For example, experiments could not be not pursued with E.O. 2. Similarly, forced vibrational response of the first torsional mode were only studied with E.O. 6 and 12. Unfortunately, this restricts the amount of experimental data gathered. As a result, careful analysis in the next chapter is critical to extract the most benefit from these resonant vibration tests.

Another unforeseen obstacle was the HP Tachometer. Although the tachometer functioned properly for the input force characterization, SignalCalc 620 software measurements of the tachometer for a steady flywheel RPM did not remain constant for this experimental portion. Instead, the tachometer RPM reading fluctuated anywhere from  $\pm 10$  RPM to  $\pm 50$  RPM even with a stabilized flywheel speed. Such wavering measurements would introduce error when converting the RPM speed back to a forcing input frequency. The higher the engine order, the more gross the inaccuracies would become. This was very discouraging since the original intent of the software was to record the RMS time response data of the accelerometers through an RPM sweep of a vibration mode. Each response frame would be stamped with the RPM speed at the instant of record, and exported into a MATLAB® formatted file for analysis and construction of the resonant response curves.

Fortunately, an RPM measurement gauge was already owned by the AFIT laboratory and proved to be a suitable substitute. The device operated as a non-contact approach to measuring the flywheel RPM. The timing gun was aligned within the plane of the flywheel and projected a scanning laser along the flywheel rim. A reflective patch was adhered to the flywheel outer edge to increase feedback response. As the flywheel spun, a digital filter inside the timing gun sampled response data from the reflective patch. This average response voltage was converted to an RPM number and displayed on the gun's digital output screen. A photo of this revised setup is shown in Figure 4.20.

A new system for data acquisition was required which, with user intervention, still maintained significant precision in aligning time response captures to the proper RPM

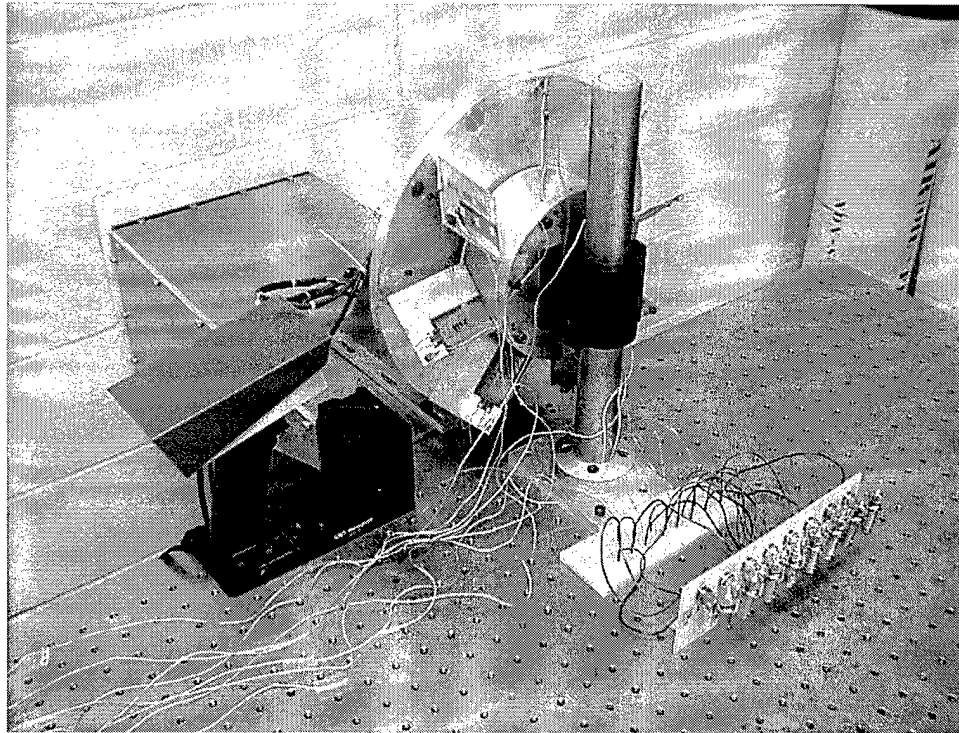


Figure 4.20 Forced Response Testing with RPM Timing Gun

speed. Since the RPM gun only measured rounded integer values of the RPM speed, the maximum number of collectable data points for a test run was the spread of integers within the RPM brackets listed in Tables 4.23 and 4.24. Instantaneous records of blades resonant responses were manually collected with the SignalCalc 620 software. For each E.O./vibration mode pair, the frequency step between captures are outlined in Table 4.25.

E.O.	Case I		Case II	
	1 <sup>st</sup> Bending	1 <sup>st</sup> Torsion	1 <sup>st</sup> Bending	1 <sup>st</sup> Torsion
3	0.1 Hz	N/A	0.05 Hz	N/A
4	0.133 Hz	N/A	0.067 Hz	N/A
6	0.1 Hz	0.1 Hz	0.1 Hz	0.2 Hz
12	0.2 Hz	0.2 Hz	0.2 Hz	0.2 Hz

Table 4.25 Frequency Steps Between Forced Response Data Points

Frequency steps are directly related to the consecutive RPM integer increase of the RPM gun for a given engine order. For all test runs the bladed disk was aligned parallel to the flywheel with a 0.4 in separation, as indicated in the input force characterization

section, between flywheel and blade magnets. This distance provided adequate blade response without exceeding the forcing vibration limits of the ENDEVCO® accelerometers. For each simulated engine order, the flywheel was configured with the appropriate number of magnets. The input voltage to the flywheel motor was manually controlled through the digital voltmeter. For a given engine order and vibration mode, upon stabilizing the flywheel speed at the bottom threshold of each RPM range given in Tables 4.23 and 4.24, the voltage was then incremented in 0.01 V steps to ensure each RPM integer step was properly recorded. Snapshots of the accelerometer RMS values (g) were recorded until the RPM sweep was completed. Equipment settings for all forced response tests are shown in Table 4.26.

Freq Bandwidth (Hz)	Accel Range (V)	Time Span (s)	Data Points	Block Size
1600	$\pm 1.0$	0.25	400	1024

Table 4.26 Bladed Disk Forced Response Test Equipment Settings

It should be noted by the reader that because of these restraints with the RPM gun, not all test runs gathered the same number of data points. This leads to differing levels of resolution amongst the data sets. Moreover, since the data points are manually accumulated, there was a potential for minor error in the data. For instance, if the rotational acceleration of the flywheel was too large due to the voltage input, manual time captures would be taken faster than the established HP/PC time span refresh rate. The consequence would be identical data records for neighboring frequency steps. To prevent this, multiple tests were conducted and several graphical output plots generated to ensure the final results were repeatable and accurate.

## 4.7 Summary

A thorough explanation of the experimental procedure was discussed throughout the chapter. In addition, the details of the individual blade and bladed fan modal tests were also outlined and results presented. By altering the blade masses, two free response cases were compared and discussed. To encapsulate, these changes in mass caused Case I to suffer more severe mode localization than Case II. Suggestions for further study were made in

the area of complex mode shapes and localization parameters. Furthermore, challenges during the experiments and troubleshooting approaches were revealed as encountered.

This free response data will assist explanation of forced vibration responses. Since the blade disk forced response behavior is the focus of this study, these plots, localization parameters and subsequent discussions have been reserved for the following chapter.

## *V. Results and Discussion*

Presented in this chapter are results from the numerous forced response tests conducted with the procedure outlined in Chapter 4. In addition to comparative analyses amongst the individual runs, qualitative comparisons to prior studies that are readily identifiable will be made howsoever possible. Unlike the mathematical models of periodic structures, many of the bladed disk's physical properties, such as blade number or structural coupling, are unalterable without considerable modifications to the bladed disk. For this reason, conclusions drawn between experimental data and previous research can be somewhat limited in scope. However, because of the statistical nature of mistuning, it is extremely important to define precisely what each specific analysis actually implies, and to be wary of excessive generalization (13).

### *5.1 Forced Response Data Arrangement*

Even with the limited number of cases studied, an immense amount of data was generated. From necessity, the analyses must be confined to manageable proportions and organized in a orderly, yet summarized fashion. This will aid in extracting the key results from which maximum benefit can be derived. With this motivation, three figures were generated for each data set. These were found to best illustrate blade responses, blisk response and localization effects. Two figures are sets of individual blade responses and the response of the whole bladed disk. Each data set also includes a plot of the four/two and infinity/two norms at each test point throughout the indicated frequency band. Similar to the Chapter 2 numerical analysis, the four/two norm will be the preferred norm scale to determine system global and local behavior. Conversely, the infinity/two norm will be used to determine maximum system deviations (i.e. peak blade magnitude). As an example, the series of figures associated with Case I, E.O. 3, 1<sup>st</sup> bending mode are shown in Figures 5.1 through 5.3.

Unfortunately, the enormity of total figures prohibits their complete presentation in this chapter. Alternatively, remaining tests runs are succinctly compiled in Appendix B.

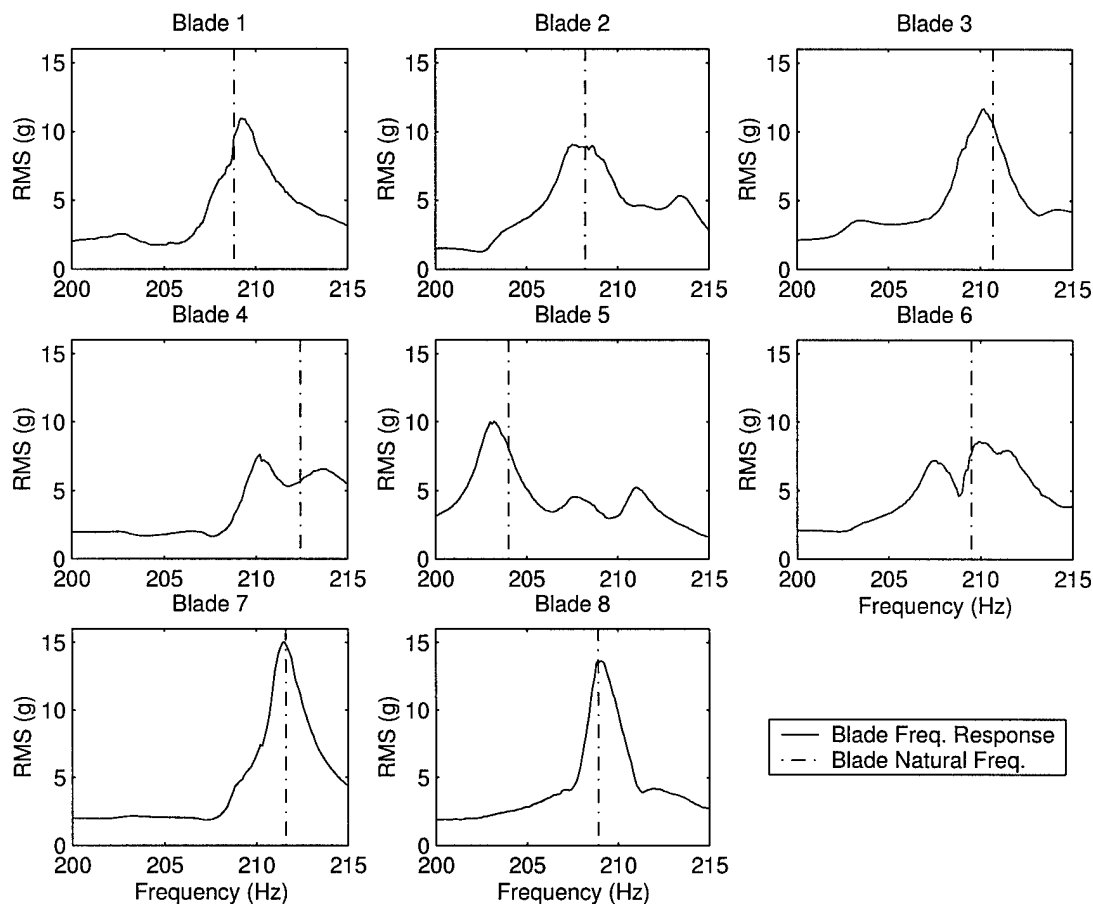


Figure 5.1 Individual Blade Responses - Case I, E.O. 3, 1<sup>st</sup> Bending Mode

Further, tables are compiled wherever deemed appropriate to help further convey observations.

## 5.2 *Presentation of Results*

Results have been segmented into four areas. The first section contains broad observations pertinent to all tests. The remaining analyses compare individual test runs under the following categories: mistuning effects, engine order variations and modal families. Since mistuning variations have been the primary focus of much prior research, it will receive the greatest emphasis. Although there is certain overlap among the discussions presented in each section, such occurrences will be appropriately referenced.

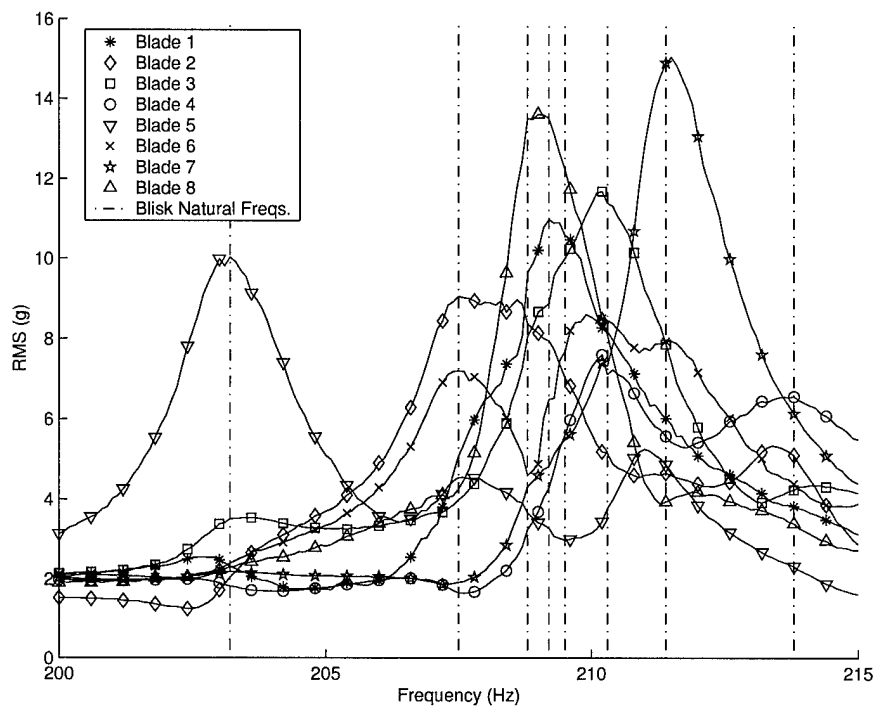


Figure 5.2 Blade Responses - Case I, E.O. 3, 1<sup>st</sup> Bending Mode

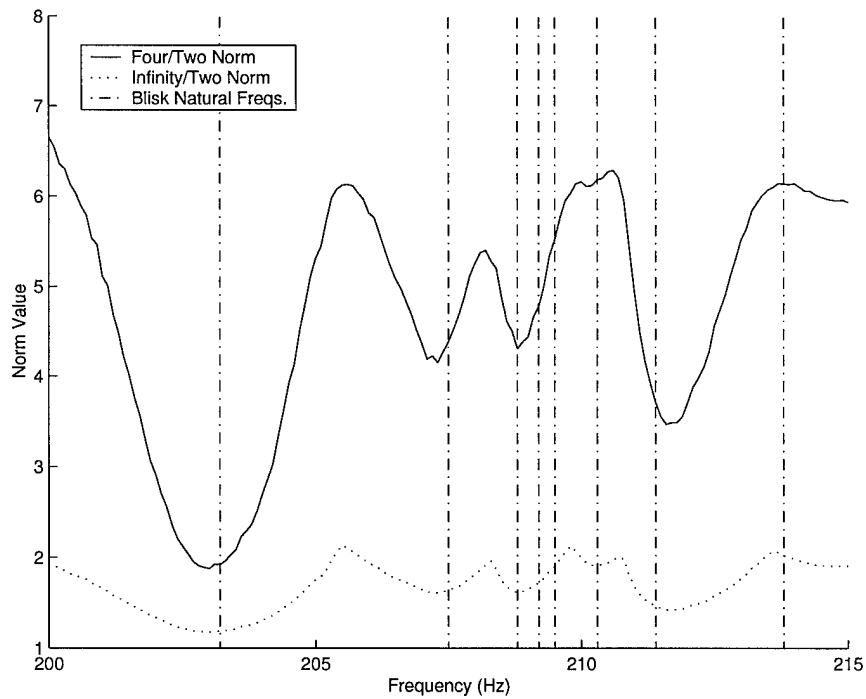


Figure 5.3 Four/Two and Infinity/Two Norm Plot - Case I, E.O. 3, 1<sup>st</sup> Bending Mode

### 5.2.1 General Observations.

**5.2.1.1 Modal Family Excitation.** It is well documented, for a tuned system, an  $m$ -nodal diameter mode will only be excited by a harmonic  $m$  E.O. source. This feature disintegrates with mistuning effects, where each mode contains a component of almost every diametral order. Therefore, mistuned modes are excitable by multiple engine order excitations according to the magnitude of the  $m$ -nodal diameter component in its modal shape (11). Since all test runs were mistuned to some extent, this result was visible throughout all experimentation. Several first bending and torsional modes were excited by every engine order, although specific characteristics of each response varied. These results were consistent to that observed with the numerical model.

**5.2.1.2 Campbell Diagram of Test Article.** Similar to operational bladed disk assemblies, the model fan experienced resonant vibration behavior at a multitude of forcing frequencies. This forced response behavior can be illustrated through a vibration amplitude-frequency plot over a broad range of flywheel speeds. Commonly referred to as a Campbell Diagram, constructing this experimentally measured interference diagram normally reveals significant system vibrational information.

Normally, bladed disk resonant responses are spread over several densely packed frequencies and RPM combinations. Because of the discrete sampling method of the test data and the inability to graphically distinguish increasing response magnitudes, an exact depiction of a Campbell Diagram is not possible. As a substitute, the peak response of each blade has been plotted for each engine order superimposed with the blisk natural frequencies of interest. This modified Campbell Diagram for all Case I test runs is shown in Figure 5.4. Further, an expanded plot of the bladed disk first bending mode and E.O. 3 intersection is also shown in Figure 5.5. Clearly, the interrelation among engine order responses is evident. Radial lines depict forced vibration at several of these integral engine orders. Horizontal lines show numerous bladed disk natural frequencies at which the system is constantly excited by random disturbances. When these two separate lines cross, resonant conditions occur (11). An initial observation of the system, explored further

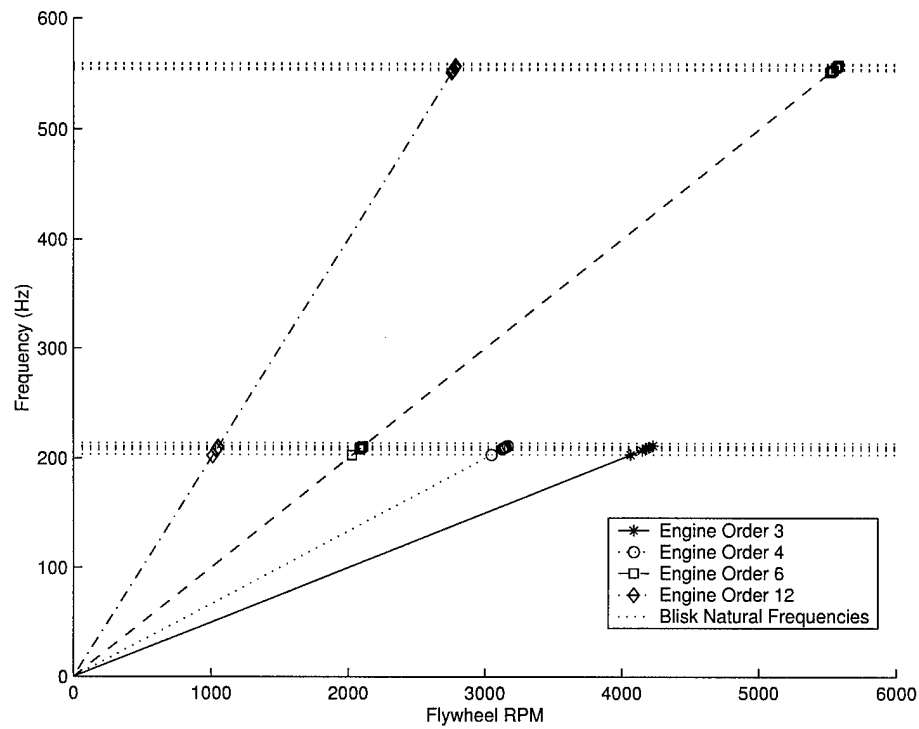


Figure 5.4 Experimental Blisk Campbell Diagram

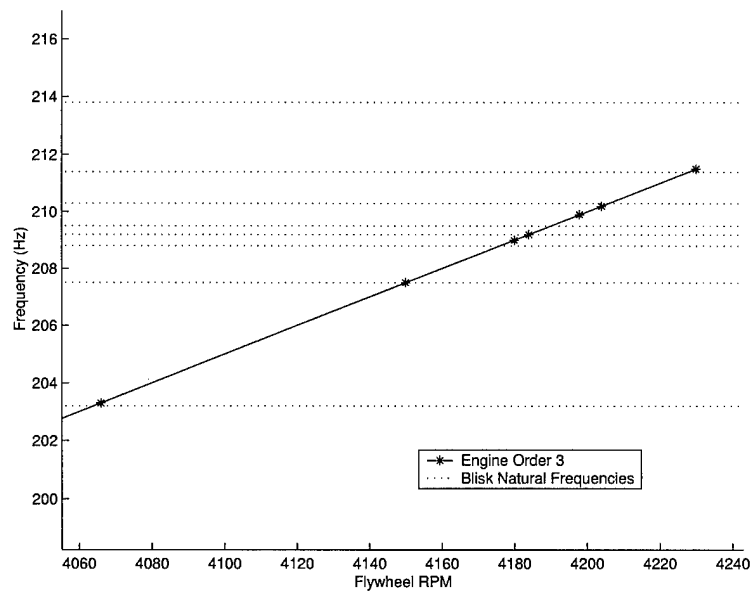


Figure 5.5 Magnified Bladed Disk 1<sup>st</sup> Bending Mode and E.O. 3 Intersection

in the subsequent results discussion, is peak blade responses do not necessarily occur at bladed disk modes.

Not indicated on the Campbell Diagram was the occurrence of subharmonic resonant responses. These phenomena occurred at integer divisions of the fundamental modal family frequencies. Their existence stems from the superposition of several multiple degree-of-freedom system resonant and anti-resonant responses (3). Subharmonics stem from the periodic, sinusoidal nature of the input and is related to the higher harmonics observed in the forcing input characterization section. Including these subharmonic incidences would unnecessarily clutter the Campbell Diagram without addition insight into the modal responses. Nevertheless, for illustration, Figure 5.6 shows the first six subharmonic components for E.O. 12. Each subharmonic is appropriately labeled, for instance, 2T is the 2<sup>nd</sup> subharmonic of the first torsion mode.

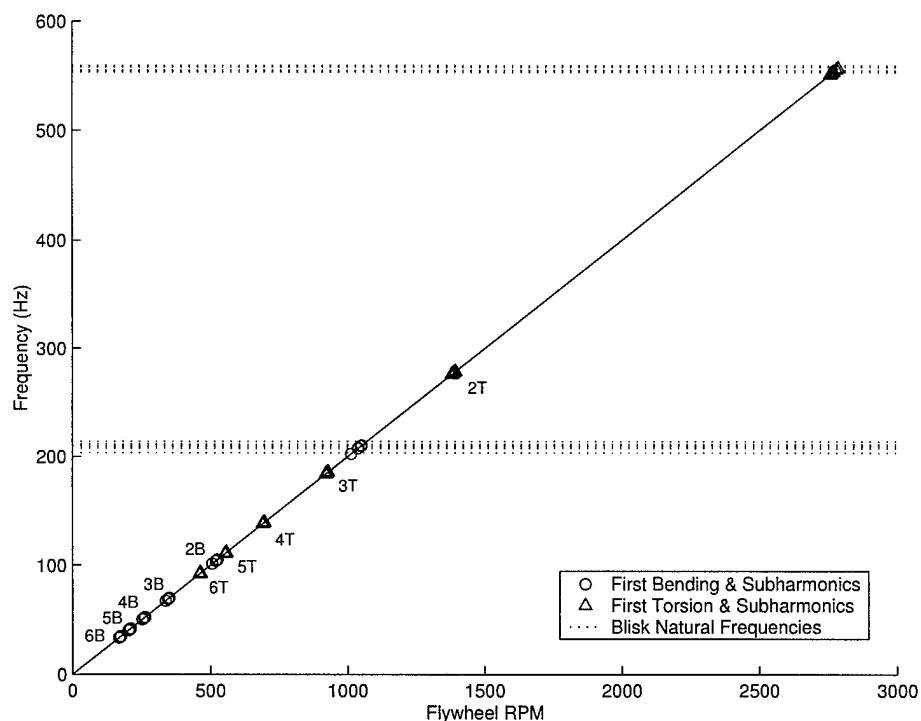


Figure 5.6 Subharmonics of E.O. 12

The magnitude of subharmonic blade resonances diminished with increasing harmonic component number. Although difficult to discern through Figure 5.6, harmonic bandwidth decreased as the subharmonic number grew larger. Bending-torsion coupling was also observed in the higher harmonics. Because of these characteristics, the subharmonics became increasingly difficult to analyze at lower frequencies. With noticeable

similarities between the resonant subharmonics and fundamental modal harmonics, their localization properties are important to characterize. However, their analysis was beyond the intended scope of this study and left for future research.

**5.2.1.3 Peak Blade Responses.** Of major significance in forced vibrational behavior is the maximum amplitude a blade will experience throughout a frequency sweep. Even more desirable is cognitive knowledge of the likelihood a blade would exceed a critical amplitude value (34). Although this critical value is not known for the current system, comparing blade responses can portray the relative extent to which individual substructures are experiencing stress and strain. Tables 5.1 through 5.4 show the maximum responses of each blade for every test run. Due to the wealth of information, these tables will be referred to repeatedly in subsequent sections.

	E.O. 3	E.O. 4	E.O. 6	E.O. 12
Blade	RMS (g)	RMS (g)	RMS (g)	RMS (g)
1	10.974	12.497	19.497	43.337
2	9.063	13.291	23.037	41.024
3	11.693	15.387	14.802	47.087
4	7.603	6.903	18.246	25.400
5	10.027	12.623	19.637	42.473
6	8.607	12.149	20.512	44.770
7	15.064	20.974	22.390	62.780
8	13.629	15.118	22.390	50.744
Mean	10.832	13.618	20.564	44.702
Std. Dev. (%)	23.57	28.99	16.84	23.34

Table 5.1 Maximum Blade Responses - Case I, 1<sup>st</sup> Bending Mode

In every instance, the variance in blade amplitudes is readily apparent. This agrees with the findings of Ewins (13)(11), yet contradicts Pierre (40) who claimed comparable blade peak amplitudes for a weakly coupled system. A plausible explanation for the differences with Pierre's findings may lie with his mono-coupled numerical model, while the test article blades experienced dual coupling effects, structural and aerodynamic. Hence, vibration energy interaction amongst individual substructures is different due to this extra coupling avenue.

	E.O. 6	E.O. 12
Blade	RMS (g)	RMS (g)
1	38.985	110.811
2	42.096	104.369
3	40.107	120.197
4	45.029	112.783
5	56.184	143.065
6	61.526	154.882
7	56.649	148.423
8	30.578	92.244
Mean	46.395	123.347
Std. Dev. (%)	22.97	18.43

Table 5.2 Maximum Blade Responses - Case I, 1<sup>st</sup> Torsion Mode

	E.O. 3	E.O. 4	E.O. 6	E.O. 12
Blade	RMS (g)	RMS (g)	RMS (g)	RMS (g)
1	9.168	13.774	11.696	42.867
2	8.676	11.642	11.679	39.284
3	8.406	11.214	12.179	35.725
4	14.174	16.053	16.028	45.429
5	12.010	20.376	11.985	57.724
6	10.782	14.297	18.595	45.863
7	12.339	14.054	19.755	50.282
8	12.812	15.774	11.761	48.103
Mean	11.046	14.648	14.210	45.660
Std. Dev. (%)	19.26	19.67	23.95	14.81

Table 5.3 Maximum Blade Responses - Case II, 1<sup>st</sup> Bending Mode

#### 5.2.1.4 Individual Blade Peak Response Frequencies. Unfortu-

nately, a firm connection between peak blade amplitudes and the frequency this peak response would occur is difficult to surmise, although some limited conclusions may be made. The individual blade response figures indicate peak blade deflections typically occurred in the vicinity of the individual blade natural frequencies or at slightly lower excitation frequencies. This is opposite to the finding of Pierre (40), who stated the resonant frequencies of a weak coupled assembly consistently become marginally larger than the individual blade frequencies.

Perhaps more beneficial would be the ability to predict whether peak blade amplitudes normally occurred close to the bladed disk free response modes instead of individual

	E.O. 6	E.O. 12
Blade	RMS (g)	RMS (g)
1	12.196	118.646
2	10.053	115.388
3	12.152	127.833
4	23.399	102.056
5	12.040	139.942
6	23.336	151.202
7	23.705	152.111
8	11.733	95.810
Mean	16.076	125.381
Std. Dev. (%)	38.37	16.96

Table 5.4 Maximum Blade Responses - Case II, 1<sup>st</sup> Torsion Mode

blades. Studying the collective blade response figures, it appears that for a more tuned system (i.e. Case II), a majority of the maximum blade deflections are closely grouped around the free modes. Blades of extreme mistune, such as blade five in Case I, also appear to reach a maximum response near a free response mode. Furthermore, for the given external forcing, the peak blade responses tend to drift to lower frequencies and away from the blisk free modes with increasing engine order. This shift with engine order may be simply caused by the increase in pulse energy with engine order suggested in the input force characterization section of Chapter 4. Pierre (40) noted that weakly coupled systems are more prone to large blade amplitudes at lower excitation frequencies when mistuned, regardless of the engine order. However, Pierre's analysis was with cases sharing a common mean blade natural frequency. This is not true here, hence the two results cannot be compared.

Despite these remarks, it would not be prudent to assume the blisk peak forced responses usually occur near the free modes. Statistical analyses of the bladed disk and further research of the periodic forcing function are necessary to provide more grounded conclusions. Inter-blade coupling, damping and changing forcing function properties can incite dramatic shifts in the frequencies at which peaks occur. These effects will be investigated further with the variance of engine order.

**5.2.1.5 Highest Response Blade.** Contrary to results produced by Ewins (13) that stated the maximum overall blade response is borne by the blade with

the lowest response frequency, examining the individual blade responses within each data set revealed a high-frequency blade consistently exhibited the peak response. The highest frequency blade was the peak blade in four data sets while the second highest frequency blade was attributed with seven data sets. This is certainly a limited conclusion, since coupling effects and the mistuning pattern arrangement could most certainly effect the results. Further, Ewins results were based on a lumped mass-spring model of a 33-bladed disk, rather than the experimental data of this study.

**5.2.1.6 Localization Measures.** Both the four/two norm and infinity/two norm provide similar results for all data sets. Conversely, a significant divergence between the two norms is the infinity/two norm scale can have dramatic changes, or jumps, in value throughout a frequency range, while the four/two norm has more gradual, varying values. Figure 5.7 demonstrates an example of the infinity/two norm's 'choppy' behavior with sharp, sudden peaks for E.O. 12, Case I, first torsion mode. Additionally, global minimums of the infinity/two norm do not necessarily occur at the highest amplitude blade responses. Both these observations prompt concern of the infinity/two norm exaggerating a system's susceptibility to blade damage at a certain forcing frequency. Similar conclusions were made with the numerical model results. Yet since the infinity/two norm is based on maximum deflections and primarily utilized to predict subsequent failures of individual substructures, perhaps this cautious approach is welcome. To best utilize the infinity/two norm, however, it is advisable to have as many data points as possible to best show patterns of behavior.

**5.2.2 Effects of Mistuning Strength.** Despite attempts to further globalize the first bending mode, both Case I and Case II are still considered mistuned due to slight differences in individual blade natural frequencies. Nonetheless, based on natural frequencies STD, the system depicted in Case I is eight times more mistuned for the first bending mode than Case II, with little variance in the first torsion. Because of the minimal STD change between both torsion mode cases, mistuning observations are primarily focused for the first bending mode, unless otherwise noted.

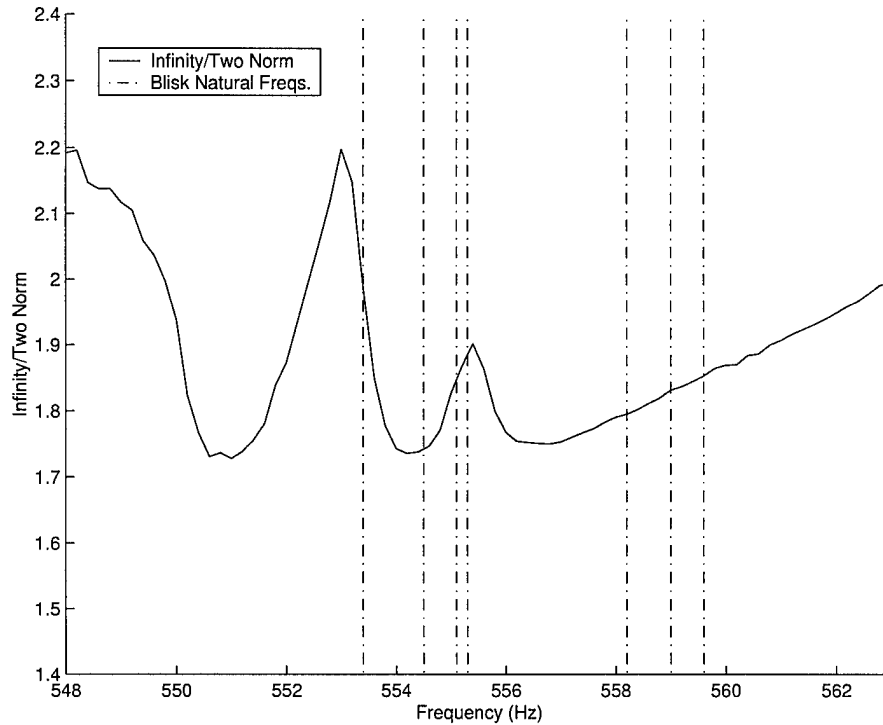


Figure 5.7 Infinity/Two Norm Scale of E.O. 12, Case I. 1<sup>st</sup> Torsion

**5.2.2.1 Blade Amplitudes.** Returning to Tables 5.1 through 5.4, between both mistuning cases there is not a significant difference in mean resonant responses of the first bending mode. Conversely, there is generally less spread of blade amplitudes for the more tuned case. Although this result seems to contradict the influences of mistuning, statistical investigations clearly show that increases in maximum amplitudes from mistuning are expected to vary among similar bladed disk assemblies (37)(8). Therefore, Case II could have exhibited significantly more favorable blade responses than Case I based on differing arrangements in blade coupling, position and damping.

**5.2.2.2 Number of Maximum Blade Amplitude Peaks.** With regards to the maximum blade response amongst all individual blades, there are noticeably more resonant peaks for the Case I first bending mode compared to Case II. As demonstrated by Pierre (40), increases in the mistuning standard deviation can cause further proportional peak splitting among maximum amplitude blade values. This, in turn, brings about a wider frequency range that contains these peaks. Figure 5.8 distinctly demon-

strates this effect for the first bending mode by plotting the overall maximum blade amplitude of the two cases with E.O. 3. The observation is less applicable for the first torsion mode because of similar mistuning standard deviation percentages among the data sets.

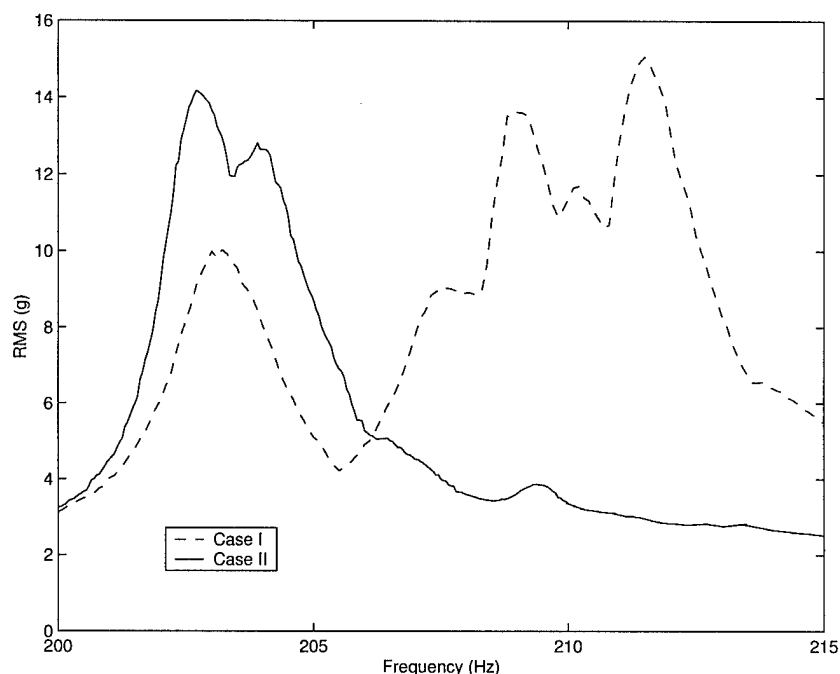


Figure 5.8 Maximum Blade Amplitude - E.O. 3, 1<sup>st</sup> Bending Mode

**5.2.2.3 Localization Effects.** Aware of the differing blade responses frequencies between the two mistuning sets, what are the localization attributes of each case? The answer lies within Table 5.5 and is representative of typical localization effects between each case. In both maximum and minimum extremes, Case I features lower four/two norm values compared to Case II, hence more localization in the response. Additionally, for both vibration modes, Tables 5.6 and 5.7 show fewer total local extremes for Case II in contrast to Case I. Local maximum and minimum were considered in a somewhat subjective fashion. Significant peaks and valleys were labeled local extremas. Additionally, several closely spaced extreme points were grouped as local maximum or minimum values. As a result, the greater mistuned Case I exhibits more localized behavior and less global behavior than Case II. It is evident that mistuning variance significantly

affected forced vibration localization. There is consistency of this finding with many prior researchers (40)(29).

	Global Minima		Global Maxima	
	Case I	Case II	Case I	Case II
$\omega$ (Hz)	203.0	202.5	210.6	208.4
$\Lambda_{four}$	1.875	5.046	6.290	7.732
$\Lambda_{\infty}$	1.178	1.745	1.962	2.465

Table 5.5 Global Norm Scale Extremas - E.O. 3, 1<sup>st</sup> Bending Mode

E.O.	Local Minimas		Local Maximas	
	Case I	Case II	Case I	Case II
3	4	1	4	2
4	4	1	3	1
6	3	1	3	1
12	4	1	3	1

Table 5.6 Number of Local Four/Two Norm Scale Extremas - 1<sup>st</sup> Bending Mode

E.O.	Local Minimas		Local Maximas	
	Case I	Case II	Case I	Case II
6	2	1	1	1
12	3	2	2	2

Table 5.7 Number of Local Four/Two Norm Scale Extremas - 1<sup>st</sup> Torsion Mode

In addition to more incidences of highly localized behavior, the endmost frequencies in a localized bandwidth spread further apart with increased mistuning. Examining the norm scale figures of each first bending data set, the localization passband associated with each engine order decreases from Case I to Case II. Table 5.8 displays these results. The transition point from a globalized to localized state was chosen at a four/two norm value of 6, and is reflected in the Table.

Case	E.O. 3		E.O. 4		E.O. 6		E.O. 12	
	$\omega \in$ (Hz)	$\Delta\omega$	$\omega \in$ (Hz)	$\Delta\omega$	$\omega \in$ (Hz)	$\Delta\omega$	$\omega \in$ (Hz)	$\Delta\omega$
I	200.5 - 213.2	12.7	200.7 - 214.6	13.9	200.6 - 213.6	13.0	200.0 - 215.0	$\geq 15.0$
II	201.8 - 203.0	1.2	202.0 - 203.2	1.2	200.2 - 201.8	1.6	200.8 - 201.9	1.1

Table 5.8 Frequency Distribution of Localization - 1<sup>st</sup> Bending Mode

Pierre (40) discovered a shift in frequency ranges dependent on the severity of mistuning. Although shifts in passband are noticeable, the mean frequency of the individual blades differs between the cases. A correlation, therefore, cannot be made in this study.

Comparing blade amplitudes and localization effects uncovers an important consideration first mentioned in the numerical analysis. Although the four/two norm value may indicate a localized state, it is not indicative of extreme peak blade responses. The four/two norm appears to serve merely as a indication of peak blade amplitudes *relative* to surrounding substructures. However, careful attention must be given to *both* conditions to adequately quantify system behavior. Unfortunately, as previously mentioned, the infinity/two norm appears incapable to compensate for the four/two norm's shortcoming in predicting peak vibrations. Certainly, several blades could undergo severe blade amplitudes magnifications, perhaps reaching a critical failure threshold, yet the four/two norm could indicate a global mode. This provokes further scepticism on the norm scales ability as a complete forced response behavior parameter.

### **5.2.3 Variance of Engine Order.**

**5.2.3.1 Increase in Mean Blade Amplitudes.** In every test run, Tables 5.1 through 5.4 all conveyed a significant increase of the mean, and individual, resonant blade response with rising engine order. This finding is dissimilar to Pierre, who concluded that engine order excitation increased the high frequency peak amplitudes while it decreases the amplitudes of the low frequency peaks for a weakly coupled blade response (40). The answer to this unusual behavior likely lies in the nature of the flywheel excitation system used to induce forced vibrations. As stated previously, magnets are substituted for wakes impinging on the blades. Airflow through an actual compressor stage transmits energy into rotating bladed disk assemblies only when the blade in question passes unobstructed airflow. On the other hand, the force interaction between the blade and flywheel magnets is related to the square of their distance. As a result, the magnets will interact throughout the entire angle of rotation between pulse inputs. As mentioned in Chapter 4, this raises the possibility that more closely spaced magnets (i.e. increasing

engine order) induce a larger amount of forcing energy into the blades. Although a possible explanation, more research on the forcing function is required to answer this question.

**5.2.3.2 Effects on Blade Responses.** Blade response profiles were also significantly influenced by the engine order. Number of peaks per blade and frequency location of peaks varied for both bending and torsion modes throughout each case. This is markedly noticed for E.O. 6, which has the most significantly different blade responses profiles for both the bending and torsion among the engine orders. These effects are somewhat expected since different natural system modes are orthogonal for varying forcing inputs. Similar to the numerical model, if the forcing phase angle coincides with a system mode, the mode will be excited. Engine orders with similar forcing phase angles should produce similar blade responses. The similarities between E.O. 4 and E.O. 12 blade response figures, which possess identical forcing phase angles, are a further testament to this forced response characteristic.

**5.2.3.3 Effects on Localization.** Since engine order effects blade response in peak splitting and frequency excitation, it is logical to conclude that localization is additionally affected. Figure 5.9 illustrates the change in the first bending mode, peak four/two norm values for all engine orders. Of significant interest is the uniqueness of E.O. 4, where the globalized and localized response slightly merge in both cases. A preliminary hypothesis to the cause of this deviation is the relationship of blades to engine order, where the engine order that coincides with half the blade number achieves less norm value spread between peak global and localized states. More analysis towards this correlation is required before any firmer conclusions can be stated.

#### **5.2.4 Comparison Between Modes.**

**5.2.4.1 Effects of Damping Strength.** Referring back to Tables 4.12 and 4.13, the first bending natural frequencies of the bladed disk are significantly damped compared to those of the first torsion. It is typical of higher modes to have less damping than their lower mode counterparts. Increased damping weakens the wave localization phenomena caused by blade to blade spatial differences, thus mistuning effects are reduced.

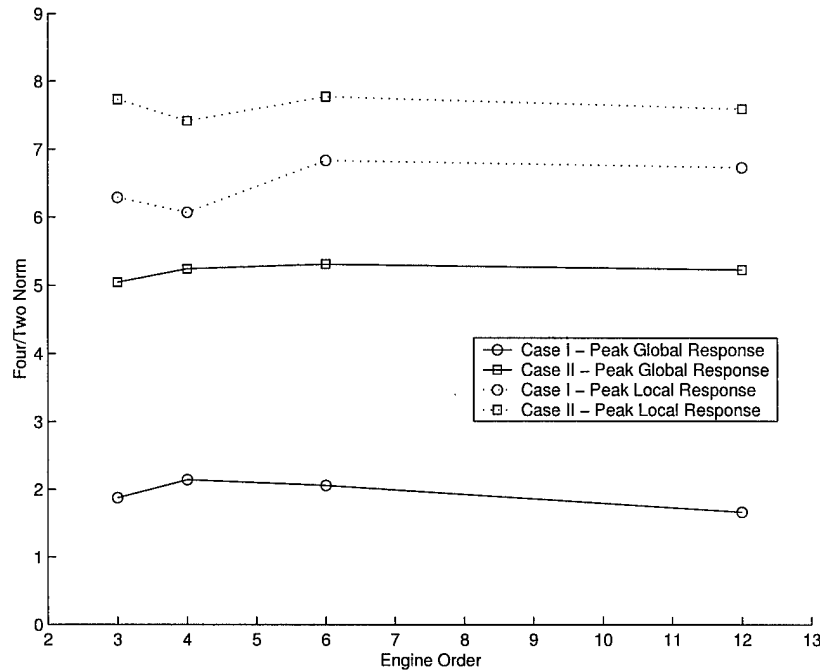


Figure 5.9 Global Maximum and Minimum Four/Two Norm Values - 1<sup>st</sup> Bending Mode

This is reflected in the mean blade responses, which are generally substantially less for the first bending than the first torsion. Damping values are fairly scattered, or mistuned, for all the blades in both modes, which may correlate with the varying amplitudes of the blades throughout all tests. This speculation would be in alignment with prior research done on damping variations throughout a bladed disk undergoing forced vibration response (27).

**5.2.4.2 Localization Effects.** Unfortunately, with the few number of data sets, it is relatively impossible to draw persuasive conclusions with regards to the effects of varying response modes on localization. Previous studies have shown that localization always occur at larger frequencies, hence at higher modes (32). Figure 5.10 shows the extreme local and global responses for all test runs, with the torsional four/two norm values embedded within the bending mode.

Comparing only two engine orders cannot constitute a trend of behavior, thus the results are inconclusive. Further, any statements would be misleading considering the several nonconstant parameters between the two modes such as damping, modal bandwidth, and

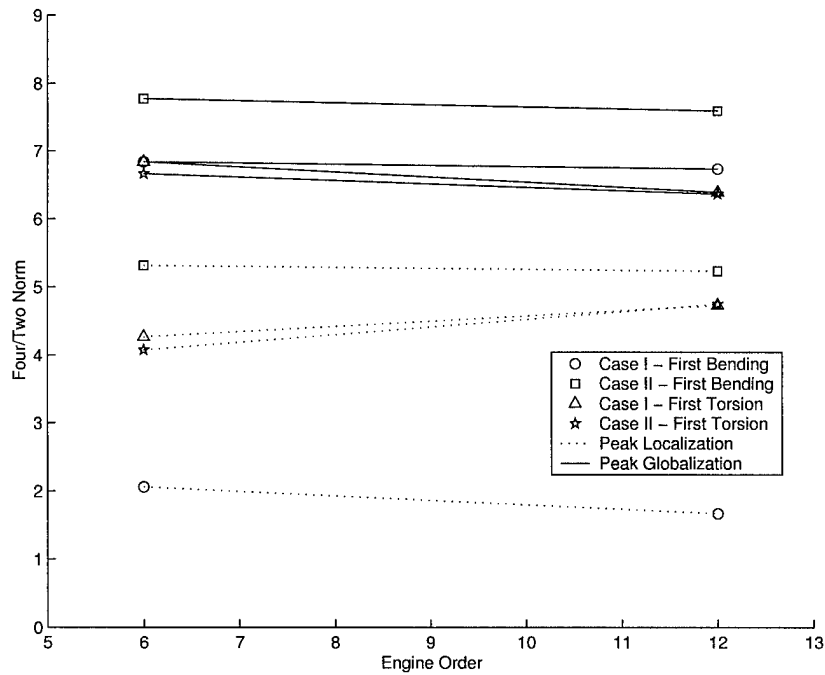


Figure 5.10 Global Maximum and Minimum Four/Two Norm Values

inter-blade coupling. More engine orders, and control over these aforementioned variables, would be needed to make credible observations.

### 5.3 Summary

Results of the bladed disk forced vibrational response via the flywheel excitation system were presented. Comparing the experimental test sets with previous works was conducted to estimate the feasibility of this external forcing system for future research. Significant conclusions and recommendations for future consideration are summarized in the next chapter.

## ***VI. Conclusions and Recommendations***

The primary thesis objective was analysis of the experimental bladed disk, forced response method for suitability towards future research endeavors. Of secondary importance was drawing comparisons between experimental data sets to supplement existing knowledge about the cyclical mistuning phenomena. Conclusions will focus on both these themes. Recommendations are condensed into two categories. The first category includes improvements to the experimental method. The second involves potential research topics toward which the flywheel excitation platform may be applied.

### ***6.1 Conclusions***

Throughout the course of this thesis, many observations were made which can be summarized in the following major conclusions:

1. The flywheel excitation system is a viable approach to simulate forced vibrations on a representative bladed disk assembly. Both bending and torsional modes of a model blisk were successfully excited with this external forcing system. With certain modifications, robustness of a data acquisition system typically used for free response modal testing allowed data collections throughout frequency sweeps of interest.
2. Forced response behavior of bladed disks are significantly dependent upon several mechanisms. Although mistuning and interblade coupling levels are commonly understood to effect localized forced vibrations, other less emphasized parameters including engine order, stimulated modal group and damping distribution can substantially alter the system response. Changing these aforementioned variables can influence localization levels, response profiles of individual blades, number of maximum blade amplitude peaks, and the frequency range in which localization occurs.
3. The periodic forcing function contains the fundamental elements of real-life periodic wakes experienced by operational bladed disk assemblies. Substituting magnets for upstream airflow obstructions produced an external force periodic in nature, composed of several sinusoidal frequencies and time varying. More characterization of

the forcing input is necessary, such as increasing blade amplitudes with rising engine order, to further understand its effects and determine if any modifications need be made to this forced excitation system.

4. The four/two norm and infinity/two norm scales produced similar trends throughout the forced response analysis. Further stated, norm scale maximum and minimum values, although different in magnitude followed similar patterns throughout a frequency band. The four/two norm seemed to express blade forced localization effects rather accurately. However, small infinity/two norm values did not always indicate a region of overall peak blade deflection throughout a passband, provoking suspicion into the infinity/two norm's reliability as a failure mode criteria for forced response behavior. This may be caused by the lack of normalization, which is incorporated into the free response analysis from which the norm values are modeled.
5. Severe forced localization is not necessarily denotative of maximum blade response. A single blade vibrating at modest amplitudes will appear more localized compared to several blades vibrating together at very large deflections. The localization parameters utilized throughout this thesis were inadequate to correlate these two traits. A proper understanding of design requirements is requisite to distinguish whether sub-component failure and/or blade amplitude distributions is the objective of analysis.

## **6.2 Recommendations**

In light of the preceding conclusions, the following sections are guidance to assist future researchers utilizing the flywheel excitation system. These suggestions are believed to be the next steps toward advancing the experimental system performance and capitalizing on this novel approach to investigating forced excitation of mistuned bladed disk assemblies.

### **6.2.1 Experimental Improvements.**

1. *Reliable Instrumentation.* Inability to use the malfunctioning HP Tachometer not only made data collection more tedious, but reduced the depths to which system

characterization could be considered. For instance, a more highly sampled data set would increase the resolution of the forced response plots which, in turn, should assist in more detailed studies of particularly interesting forced responses such as mode splitting. The RPM trigger gun, while adequate for general observations, was ill-suited to data sample frequency ranges less than a few hertz. The SignalCalc 620 software is configured to inscribe RPM inputs on respective data samples. Employing anything other than a digital tachometer for measuring flywheel speeds degrades the level of experimental accuracy. A replacement HP tachometer or different model are mandatory prerequisites for more thorough forced response system analysis.

2. *Flywheel Motor Replacement.* The Electro-Craft 3622-48-N motor driving the flywheel should be supplanted with a more powerful substitute. The 6000 RPM limit imposed by the current motor restricts the usefulness of the entire flywheel excitation system. Without a replacement, possibilities of examining the higher modal groups experienced by an operational turbine jet engine, such as the 2<sup>nd</sup> bending mode and 1<sup>st</sup> chord-wise bending (a.k.a Two-Stripe Mode), are beyond reach. Further, more diversified comparisons among engine orders can be done with a broader RPM range.
3. *Different Localization Measurement Parameters.* As previously stated, although localization effects could be characterized with the four/two and infinity/two norm values, these are better suited for free response modes. Forced response analysis is concerned not only with localized vibrations but the probability a blade would exceed a maximum amplitude value. A method that integrates both localization and peak blade responses is more appropriate for forced response analysis and should be investigated.

**6.2.2 Future Research.** Verification of the forced vibrational approach studied throughout this thesis is a prelude to a myriad of potential projects for future consideration. Experimental investigation of these topics can be compared to prior research efforts or lay precedence for emerging developments towards further understanding the sensitive dynamics of turbine bladed disks.

1. *Further Characterization of Periodic Forcing Function.* Before subsequent investigations are conducted, a more in-depth understanding of the periodic forcing function should be pursued. Mathematical analysis of the various engine order forcing profiles could provide answers for the varying spread of input frequencies and unforeseen variance in mean peak blade responses among the examined engine orders.
2. *Subharmonic Derivatives of Modal Groups.* From initial examination, blade deflections and localization experienced at subharmonic frequencies have similar potential to damage bladed disk assemblies as primary modal groups. The conjunction of primary and subharmonic resonances should be analyzed in future studies of forced response system behavior. Additionally, possible higher harmonic frequencies responses not encountered throughout the experiments should be included with these tests.
3. *Statistical Analysis of Mistuning on Bladed Disk Forced Response.* Much research into the statistical nature of mistuning has previously been complied through Monte Carlo simulations, perturbation methods (37) and reduced order modeling (6)(25)(24). Adding to this existing body of knowledge through an experimental approach would hopefully aid in further comprehending localization and blade forced response characteristics.
4. *Vibration Suppression of Forced Response Behavior with PZTs.* Properly implemented vibration suppression techniques can reduce resonant blade responses. Piezoelectric materials (PZTs) combined with a passive electrical network, active positive position feedback system or a active-passive hybrid control design could minimize mode localization while simultaneously provide consistent damping throughout individual blades (38).
5. *Effects of Differing Modal Groups On Forced Response Behavior.* Higher modes typically have more closely spaced eigenvalues, less damping and lower levels of inter-blade coupling. Modifying the flywheel motor, as suggested for experimental improvements, would provide the opportunity to quantify these key differences via forced excitation of targeted higher modal groups.

6. *Variable Bladed Disk Parameter Analysis.* Testing several fabricated blisks of varying structural properties could bring enlightenment toward their influence on forced response behavior. Some possible differences between the test articles include numbers of blades, hub stiffness, blade aspect ratios and substructure damping ratios.
7. *Expansion of Structural and Aerodynamic Coupling Effects.* Past research has considered these inter-blade coupling avenues separately, rather than jointly. However, both types of coupling need to be simultaneously analyzed to properly pattern an operational turbine bladed disk assembly. Fusion of the two is inherent with the experimental blisk model, hence the dual effects of these coupling mechanisms can be more realistically investigated.
8. *Complex Free Response Modes.* Modal complexity appeared in the free response portions of the experimental results. Particularly bothersome, the complexity seen from the ERA analysis was beyond that anticipated for a lightly damped system. Several possible explanations as to the cause of these complex modes were offered. Whether these results reflect actual system behavior or were produced from an unexplained obscurity in the analysis remains unanswered. Although similar behavior has been witnessed in prior RPS free response experiments (8), the origin of complex modes should be the focus of future research.

### **6.3 Summary**

The United States Air Force is under ever increasing pressure to sustain its aging aircraft fleet. To reach this objective, longevity of operational systems with minimal maintenance expense is critically emphasized. As a result, analysis and design methodologies that deter aircraft system failures are constantly sought. The HCF problem of jet engine bladed disk assemblies is such an area where alternative technologies are highly desired in hope of constructing a preventative solution. Before these technologies are developed, however, an increased understanding of bladed disk dynamics must be obtained.

The successful completion of this study offers a new approach towards comprehending the forced response characteristics of bladed disk assemblies. Using a reduced scale model

fan and magnetic forces to pattern aerodynamic disturbances, a relatively simple and inexpensive research platform was experimentally tested and verified. By examining the effects of mistuning, forcing input and excited modal family, consistencies with previous studies and new areas for future research were found.

Utilizing this experimental apparatus will hopefully contribute towards subsequent efforts of monitoring and controlling forced vibrational behavior of bladed disks. Reducing or eliminating turbine blade HCF would allow for lighter structural materials, increased aircraft reliability and fewer aircraft support personnel. Ultimately, aircraft performance would be enhanced and the service life of military jet engines could be extended beyond current expectations.

## *Appendix A. Supplemental Graphs - Periodic Forcing Function Figures*

The following pages include additional PSD and time response plots of the input forcing function discussed, but not presented, within Chapter 4 discussions. The information contain herein is intended to completely document all data collected from the forcing input test runs. Like the figures in Chapter 4, the figure title contains information describing a particular run.

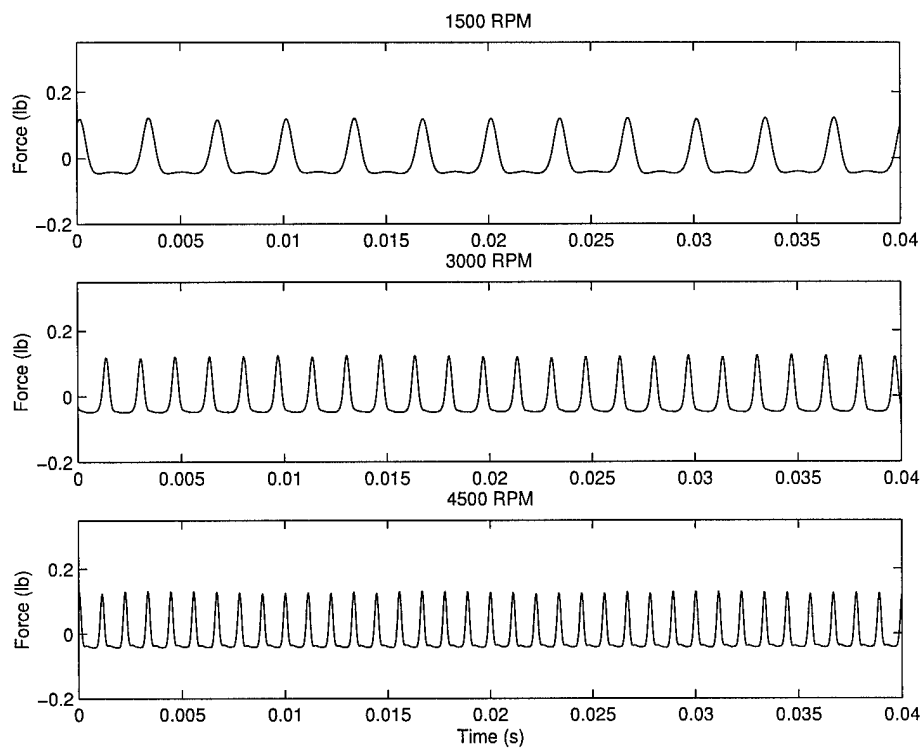


Figure A.1 Time Response of E.O. 12 with 0.4 in Spacing

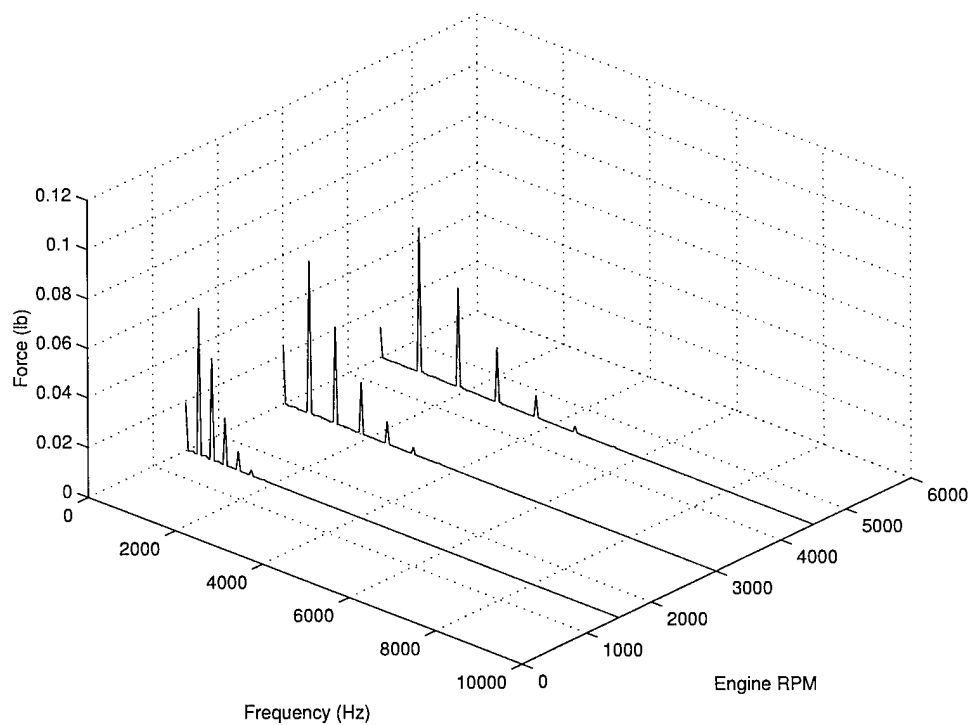


Figure A.2 PSD of E.O. 12 with 0.4 in Spacing

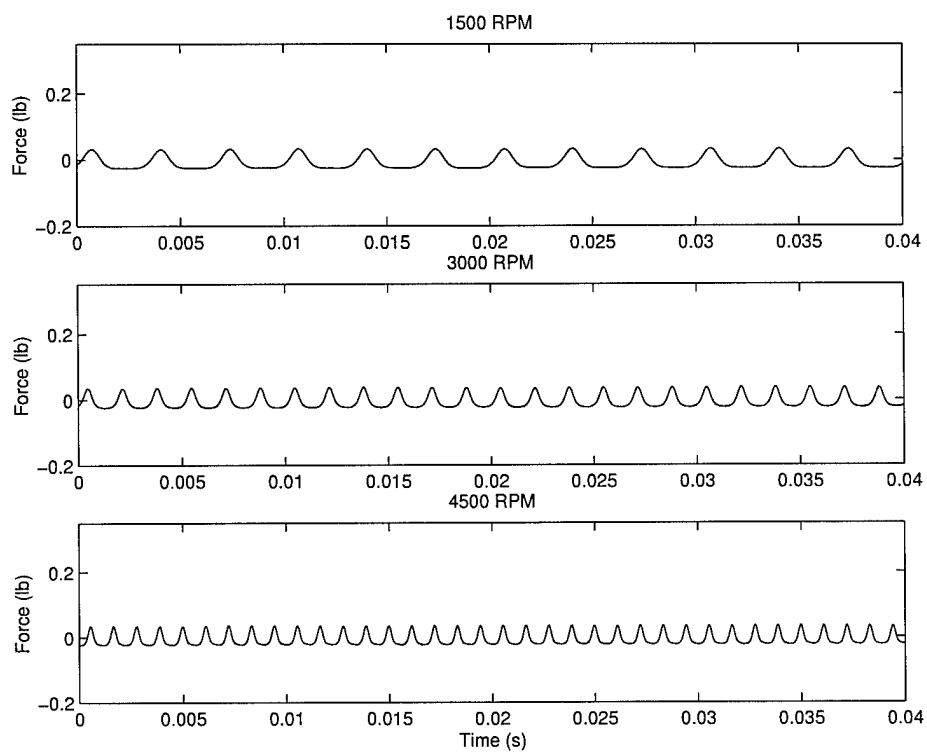


Figure A.3 Time Response of E.O. 12 with 0.6 in Spacing

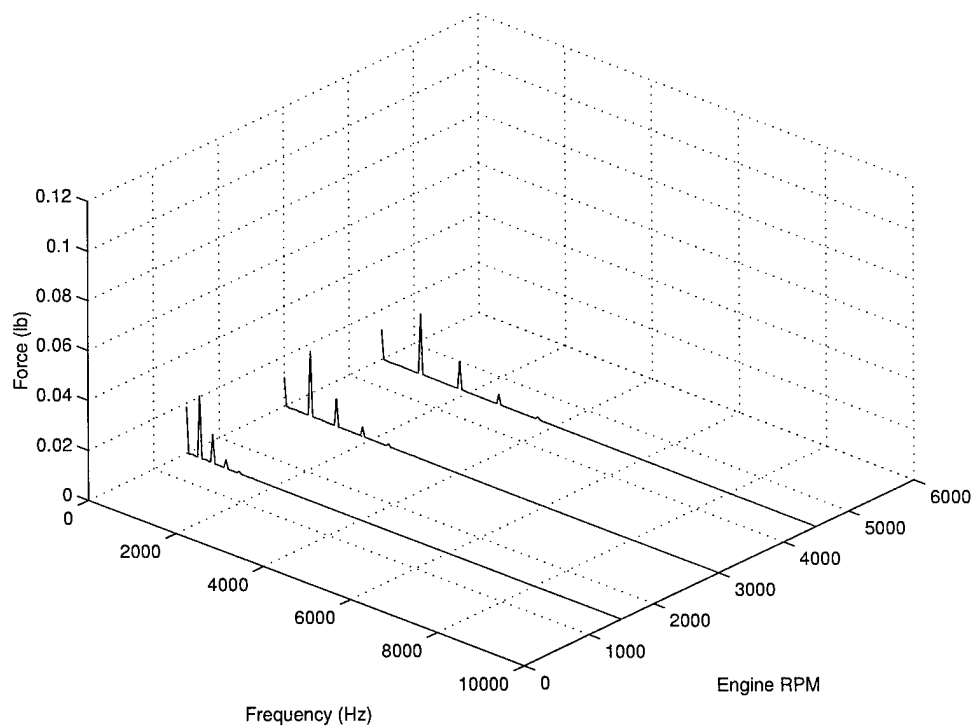


Figure A.4 PSD of E.O. 12 with 0.6 in Spacing

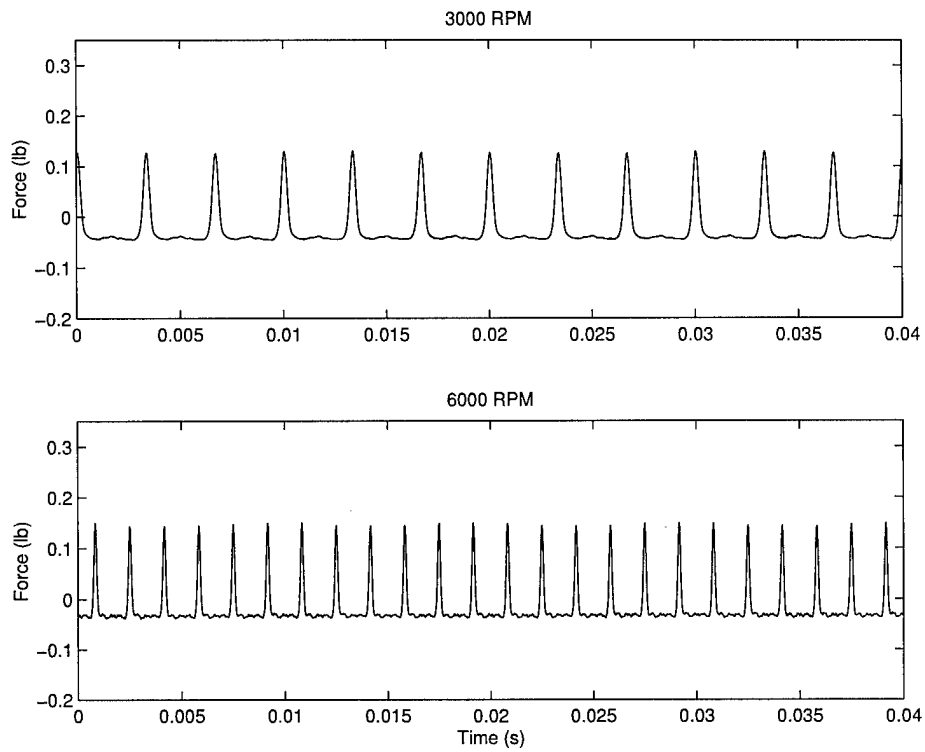


Figure A.5 Time Response of E.O. 6 with 0.4 in Spacing

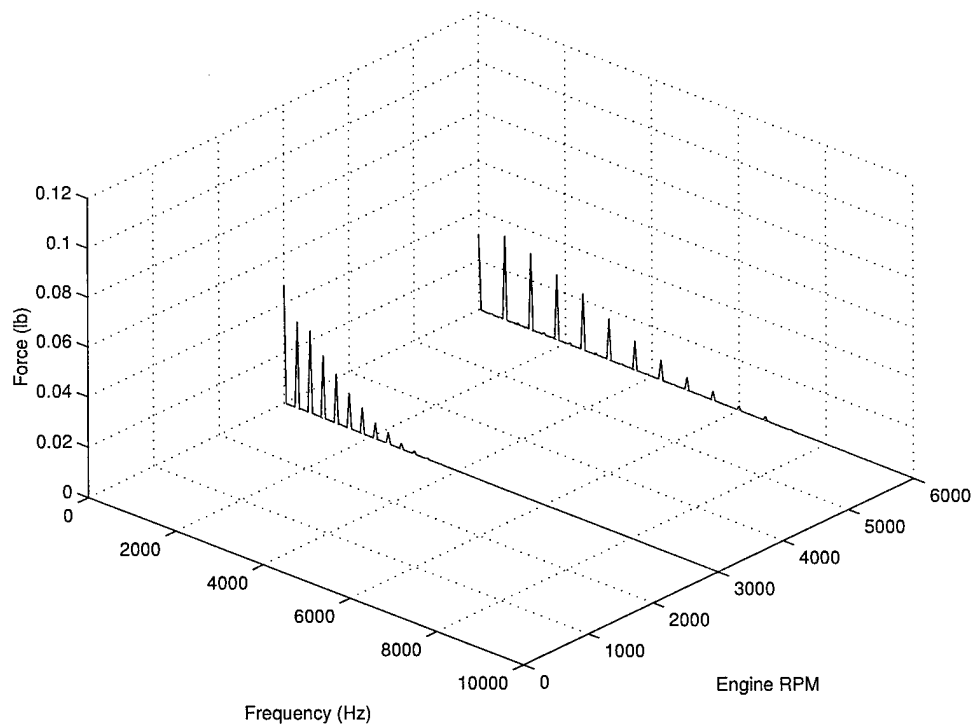


Figure A.6 PSD of E.O. 6 with 0.4 in Spacing

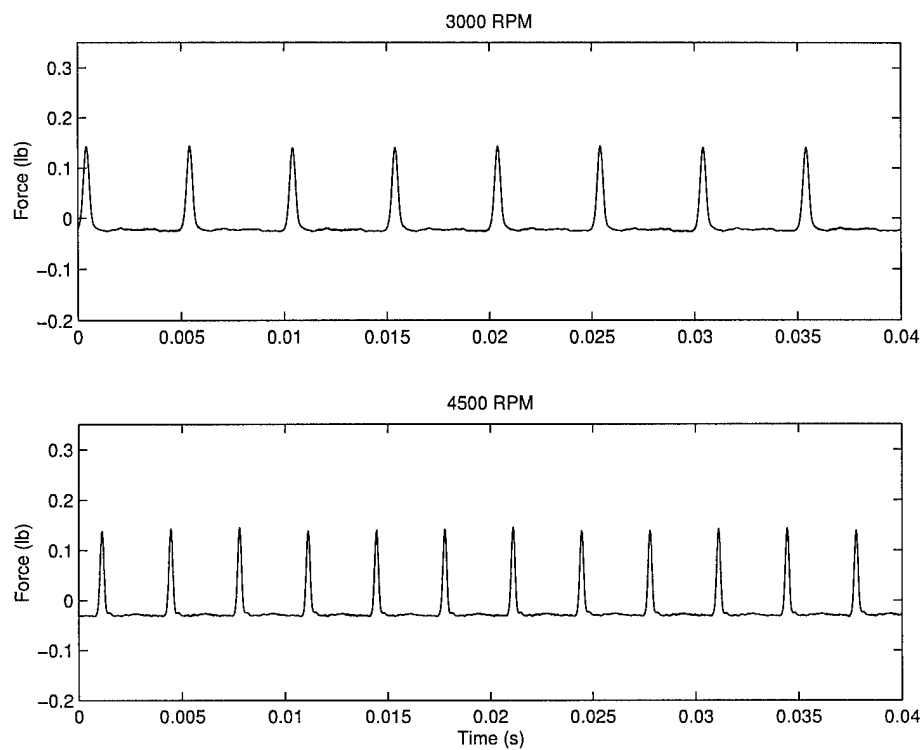


Figure A.7 Time Response of E.O. 4 with 0.4 in Spacing

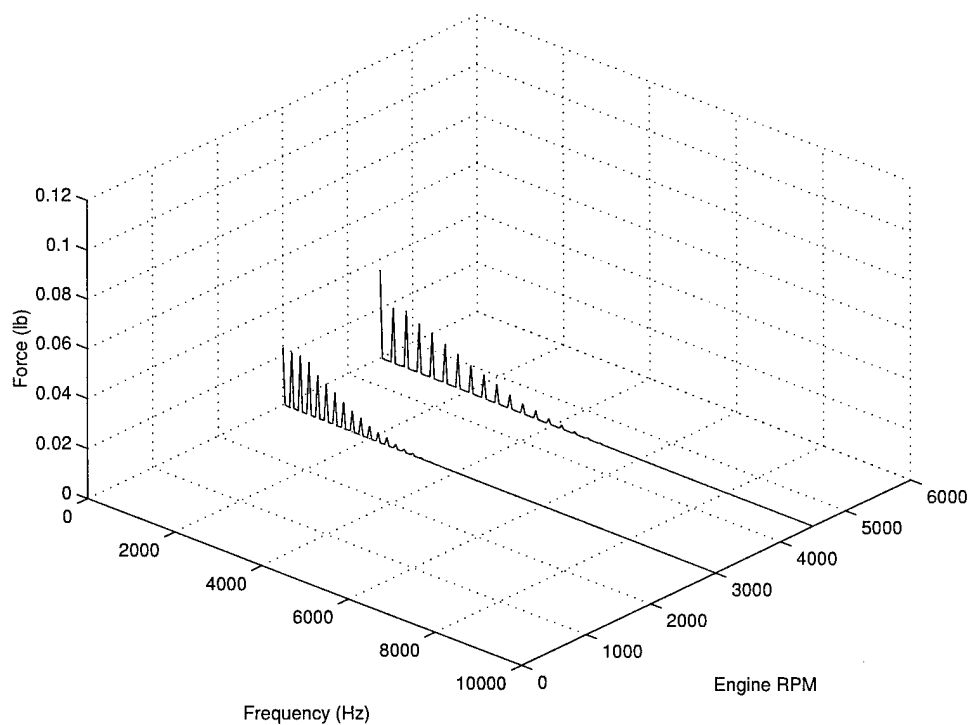


Figure A.8 PSD of E.O. 4 with 0.4 in Spacing

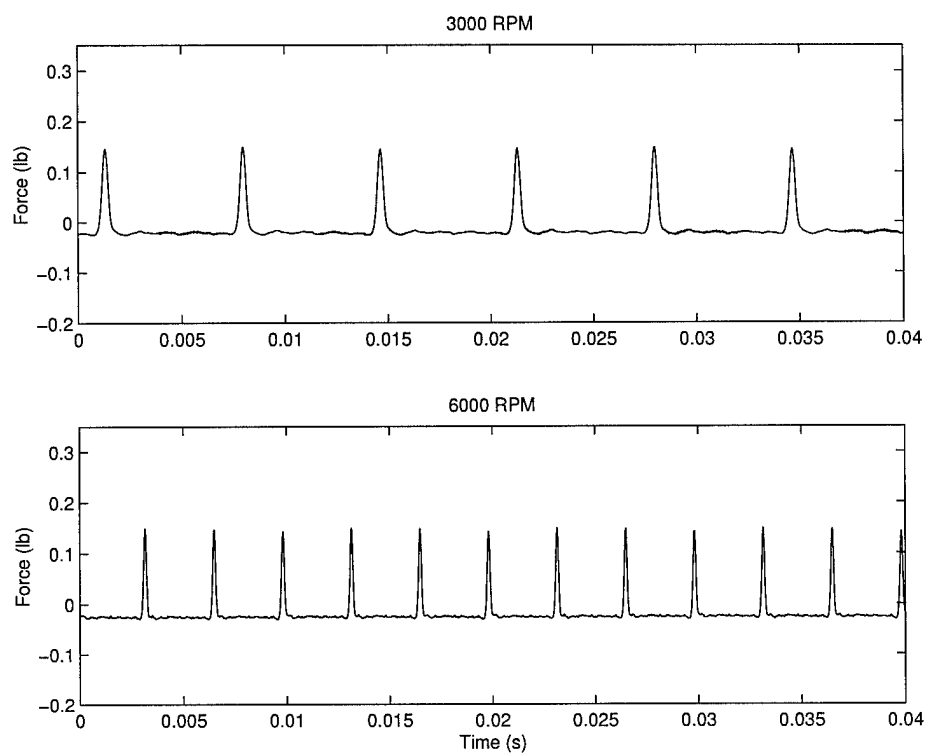


Figure A.9 Time Response of E.O. 3 with 0.4 in Spacing

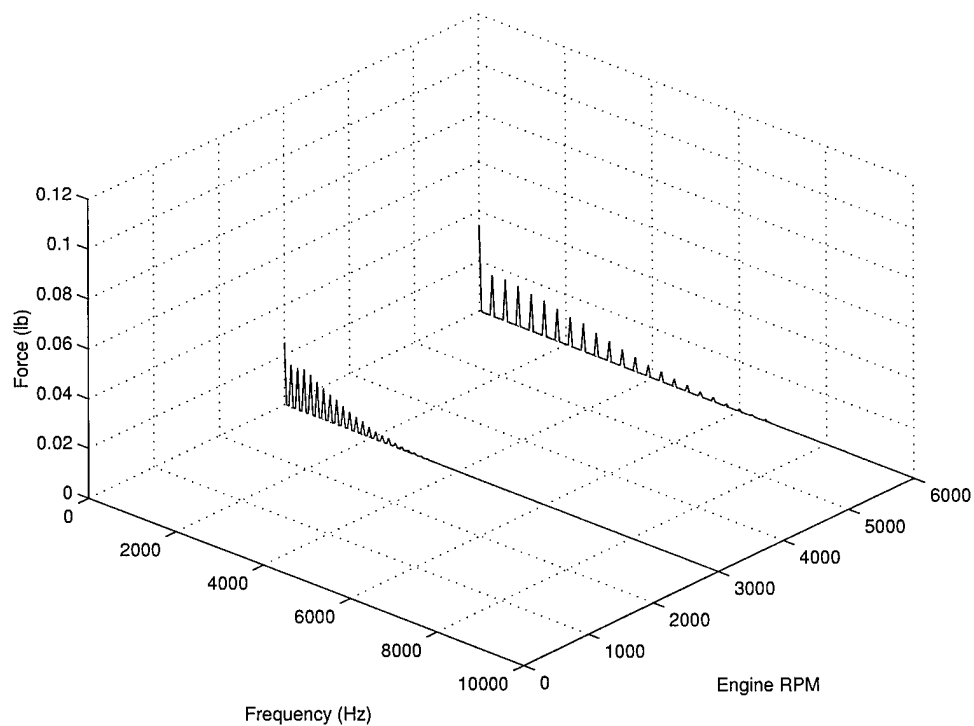


Figure A.10 PSD of E.O. 3 with 0.4 in Spacing

## ***Appendix B. Supplemental Graphs - Forced Response Figures***

Included in the following pages are engine order response figures not presented within the Chapter 5 results. The information contain herein is intended as complete documentation for all forced response experimental testing. Eleven runs are enclosed, each including the following figures:

1. Forced response of individual blades plotted with their respective natural frequency
2. Blade responses superimposed with all blade disk natural frequencies
3. A graphical representation of the four/two and infinity/two norms throughout the testing passband, overlayed with all bladed disk natural frequencies

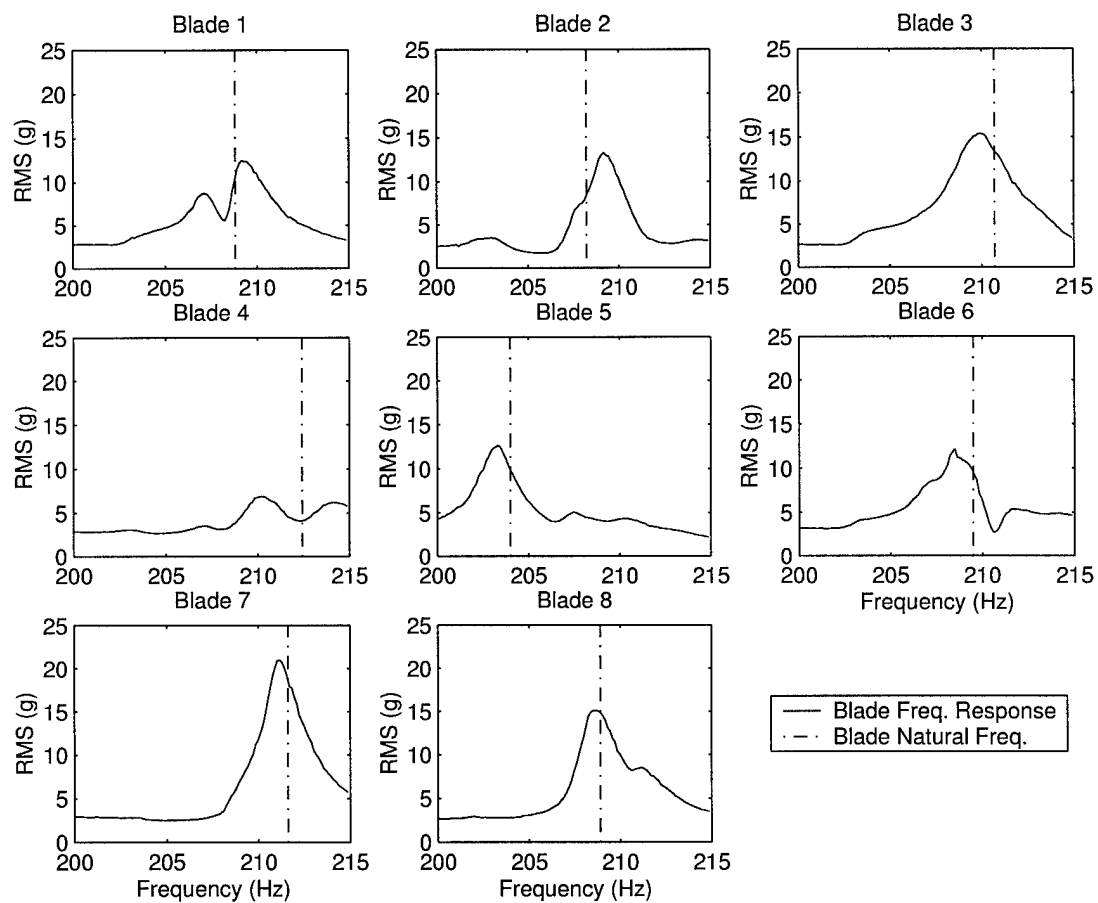


Figure B.1 Individual Blade Responses - Case I, E.O. 4, 1<sup>st</sup> Bending Mode

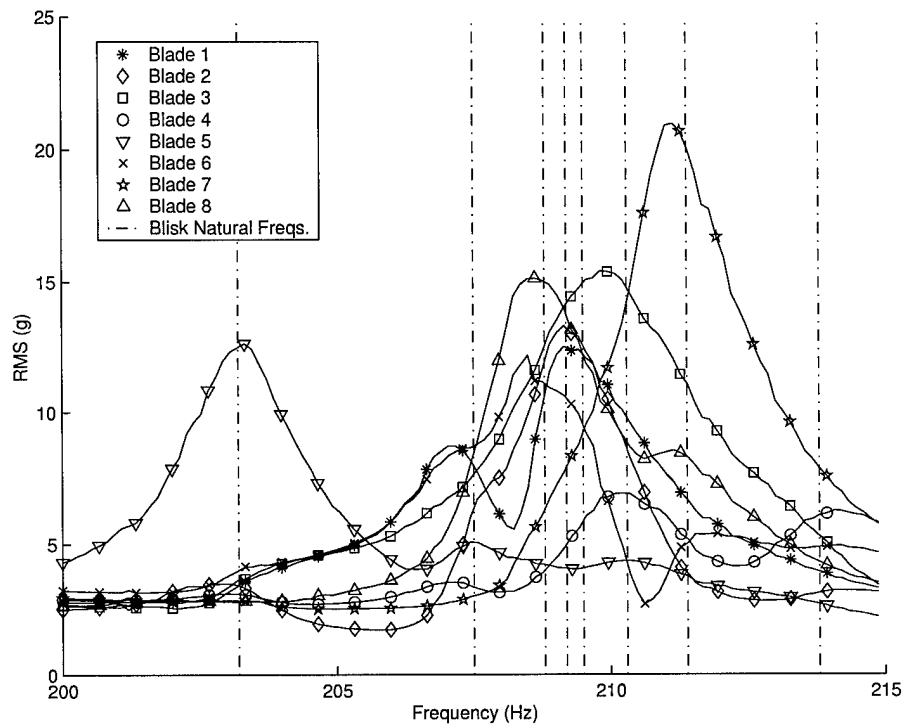


Figure B.2 Blade Responses - Case I, E.O. 4, 1<sup>st</sup> Bending Mode

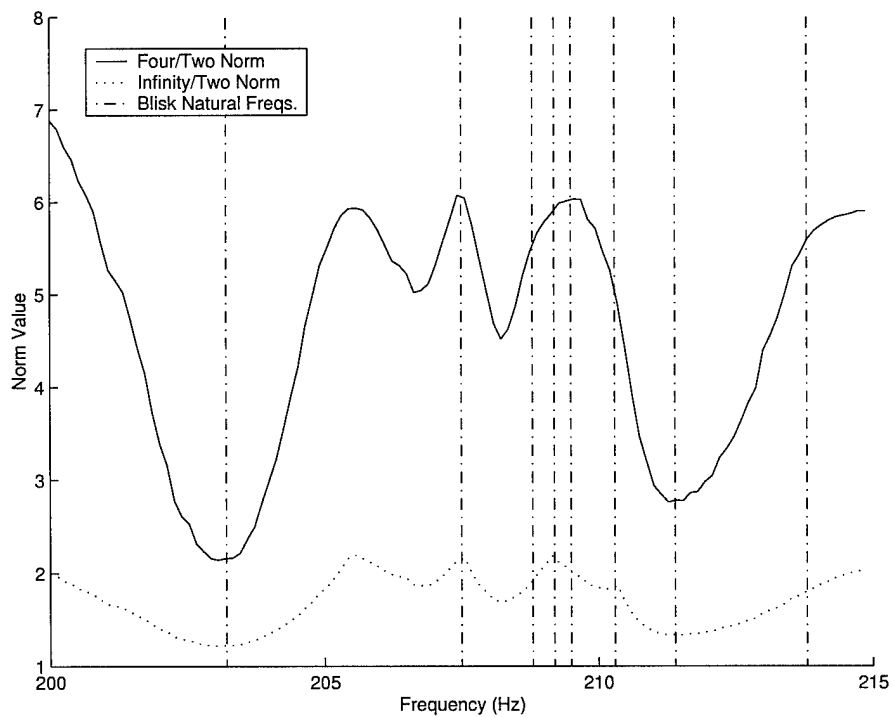


Figure B.3 Four/Two and Infinity/Two Norm Plot - Case I, E.O. 4, 1<sup>st</sup> Bending Mode

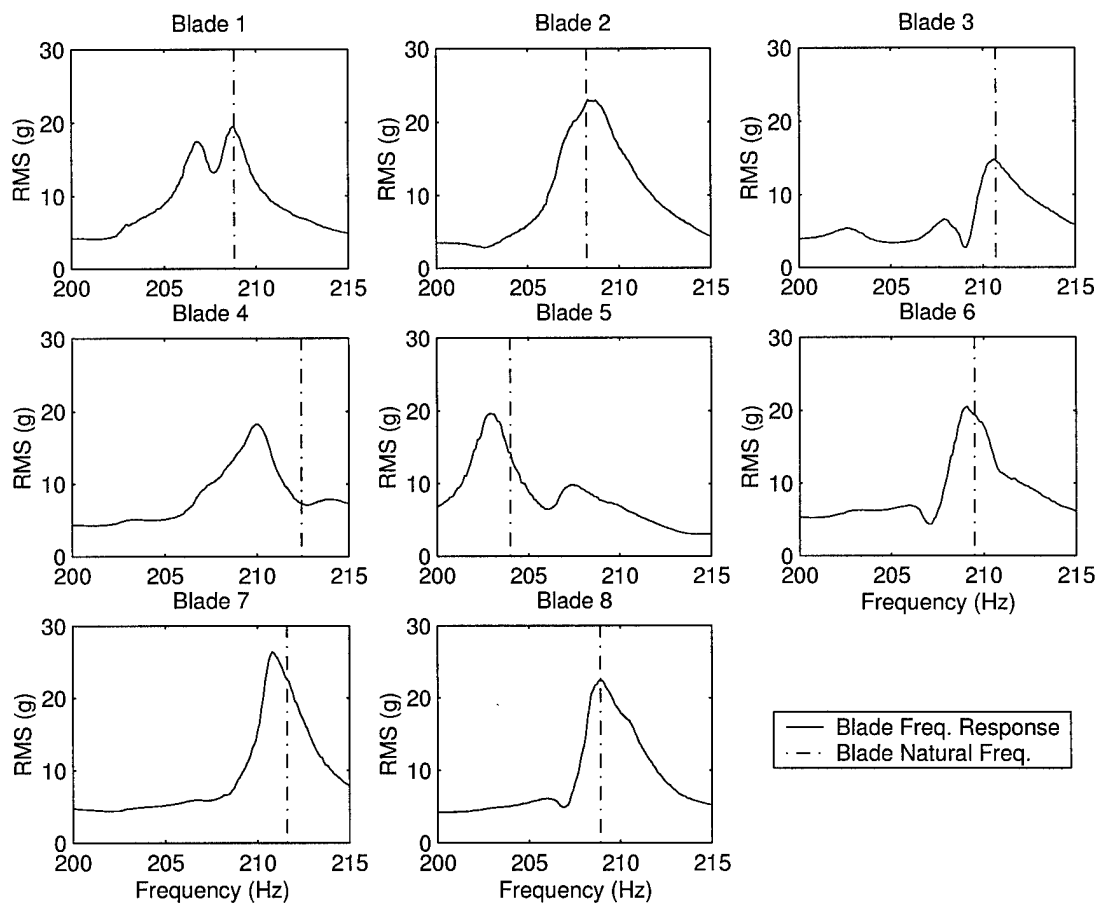


Figure B.4 Individual Blade Responses - Case I, E.O. 6, 1<sup>st</sup> Bending Mode

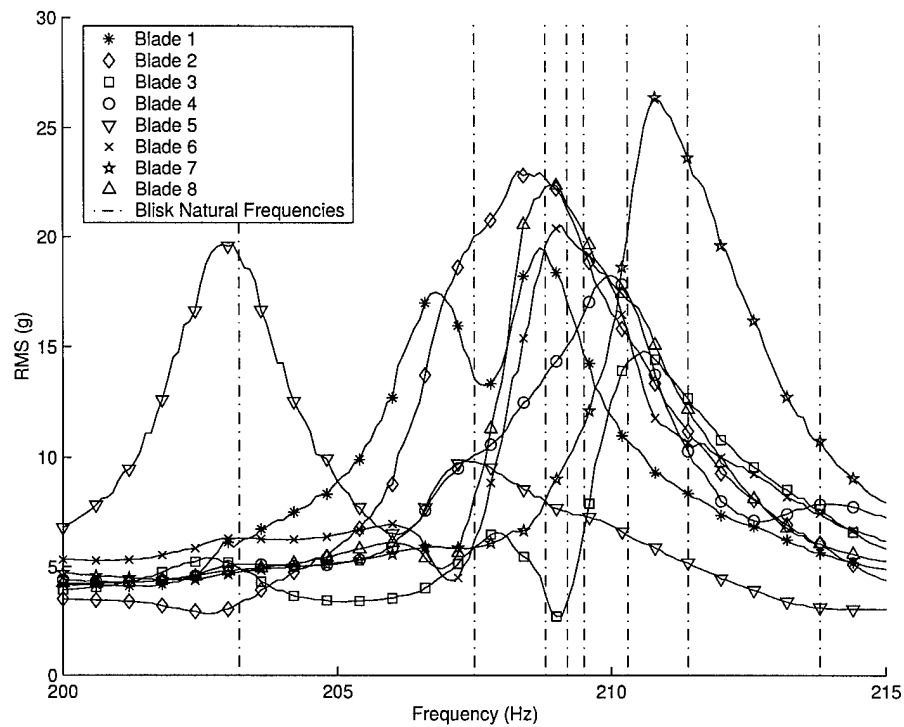


Figure B.5 Blade Responses - Case I, E.O. 6, 1<sup>st</sup> Bending Mode

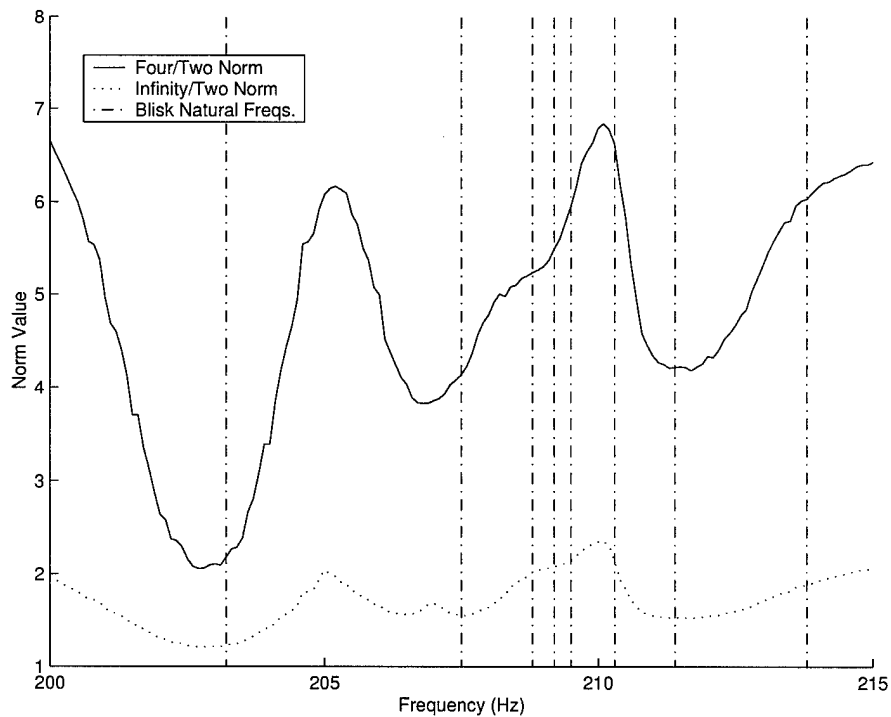


Figure B.6 Four/Two and Infinity/Two Norm Plot - Case I, E.O. 6, 1<sup>st</sup> Bending Mode

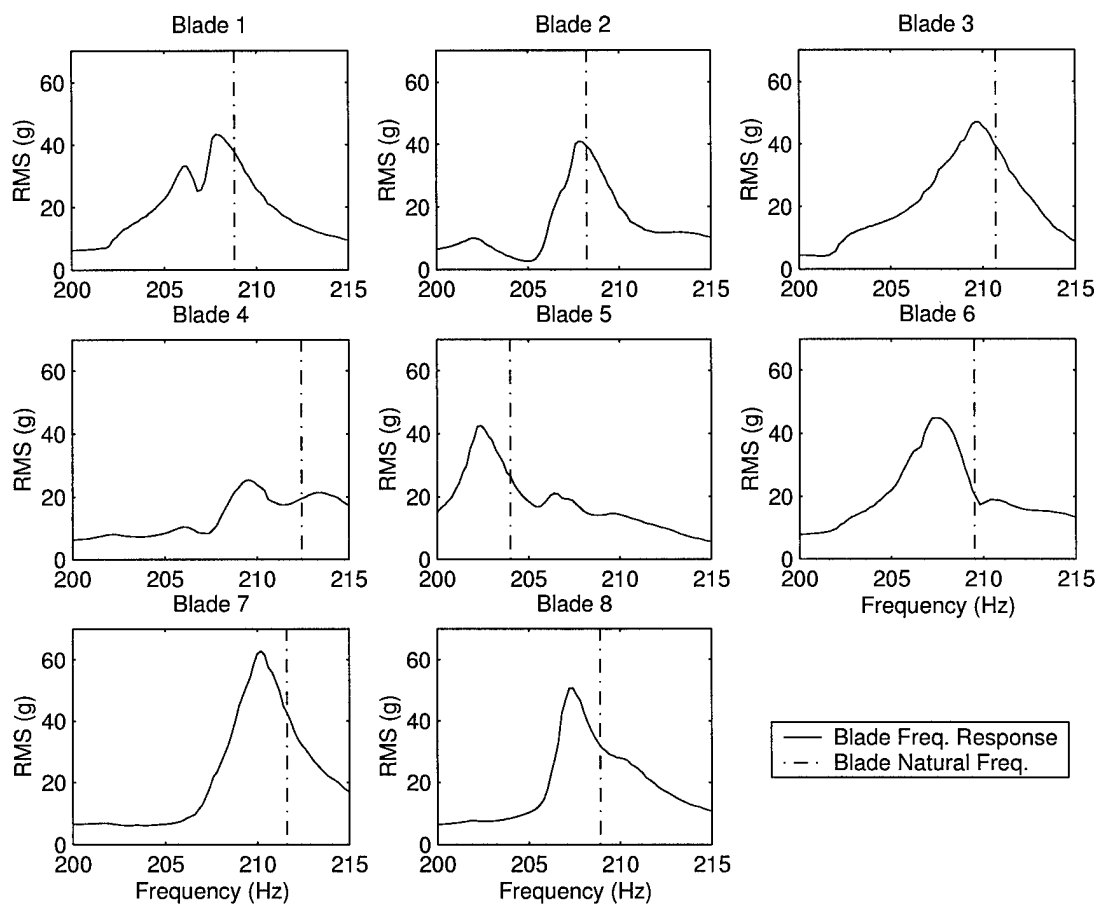


Figure B.7 Individual Blade Responses - Case I, E.O. 12, 1<sup>st</sup> Bending Mode

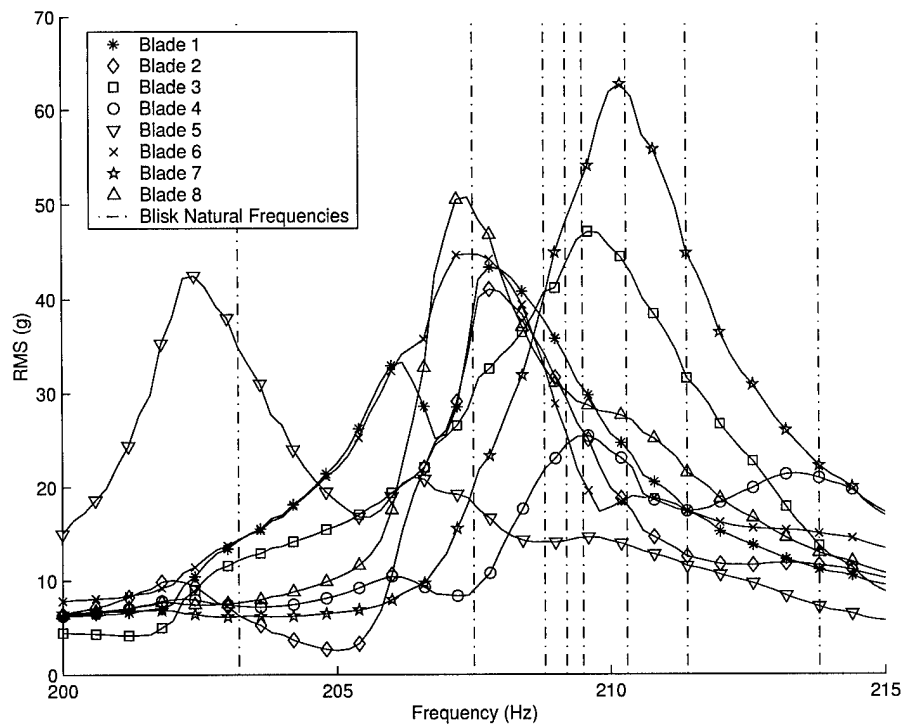


Figure B.8 Blade Responses - Case I, E.O. 12, 1<sup>st</sup> Bending Mode

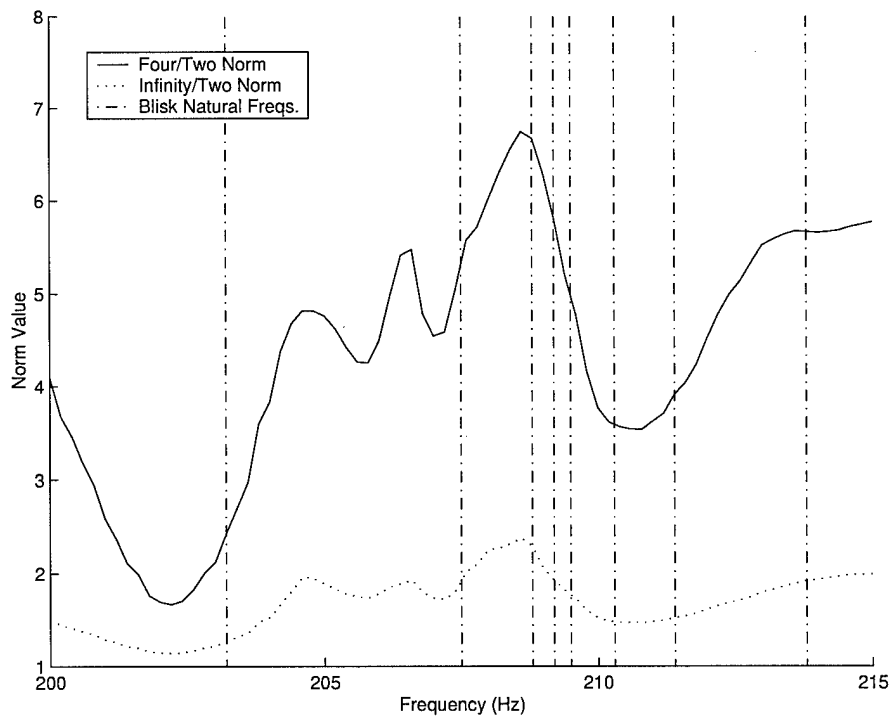


Figure B.9 Four/Two and Infinity/Two Norm Plot - Case I, E.O. 12, 1<sup>st</sup> Bending Mode

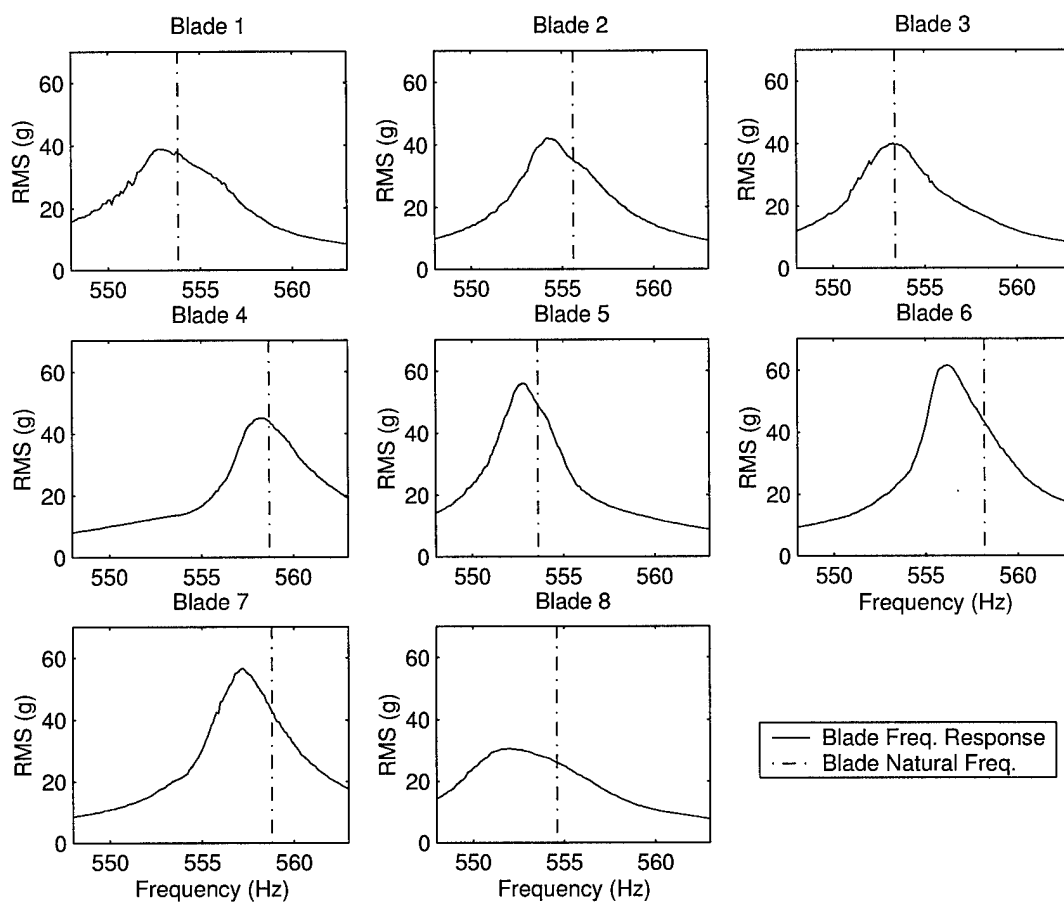


Figure B.10 Individual Blade Responses - Case I, E.O. 6, 1<sup>st</sup> Torsion Mode

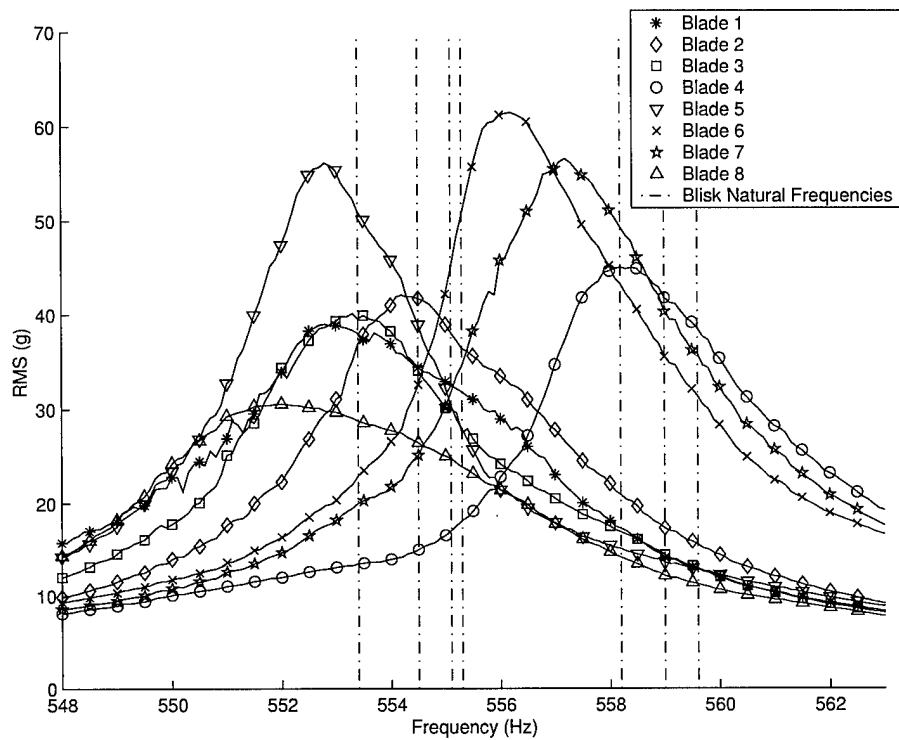


Figure B.11 Blade Responses - Case I, E.O. 6, 1<sup>st</sup> Torsion Mode

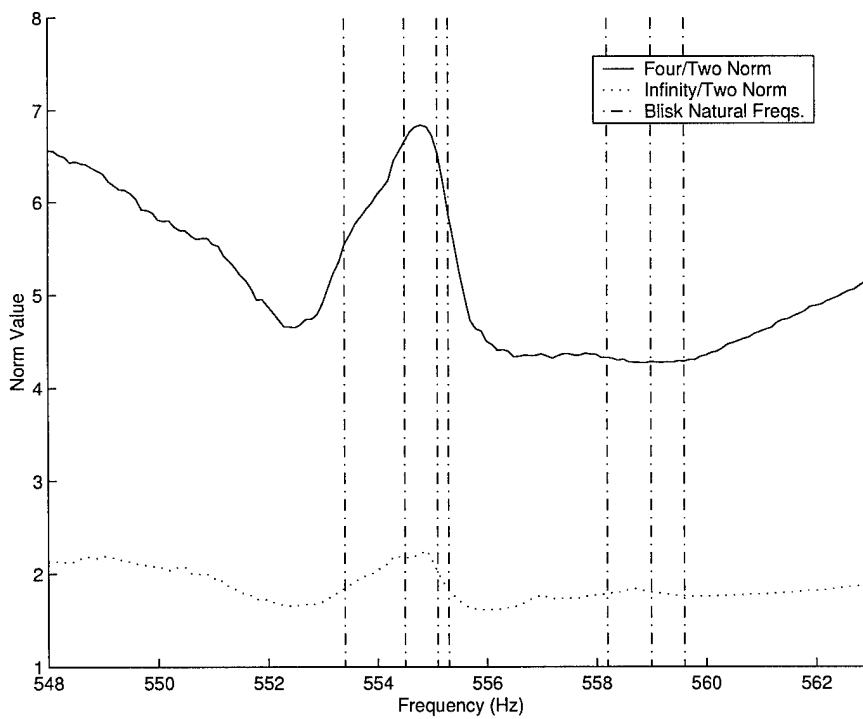


Figure B.12 Four/Two and Infinity/Two Norm Plot - Case I, E.O. 6, 1<sup>st</sup> Torsion Mode

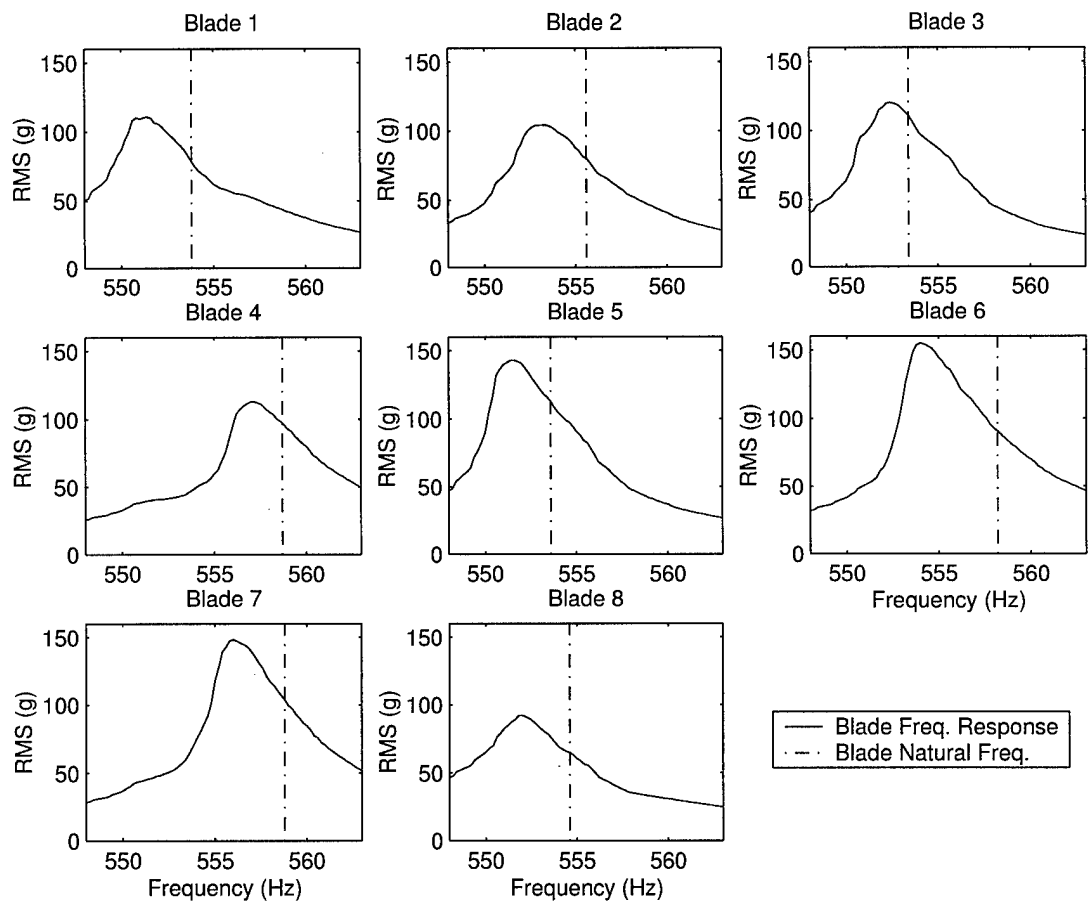


Figure B.13 Individual Blade Responses - Case I, E.O. 12, 1<sup>st</sup> Torsion Mode

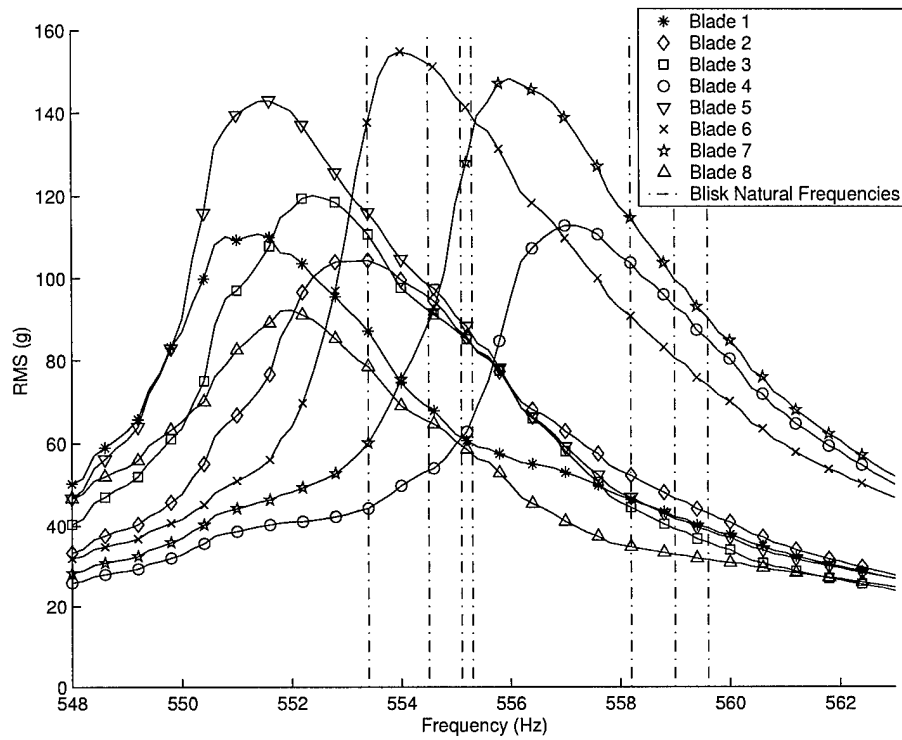


Figure B.14 Blade Responses - Case I, E.O. 12, 1<sup>st</sup> Torsion Mode

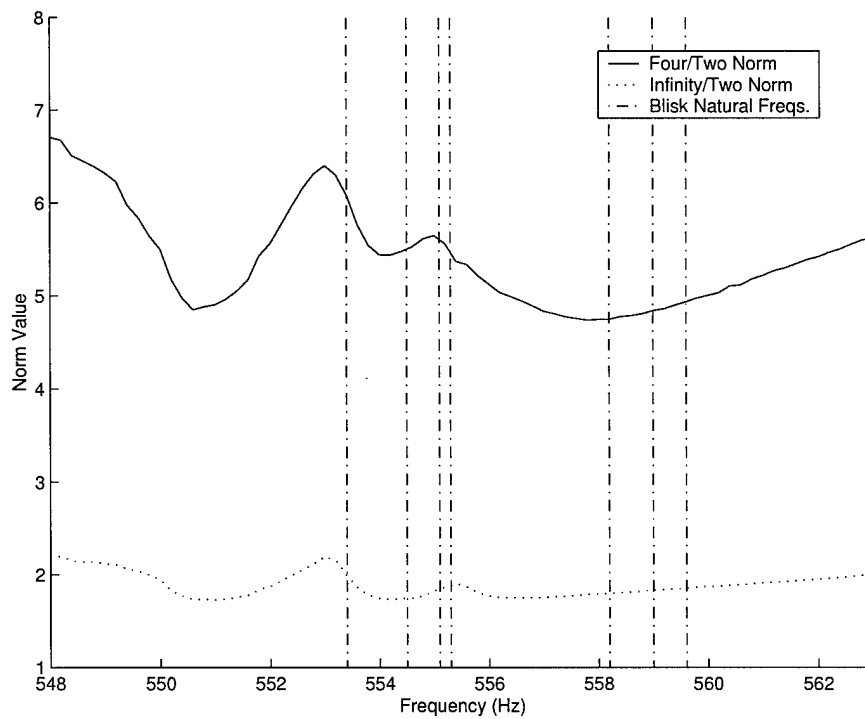


Figure B.15 Four/Two and Infinity/Two Norm Plot - Case I, E.O. 12, 1<sup>st</sup> Torsion Mode

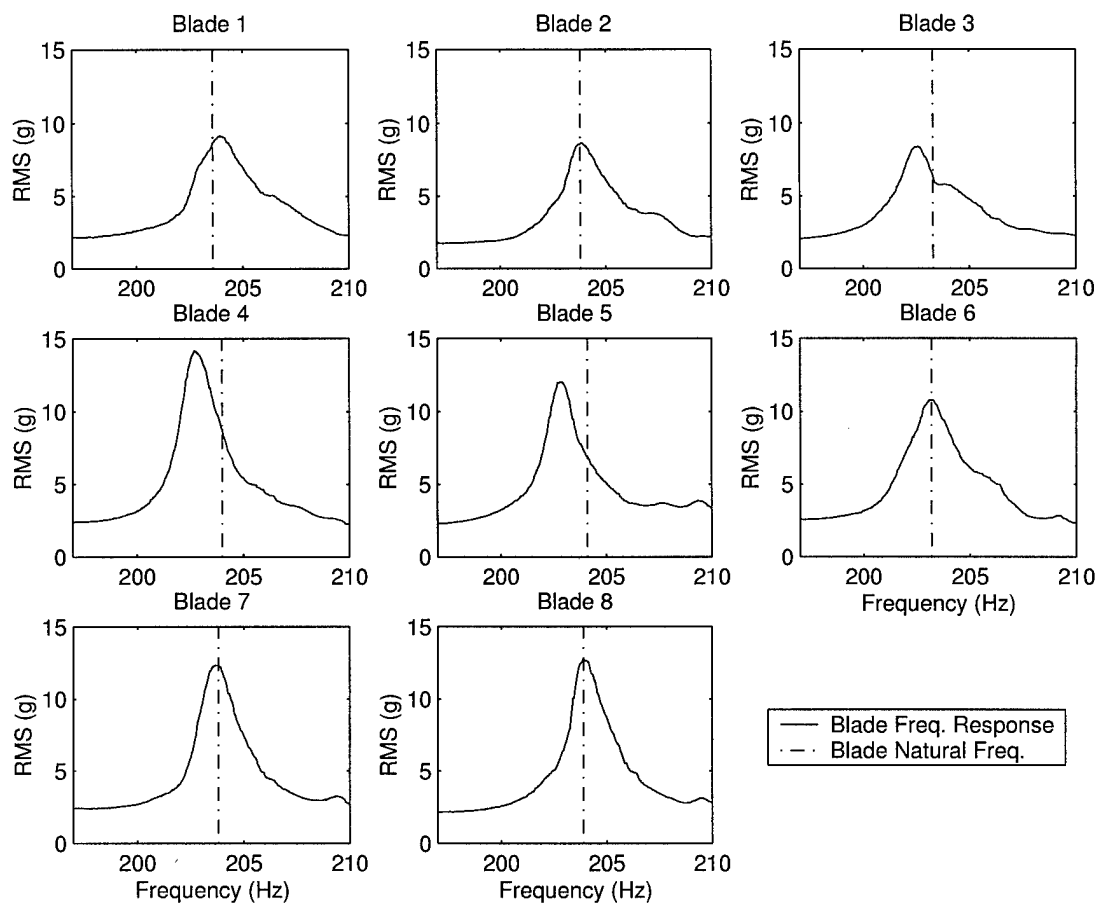


Figure B.16 Individual Blade Responses - Case II, E.O. 3, 1<sup>st</sup> Bending Mode

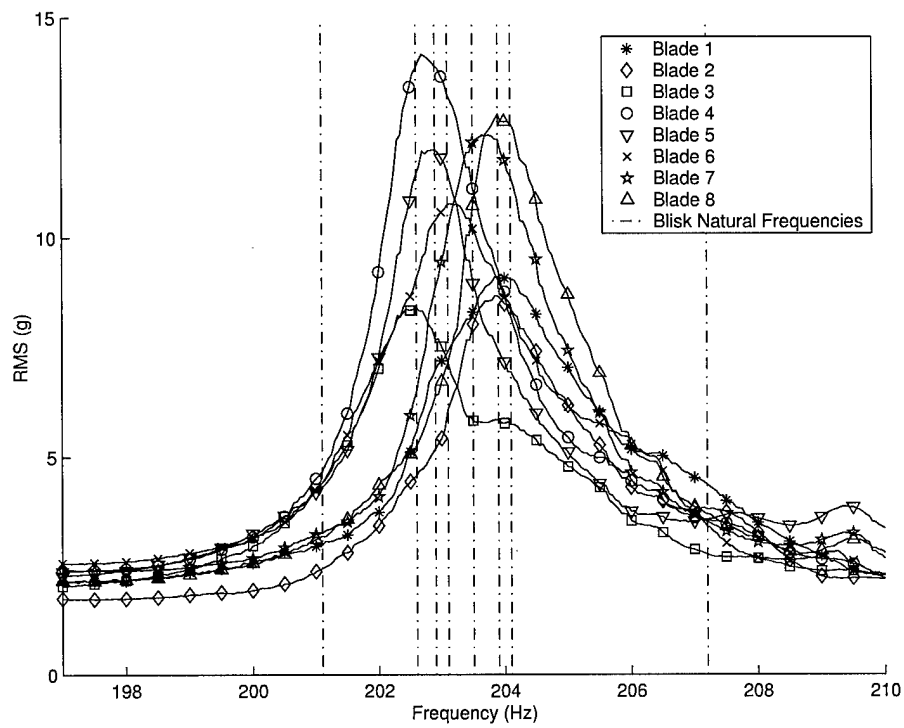


Figure B.17 Blade Responses - Case II, E.O. 3, 1<sup>st</sup> Bending Mode

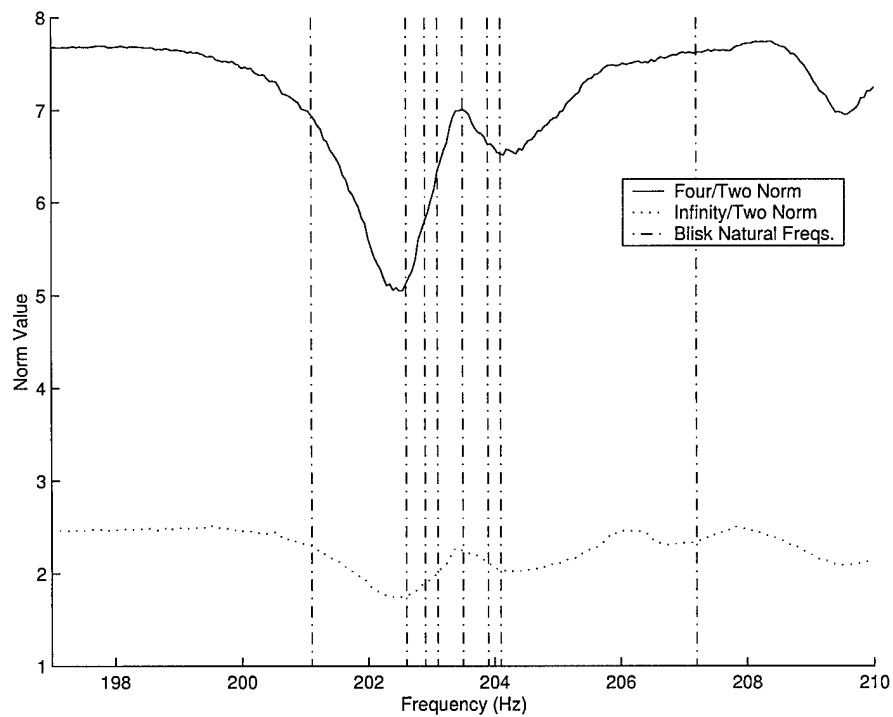


Figure B.18 Four/Two and Infinity/Two Norm Plot - Case II, E.O. 3, 1<sup>st</sup> Bending Mode

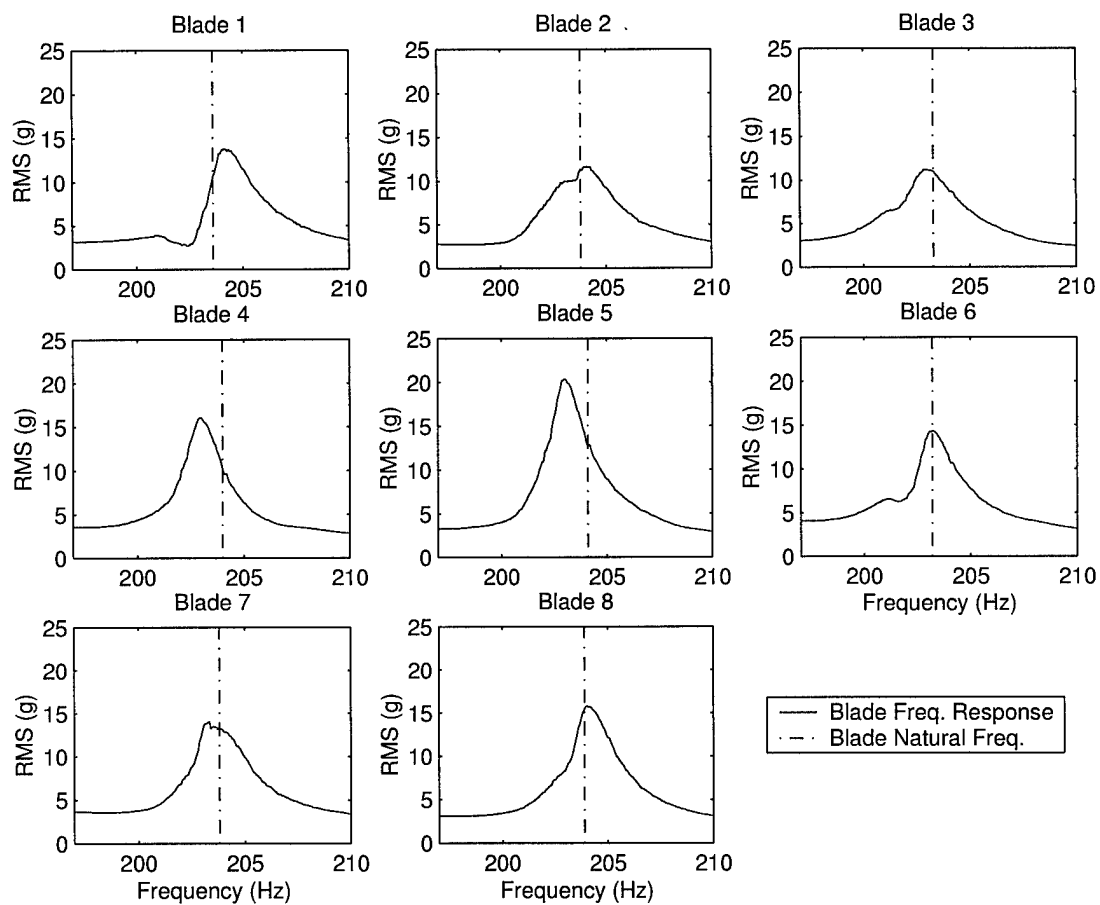


Figure B.19 Individual Blade Responses - Case II, E.O. 4, 1<sup>st</sup> Bending Mode

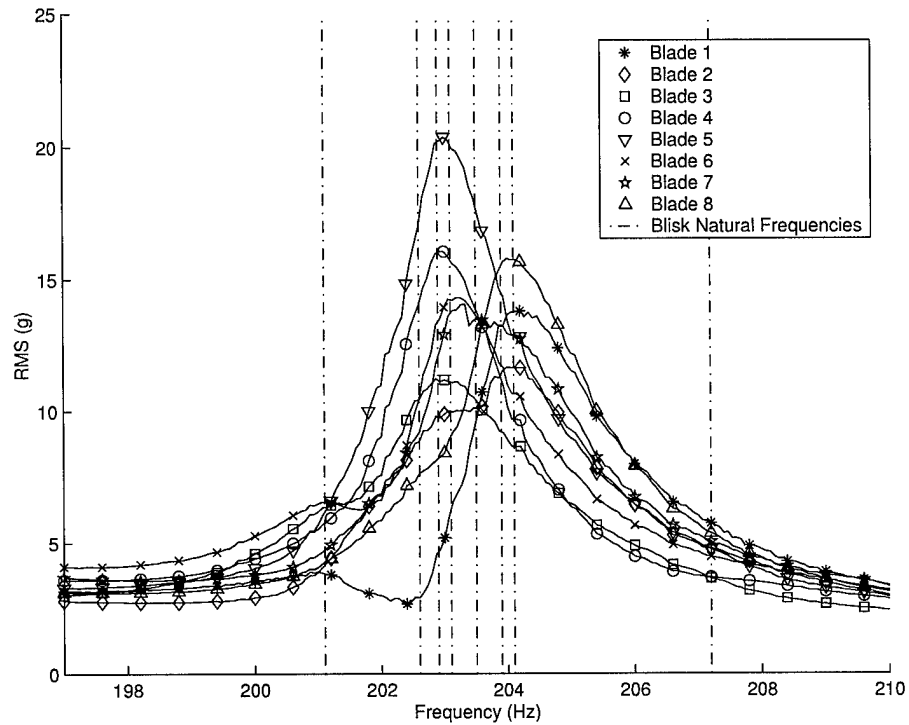


Figure B.20 Blade Responses - Case II, E.O. 4, 1<sup>st</sup> Bending Mode

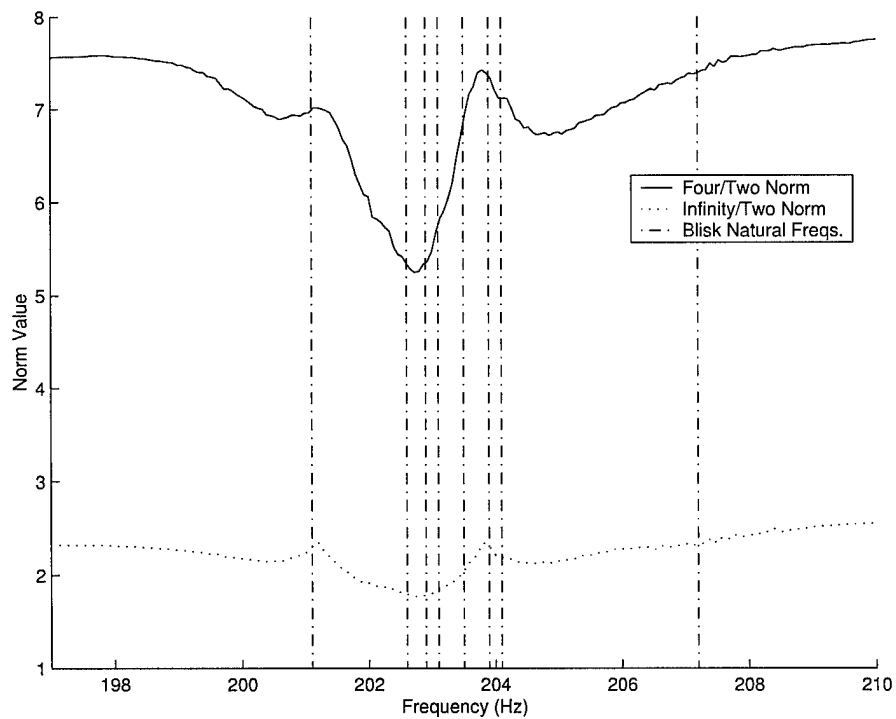


Figure B.21 Four/Two and Infinity/Two Norm Plot - Case II, E.O. 4, 1<sup>st</sup> Bending Mode

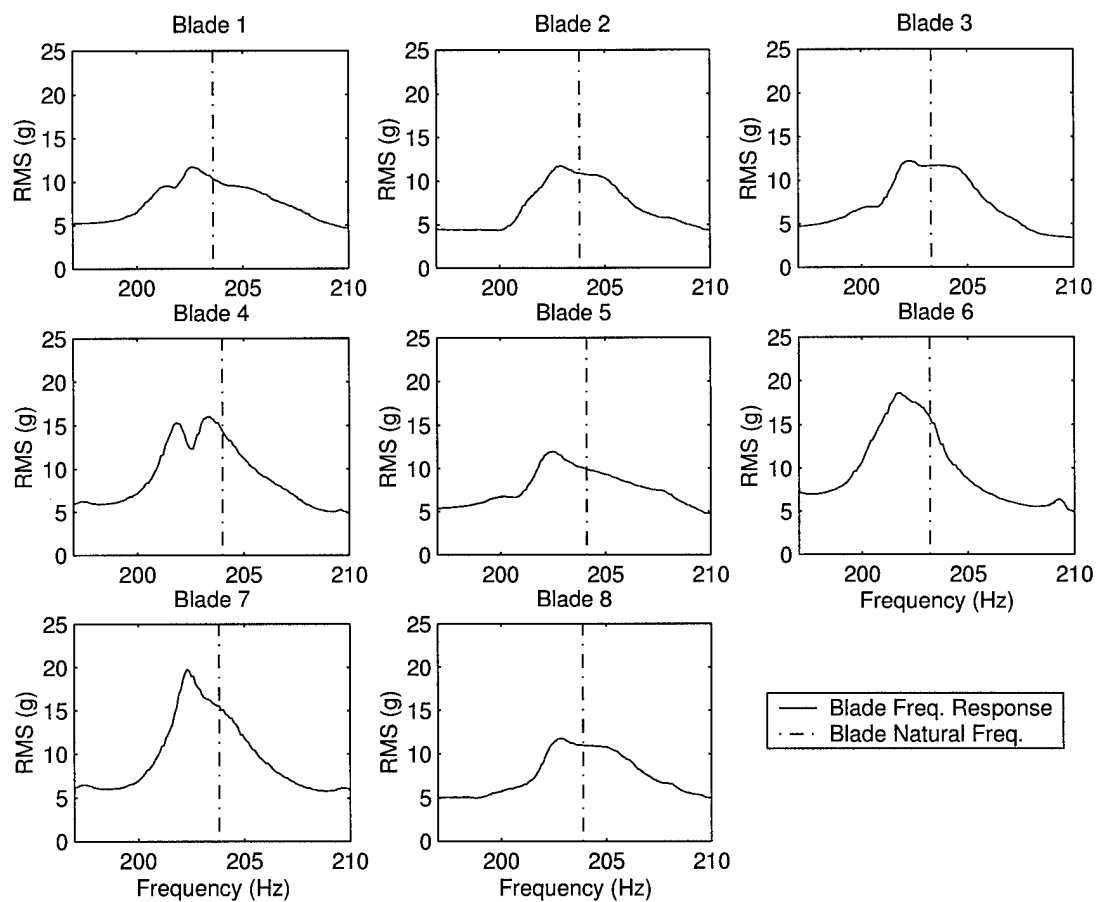


Figure B.22 Individual Blade Responses - Case II, E.O. 6, 1<sup>st</sup> Bending Mode

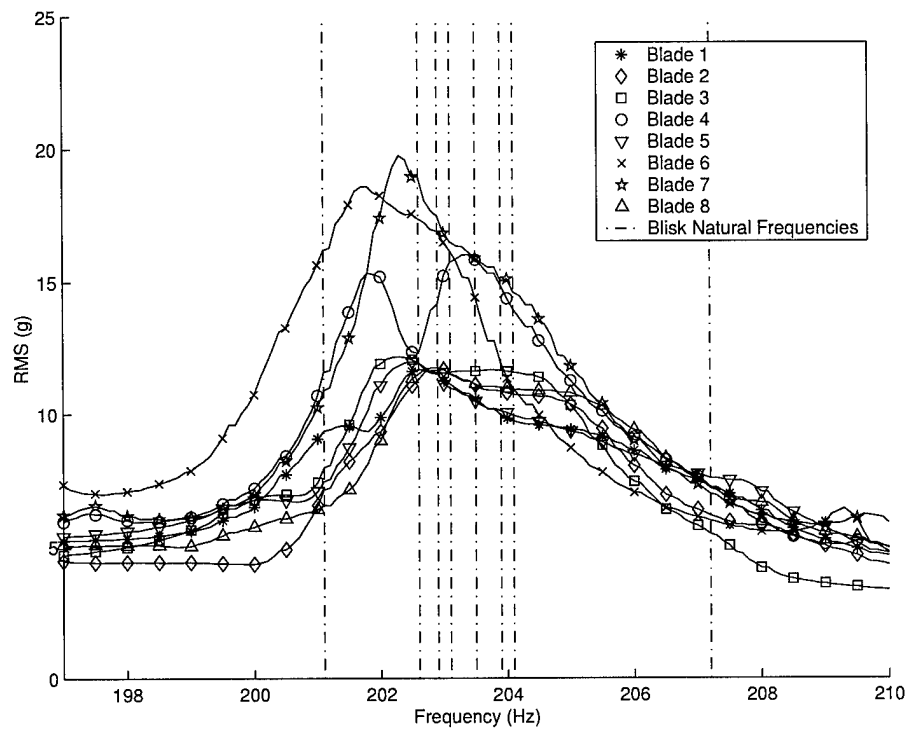


Figure B.23 Blade Responses - Case II, E.O. 6, 1<sup>st</sup> Bending Mode

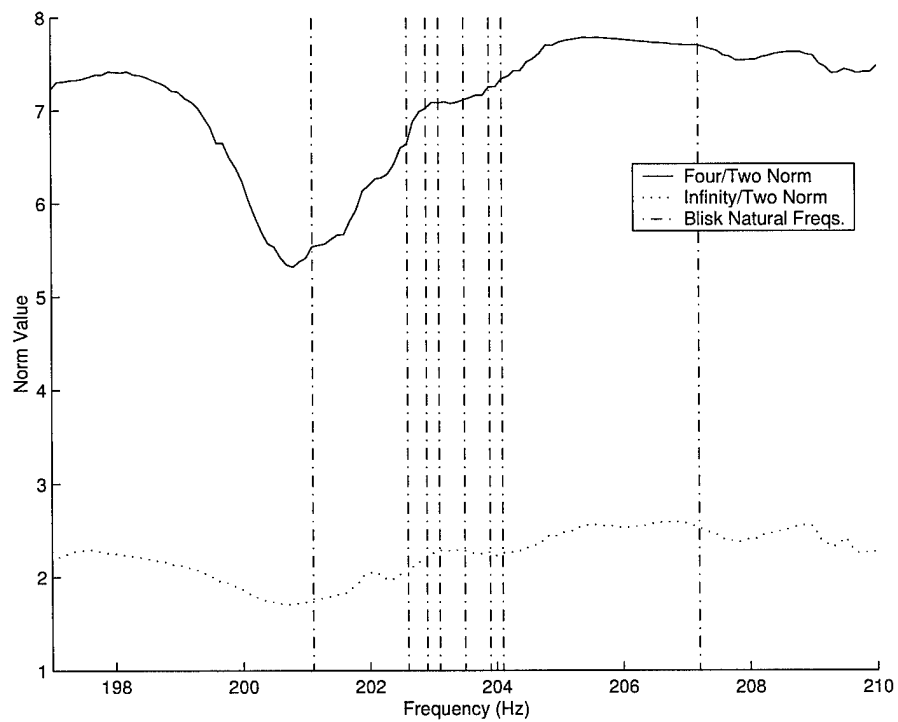


Figure B.24 Four/Two and Infinity/Two Norm Plot - Case II, E.O. 6, 1<sup>st</sup> Bending Mode

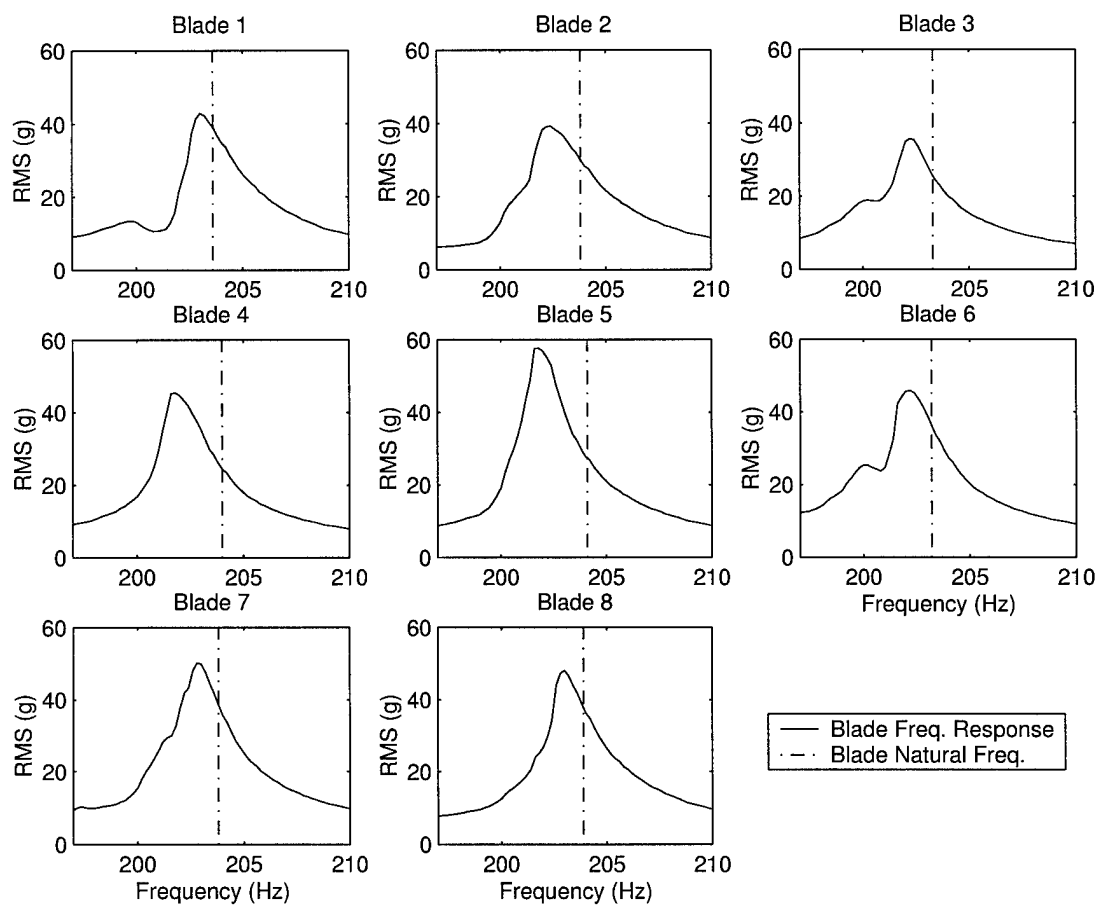


Figure B.25 Individual Blade Responses - Case II, E.O. 12, 1<sup>st</sup> Bending Mode

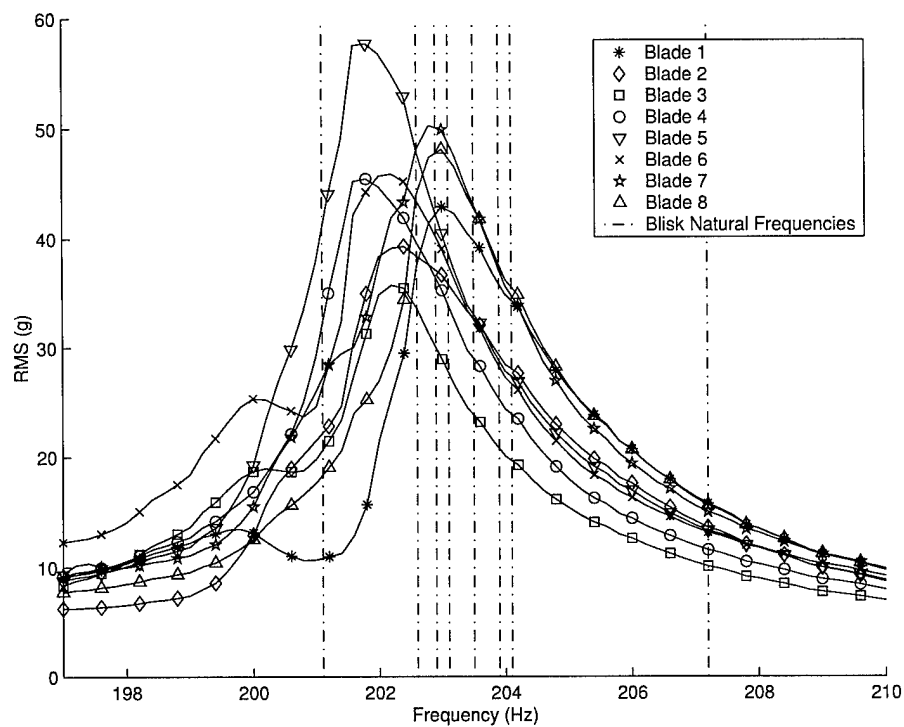


Figure B.26 Blade Responses - Case II, E.O. 12, 1<sup>st</sup> Bending Mode

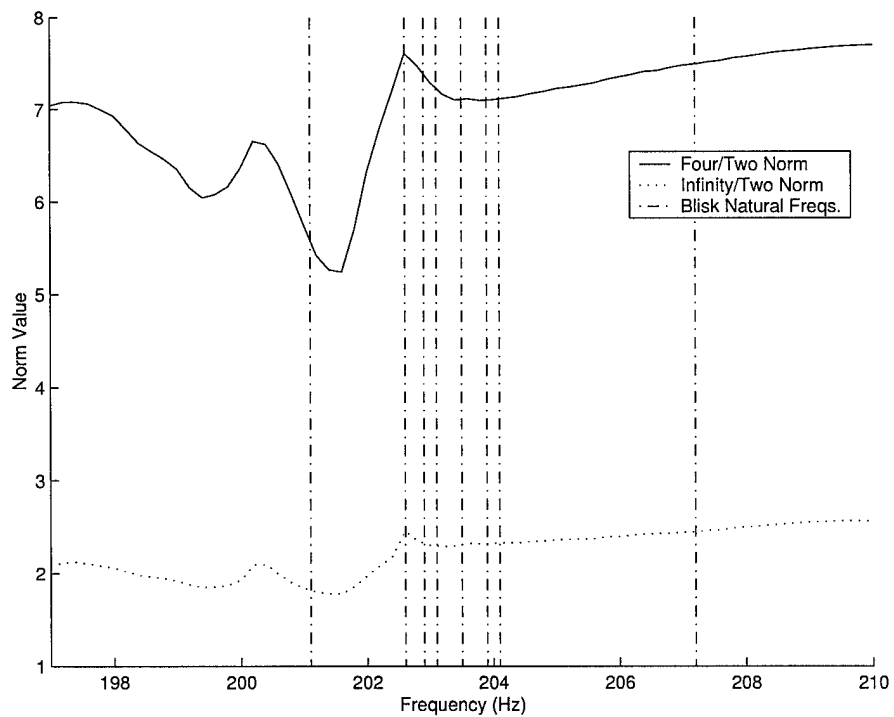


Figure B.27 Four/Two and Infinity/Two Norm Plot - Case II, E.O. 12, 1<sup>st</sup> Bending Mode

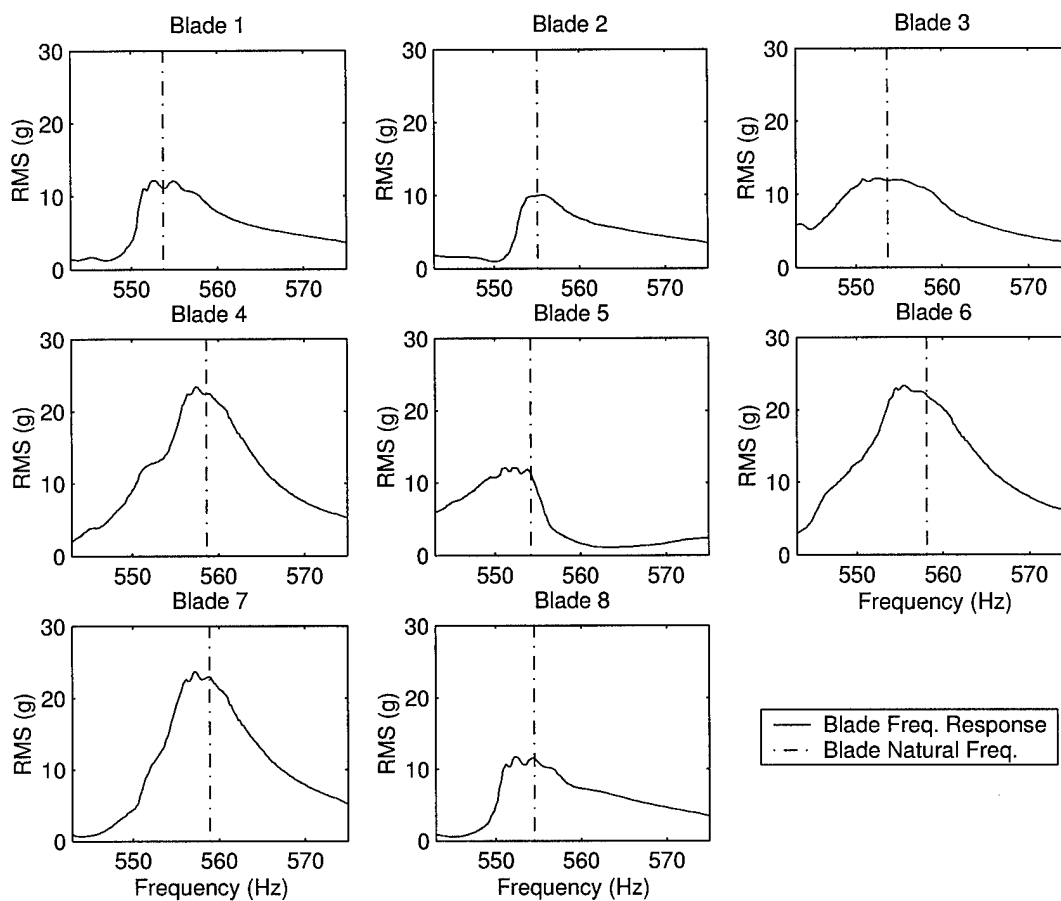


Figure B.28 Individual Blade Responses - Case II, E.O. 6, 1<sup>st</sup> Torsion Mode

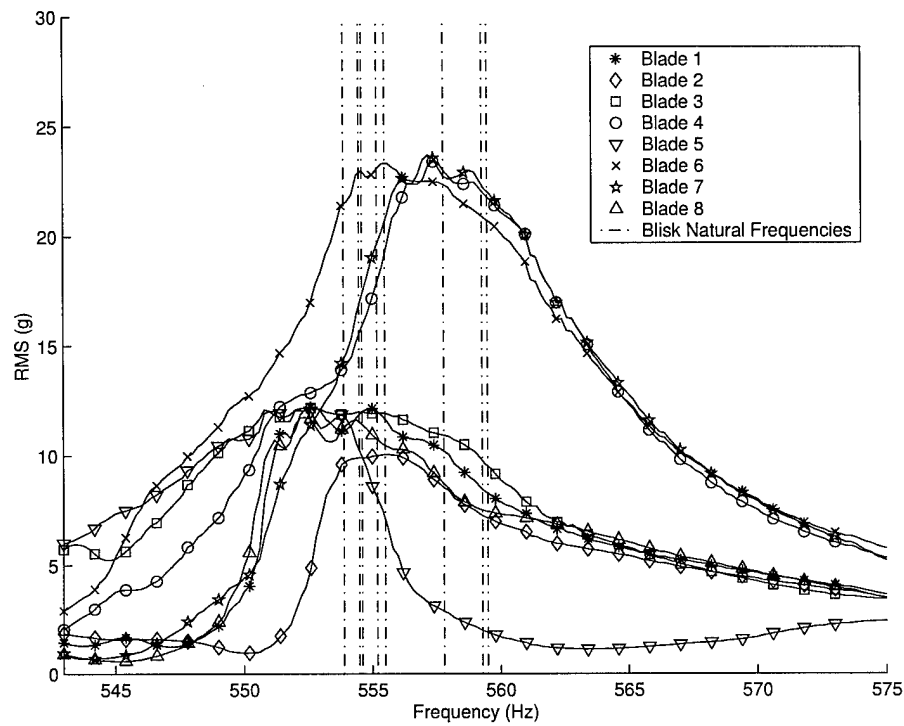


Figure B.29 Blade Responses - Case II, E.O. 6, 1<sup>st</sup> Torsion Mode

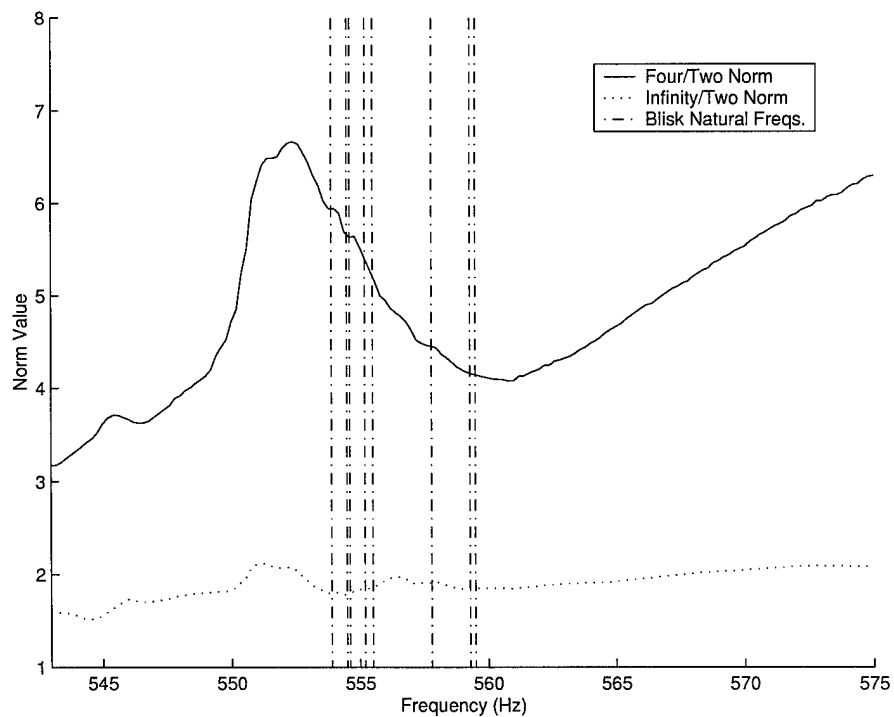


Figure B.30 Four/Two and Infinity/Two Norm Plot - Case II, E.O. 6, 1<sup>st</sup> Torsion Mode

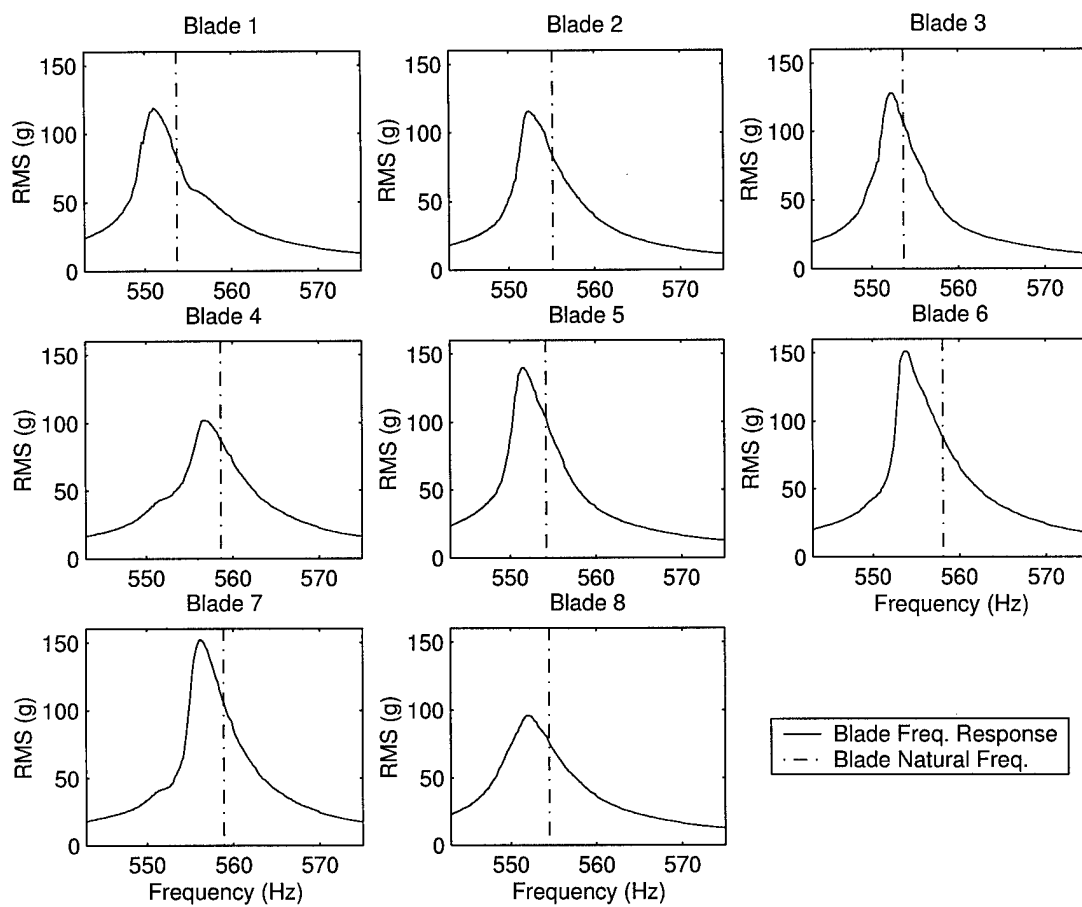


Figure B.31 Individual Blade Responses - Case II, E.O. 12, 1<sup>st</sup> Torsion Mode

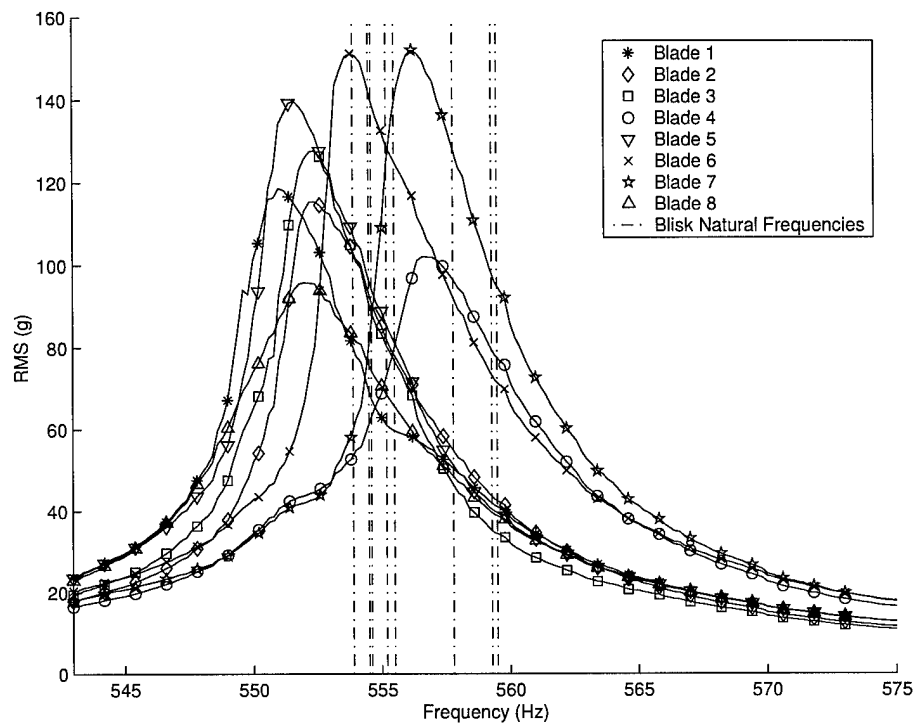


Figure B.32 Blade Responses - Case II, E.O. 12, 1<sup>st</sup> Torsion Mode

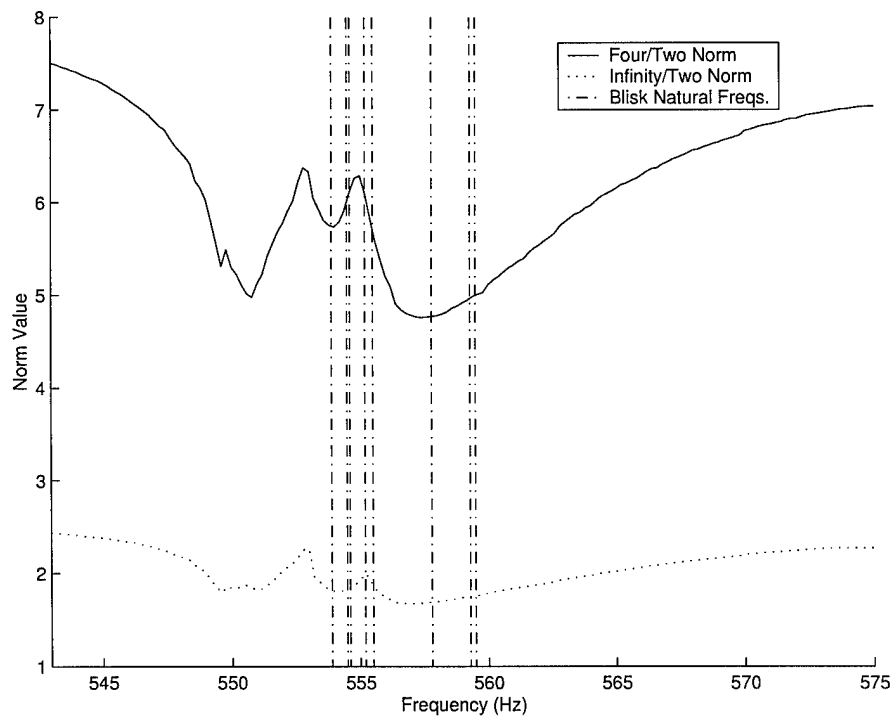


Figure B.33 Four/Two and Infinity/Two Norm Plot - Case II, E.O. 12, 1<sup>st</sup> Torsion Mode

## *Bibliography*

1. ACX, "ACX 1224/5 Quickpack Power Amplifier Operating Manual," 1994.
2. ACX, "ACX QP10Ni Operating Manual," 1999.
3. Agnes, Gregory, "Informal correspondence between G. Agnes and C. Duffield."
4. Agnes, Gregory, "MECH 719 Class Notes - Time Domain Identification Techniques."
5. Castanier, M. and others. "A Reduced Order Modeling Technique for Mistuned Bladed Disks," *Journal of Vibrations and Acoustics*, 119(7):439-447 (July 1997).
6. Castanier, M. and C. Pierre. "Investigation of the Combined Effects of Intentional and Random Mistuning on the Forced Response of Bladed Disk." *34th AIAA/ASME/SAE/ASEE Joint Propulsion Conference and Exhibit*. Washington D.C.: AIAA, July 1998.
7. Cornwell, Phillip J. and Oddvar O. Bendiksen. "A Numerical Study of Vibration Localization in Disordered Cyclic Structures." *Proceedings of the AIAA/ASME/ASCE/AHS/ASC 30th Structures, Structural Dynamics and Materials Conference*. 199-208. Washington D.C.: AIAA, April 1989.
8. Cox, Second Lieutenant Amy M. *A Statistical Analysis of Space Structure Mode Localization*. MS thesis, AFIT/GSO/ENY/99M-001, ENY, WPAFB, March 1999 (AFSOR-PO-A990011).
9. Endevco, "Endevco General Catalog," 1989. Page 1.14, Technical information for Models 2250a-10/2250AM1-10 Micro Minature Isotron<sup>TM</sup> Shear Accelerometers.
10. Ewins, D. J. "Effects of Detuning Upon the Forced Vibrations of Bladed Disks," *Journal of Sound and Vibration*, 9(1):65-79 (January 1969).
11. Ewins, D. J. "Vibration Characteristics of Bladed Disc Assemblies," *Journal of Mechanical Engineering Science*, 15(3):165-186 (March 1973).
12. Ewins, D. J. *Modal Testing: Theory and Practice*, 1. 1. New York, NY 10158: John Wiley and Sons Inc., 1984.
13. Ewins, D. J. and Z. S. Han. "Resonant Vibration Levels of a Mistuned Bladed Disk," *Journal of Vibration, Acoustics, Stress and Reliability in Design*, 106(4):211-217 (April 1984).
14. Hodges, C. H. "Confinement of Vibration by Structural Irregularity," *Journal of Sound and Vibration*, 82(3):441-424 (March 1982).
15. Hollkamp, J. and R. Gordon. "An Experimental Investigation of Non-Uniform Damping in Bladed Disk Assemblies." *34th AIAA/ASME/SAE/ASEE Joint Propulsion Conference and Exhibit*. Number AIAA Paper 98-3747. Washington D.C.: AIAA, July 1998.
16. Hollkamp, Joseph J., "Informal correspondence between J. Hollkamp and C. Duffield."

17. Hollkamp, Joseph J., "ERA.m," 1991. MATLAB® based Eigenstructure Realization Algorithm (ERA) routine.
18. Hollkamp, Joseph J., "weave.m," 1991. MATLAB® based ERA multi-SIMO to MIMO Conversion routine.
19. Hollkamp, Joseph J. and Robert W. Gordon. "Modal Testing of a Bladed Disk." *Proceedings of the 17th International Modal Analysis Conference*. February 1999.
20. Hollkamp, Joseph J., "irf.m," 1991. MATLAB® based Impulse Response Function routine.
21. Juang, Jer-Nan and Richard S. Pappa. "An Eigensystem Realization Algorithm for Modal Parameter Identification and Modal Reduction," *AIAA Journal of Guidance, Control and Dynamics*, 8(5):620-627 (September 1985).
22. Kim, Youdan, "Eign.m," 1991. Matlab based Eigenvalue/Eigenvector routine.
23. Kramer, Stuart C. *Vector Dynamics*. Dayton, OH: Private Printing, 1998.
24. Kruse, Marlin and C. Pierre. "Dynamic Reponse of an Industrial Turbomachinery Rotor." *32th AIAA/ASME/SAE/ASEE Joint Propulsion Conference and Exhibit*. Washington D.C.: AIAA, July 1996.
25. Kruse, Marlin and C. Pierre. "Forced Reponse of Mistuned Bladed Disks Using Reduced-Order Modeling." *37th AIAA/ASME/SAE/ASEE Joint Propulsion Conference and Exhibit*. Washington D.C.: AIAA, July 1996.
26. National Aeronautics and Space Administration, Scientific and Technical Information Division (Leissa Report). *Vibration of Plates*. Scientific Publication 160. Washington D.C.: U.S. Government Printing Office, 1969.
27. Lin, C.-C. and M. P. Mignolet. "Effects on Damping and Damping Mistuning on the Forced Vibration Reponse of Bladed Disks," *Journal of Sound and Vibration*, 193(2):525-540 (1996).
28. Ometron, "VH300 Laser Vibrometer Operator's Manual," 1997.
29. Ottarsson, Gisli and C. Pierre. "On the Effects of Interblade Coupling on the Statistics of Maximum Forced Response Amplitudes in Mistuned Bladed Disks." *Proceedings of the AIAA/ASME/ASCE/AHS 36th Structural Dynamics and Materials Conference*. 3070-3078. Washington D.C.: AIAA, April 1995.
30. Pierre, C. "Weak and Strong Vibration Localization in Disordered Structures: A Statistical Investigation." *Proceedings of the AIAA/ASME/ASCE/AHS 29th Structural Dynamics and Materials Conference*. 1511-1521. Washington D.C.: AIAA, April 1988.
31. Pierre, C. and D. V. Murthy. "Aeroelastic Modal Characteristics of Mistuned Blade Assemblies: Mode Localization and Loss of Eigenstructure," *AIAA Journal*, 30(10):2483-2496 (October 1992).
32. Pierre, Christophe. "Localized Free and Forced Vibrations of Nearly Periodic Structures." *Proceedings of the AIAA/ASME/ASCE/AHS 28th Structural Dynamics and Materials Conference*. 186-197. Washington D.C.: AIAA, April 1987.

33. Rao, J. S. *Turbomachine Blade Vibration*, 1. 1. New York, NY 10158: John Wiley and Sons Inc., 1991.
34. Sinha, Alok. "Calculating the Statistics of Forced Response of a Mistuned Bladed Disk Assembly," *AIAA Journal*, 24(11):1797-1801 (November 1986).
35. Slater, Joseph C. and Andrew J. Blair. *A Design Strategy for Preventing High Cycle Fatigue by Minimizing Sensitivity of Bladed Disks to Mistuning*. Technical Report, Bolling AFB, Washington D.C.: Air Force Office of Scientific Research, 1996.
36. Srinivasan, A. V. "Vibrations of Bladed-Disk Assemblies - A Selected Survey," *Journal of Vibration, Acoustics, Stress and Reliability in Design*, 106(4):1797-1801 (April 1984).
37. T., Wei. S. and C. Pierre. "Statistical Analysis of the Forced Response of Mistuned Cyclic Assemblies," *AIAA Journal*, 28(5):861-868 (May 1990).
38. Tang, J. and K. W. Wang. "Vibration Control of Rotationally Periodic Structures Using Passive Piezoelectric Shunt Networks and Active Compensation," *Journal of Vibration and Acoustics*, 121(7):379-390 (July 1999).
39. U.S. Air Force Scientific Advisory Board. *Structural Failure Modes of Titanium Components in Fans and Compressors of Air Force Gas Turbine Engines*. Technical Report P25; No. 108. Washington: Government Printing Office, 1994.
40. Wei, S. T. and C. Pierre. "Localization Phenomena in Mistuned Assemblies with Cyclic Symmetry Part II: Forced Vibrations," *Journal of Vibration, Acoustics, Stress, and Reliability in Design*, 110(10):439-449 (October 1988).
41. Wie, S.T. and C. Pierre. "Localization Phenomena in Mistuned Assemblies with Cyclic Symmetry Part I: Free Vibrations," *Journal of Vibration, Acoustics, Stress and Reliability in Design*, 110(4):429-438 (April 1988).

REPORT DOCUMENTATION PAGE			Form Approved OMB No. 0704-0188	
Public reporting burden for this collection of information is estimated to average 1 hour per response, including the time for reviewing instructions, searching existing data sources, gathering and maintaining the data needed, and completing and reviewing the collection of information. Send comments regarding this burden estimate or any other aspect of this collection of information, including suggestions for reducing this burden, to Washington Headquarters Services, Directorate for Information Operations and Reports, 1215 Jefferson Davis Highway, Suite 1204, Arlington, VA 22202-4302, and to the Office of Management and Budget, Paperwork Reduction Project (0704-0188), Washington, DC 20503.				
1. AGENCY USE ONLY (Leave blank)		2. REPORT DATE March 2000		3. REPORT TYPE AND DATES COVERED Master's Thesis
4. TITLE AND SUBTITLE AN EXPERIMENTAL INVESTIGATION ON PERIODIC FORCED VIBRATIONS OF A BLADED DISK				5. FUNDING NUMBERS
6. AUTHOR(S)  Colin J. Duffield, Captain, USAF				
7. PERFORMING ORGANIZATION NAME(S) AND ADDRESS(ES) Air Force Institute of Technology 2950 P Street, Bldg 640 WPAFB, OH 45433-7765				8. PERFORMING ORGANIZATION REPORT NUMBER  AFIT/GAE/ENY/00M-05
9. SPONSORING/MONITORING AGENCY NAME(S) AND ADDRESS(ES) AFIT/ENY 2950 P Street, Bldg 640 WPAFB, OH 45433-7765				10. SPONSORING/MONITORING AGENCY REPORT NUMBER
11. SUPPLEMENTARY NOTES Advisor - Captain Gregory Agnes, ENY Gregory.Agnes@afit.af.mil (937) 255-6565 ext. 4317, DSN 785				
12a. DISTRIBUTION AVAILABILITY STATEMENT  Approved for public release; distribution unlimited				12b. DISTRIBUTION CODE
13. ABSTRACT (Maximum 200 words) Aircraft engine blades are subject to harmonic forcing produced from periodic wakes created by fixed stators. Prolong or repeated exposure at blade resonant frequencies can cause vibration-induced fatigue, otherwise known as High Cycle Fatigue (HCF). Structural mistuning coupled with HCF causes premature blade failures, excessive operational costs and increased engine servicing. This study offered a novel approach to characterize mistuning effects on bladed disk forced vibration behavior. A model fan reduced in dynamic scale from an operational jet engine fan and with weak inter-blade coupling was fabricated. Aerodynamic disturbances produced by the stators were replicated by magnets attached to a rotating flywheel interacting with similar magnets epoxied to the model fan blades. Magnet configurations mimicked engine order. Accelerometers transducers at blade tips measured forced vibration loads. Transducer response signals were analyzed by a data acquisition system. The flywheel excitation system performed very well in its ability to impart periodic forcing onto the bladed disk. The harmonic forcing input was characterized and capable of producing a wide assortment of forced vibration results. Mistuning and engine order primarily effected system response, specifically in the areas of localization levels, individual blade response profiles, number of maximum blade amplitude peaks and localization frequency range.				
14. SUBJECT TERMS Bladed Disk, Cyclic Structures, Rotationally Periodic Structures, Forced Response, Mode Localization, Mistuning, Turbine Blades, Compressor Blades, Vibrations, High Cycle Fatigue				15. NUMBER OF PAGES 152
				16. PRICE CODE
17. SECURITY CLASSIFICATION OF REPORT  UNCLASSIFIED		18. SECURITY CLASSIFICATION OF THIS PAGE  UNCLASSIFIED		19. SECURITY CLASSIFICATION OF ABSTRACT  UNCLASSIFIED
				20. LIMITATION OF ABSTRACT  UL